People’s Democratic Republic of Algeria
Ministry of Higher Education and Scientific Research
Kasdi Merbah University Ouargla
College of Mathematics and Matter Sciences
Department of Chemistry

Thesis

Presented with a view to obtaining the Diploma of Doctorate in LMD

Speciality: Materials Chemistry

Theme:

Synthesis of manganese and nickel oxide nanoparticles from sunflower husks and studying their effectivenss in removing heavy metals from aqueous solutions

Presented by: ***Aouadj Ikram***

Publicly supported on: 22/10/2025

Before the Jury composed of:

Nedjimi Mohammed Said	Professor	University of Ouargla	President
Zerrouki Hayat	MCA	University of Ouargla	Supervisor
Zenkhri Louiza	Professor	University of Ouargla	Co-Supervisor
Neghmouche Nacer Salah	MCA	University of El-Oued	Examiner
Souyei Belgacem	MCA	University of El-Oued	Examiner
Belfar Mohamed El Akhdar	Professor	University of Ouargla	Examiner
Doureid Mohamed El Habib	MCA	University of Ouargla	Examiner

Academic Year: 20252026

Abstract

The green synthesis of metal oxide nanoparticles using plant-based extracts offers a sustainable, efficient, and eco-friendly alternative to conventional chemical routes. In this study, nickel oxide (NiO), mixed manganese oxides (MnO_2/Mn_2O_3), and hausmannite (Mn_3O_4) nanoparticles were synthesized employing sunflower seed husk extract as a natural reducing and stabilizing agent through a simple, rapid, and cost-effective method.

The obtained nanoparticles were characterized by UVVis, FTIR, XRD, SEM, EDX, and BET analyses, revealing stable nanostructures with average crystallite sizes of 14.11, 29.93, and 20.30 nm, respectively. Their adsorption performance toward Pb^{2+}, Cd^{2+}, and Cu^{2+} ions from aqueous media was systematically evaluated under varying pH, contact time, initial concentration, temperature, and adsorbent dosage conditions. The adsorption equilibrium and kinetics were best described by the Langmuir and Freundlich isotherm models and the pseudo-first- and pseudo-second-order kinetic models, respectively, while thermodynamic parameters confirmed the spontaneous nature of adsorption.

The nanoparticles demonstrated exceptionally high removal efficiencies (up to 99.7%), underscoring their promising potential as sustainable nanoadsorbents for heavy metal remediation and environmentally safe water purification applications.

Keywords: green synthesis; *Helianthus annuus* seed husks; nanoparticles (NiO, MnO_2/Mn_2O_3, Mn_3O_4); heavy metals; adsorption.

Résumé

La synthèse verte de nanoparticules doxydes métalliques à partir dextraits végétaux constitue une approche écologique, économique et durable en remplacement des méthodes chimiques classiques. Dans ce travail, des nanoparticules doxyde de nickel (NiO), doxydes mixtes de manganèse (MnO_2/Mn_2O_3) et dhausmannite (Mn_3O_4) ont été élaborées à laide de lextrait des coques de graines de tournesol comme agent réducteur et stabilisant naturel, selon une procédure simple, rapide et respectueuse de lenvironnement.

Les nanoparticules obtenues ont été caractérisées par UVVis, FTIR, XRD, SEM, EDX et BET, confirmant la formation de structures nanocristallines stables de tailles moyennes de 14,11 nm, 29,93 nm et 20,30 nm, respectivement. Leur performance dadsorption vis-à-vis des ions Pb^{2+}, Cd^{2+} et Cu^{2+} a été étudiée dans des conditions variées de pH, concentration initiale, temps de contact, température et masse dadsorbant.

Les isothermes de Langmuir et Freundlich ainsi que les modèles cinétiques de pseudo-premier et pseudo-deuxième ordre ont permis de décrire le mécanisme dadsorption, tandis que les paramètres thermodynamiques ont mis en évidence un processus spontané et endothermique.

Les matériaux obtenus ont montré des efficacités délimination très élevées (jusquà 99,7%), confirmant leur grand potentiel comme adsorbants nanostructurés pour la dépollution des métaux lourds et leur pertinence dans le traitement durable des eaux contaminées.

Mots-clés : synthèse verte; enveloppes de graines d’*Helianthus annuus*; nanoparticules (NiO, MnO_2/Mn_2O_3, Mn_3O_4); métaux lourds; adsorption.

ملخص

يمثل التصنيع الأخضر للجسيمات النانوية المعدنية باستخدام المستخلصات النباتية نهجًا مستدامًا وفعالًا بديلًا للطرق الكيميائية التقليدية. في هذا العمل، تم تحضير جسيمات نانوية من NiO و MnO_2/Mn_2O_3 ، و Mn_3O_4 (هاوسمانايت) باستخدام مستخلص قشور بذور دوّار الشمس بطريقة سريعة، منخفضة التكلفة، وصديقة للبيئة.

تم توصيف المواد المحضَّرة باستخدام UV–Vis، FTIR، XRD، SEM، EDX، وBET، وأظهرت النتائج تشكّل جسيمات نانوية مستقرة بأحجام 14.11، 29.93، و20.30 نانومتر على التوالي. تم تقييم أدائها في إزالة أيونات Pb^{2+} و Cd^{2+} ، و Cu^{2+} من المحاليل المائية عبر تجارب الامتزاز الدفعي، حيث تمت دراسة تأثير درجة الحموضة، تركيز الأيون، ووقت التلامس. حللت البيانات بنماذج Langmuir و Freundlich وحركيات شبه الدرجة الأولى والثانية، مع تقدير المعلمات الديناميكية الحرارية.

أظهرت الجسيمات النانوية كفاءة إزالة عالية بلغت حتى 99.7%، مما يؤكد فعاليتها الكبيرة في إزالة الملوثات المعدنية ويبرز إمكاناتها الواعدة في تطبيقات المعالجة البيئية المستدامة.

الكلمات المفتاحية: التصنيع الأخضر، قشور بذور دوار الشمس ،جسيمات النانوية(NiO, MnO_2/Mn_2O_3, Mn_3O_4) ، المعادن الثقيلة ، الامتزاز .

Acknowledgements

First and foremost, I express my gratitude to Almighty God for granting me the strength, patience, and perseverance to complete this work. Words cannot fully convey my deepest appreciation.

I extend my heartfelt thanks to my supervisor, Professor Hayat Zerrouki, for proposing this research topic, for her continuous support, valuable guidance, and patience throughout this journey.

My sincere thanks also go to my co-supervisor, Professor Louiza Zenkhri, for her encouragement and valuable advice.

I am deeply grateful to Professor Mohamed Lakhdar Belfar for his insightful discussions and guidance during this work.

I also wish to thank all members of the jury for accepting to evaluate this thesis.

Finally, I express my deepest gratitude to my family and all those who supported and encouraged me throughout this research.

Contents

List of Figures

List of Tables

List of Abbreviations

Abbreviation	**Meaning**
Pb	Lead
Cd	Cadmium
Cu	Copper
NPs	Nanoparticles
NiO	Nickel oxide
MnO_2	Manganese dioxide
Mn_2O_3	Manganese trioxide
Mn_3O_4	Trimanganese tetraoxide
SSHE	Sunflower seed husk extract
E_g	Band gap energy
JCPDS	Joint Committee on Powder Diffraction Standards
UVVis	Ultravioletvisible spectroscopy
XRD	X-ray diffraction
FTIR	Fourier Transform Infrared spectroscopy
SEM	Scanning Electron Microscopy
EDX	Energy Dispersive X-ray analysis
BET	BrunauerEmmettTeller method
C_0	Initial concentration
C_e	Equilibrium concentration
K_1	Pseudo first-order adsorption rate constant (min^{-1})
K_2	Pseudo second-order adsorption rate constant (gůmg^{-1}ůmin^{-1})
K_L	Langmuir constant (Lůmg^{-1})
K_F	Freundlich constant
ΔG°	Gibbs free energy
ΔH°	Enthalpy
ΔS°	Entropy
R^2	Coefficient of determination

General Introduction

General Introduction

Water contamination has become a critical global challenge due to the rapid advancement of industrialization, technology, and urban development [1]. Among various pollutants, heavy metals are of particular concern because they are toxic, non-biodegradable, and persistent in the environment. They originate from both anthropogenic and natural sources, including vehicle emissions, industrial discharge, and mining operations [2].

Lead (Pb), cadmium (Cd), and copper (Cu) are among the most frequently encountered toxic metals in industrial wastewater. Lead is widely recognized for its high toxicity and environmental persistence. Chronic exposure to Pb(II) can cause severe damage to the nervous, reproductive, and hematopoietic systems, leading to health disorders such as anemia, renal failure, liver dysfunction, bone abnormalities, hallucinations, coma, and even death [3].

Cadmium contamination results mainly from industrial activities such as steel and cement production, NiCd battery manufacturing, phosphate fertilizers, and electroplating [4]. According to the World Health Organization (WHO, 2010) [5], the permissible concentration of cadmium in drinking water should not exceed 0.003 mgůL^{-1}. Exposure to Cd(II) has been associated with renal dysfunction, skeletal deformities, testicular atrophy, and muscular disorders [6].

Copper, though an essential trace element for enzyme activity and bone development, becomes hazardous when present in excess. It is released from industries such as mining, electroplating, smelting, and electrical component manufacturing [7]. High levels of Cu(II) intake can cause nausea, vomiting, abdominal pain, liver and kidney failure, and respiratory complications [8, 9]. The USEPA has set a maximum discharge limit of 1.3 mgůL^{-1} of copper in industrial wastewater.

Because heavy metals are not biodegradable and tend to bioaccumulate through the food chain, they pose long-term risks to both ecosystems and human health. Therefore, effective treatment of metal-contaminated wastewater before environmental release is essential.

Several physicochemical and biological methods, such as electrochemical treatment, ion exchange, reverse osmosis, ozonation, photocatalysis, UV irradiation, bioremediation, and adsorption, have been explored for heavy metal removal [10]. Among these, adsorption is considered the most effective due to its high surface area, selectivity, reusability, low cost, and operational simplicity [11, 12].

A variety of adsorbents have been developed, including zeolites, polymers, activated carbon, biomass, and industrial by-products [13, 14]. However, these materials often suffer from limited adsorption capacity, poor selectivity, and low economic feasibility. To overcome these limitations, researchers have turned toward nanostructured metal oxides, which exhibit unique surface, structural, and physicochemical properties [15, 16].

Nickel oxide (NiO) nanoparticles, a well-known p-type semiconductor, have attracted significant interest due to their wide band gap (3.64.0 eV), chemical stability, optical and magnetic behavior, and catalytic versatility [17]. Likewise, manganese oxide nanoparticles (MnO, MnO_2, Mn_2O_3, and Mn_3O_4) are promising materials because of their multiple oxidation states, low cost, and excellent redox activity, making them suitable for environmental applications such as water purification [18, 19].

In recent years, the green synthesis of nanoparticles using plant extracts has emerged as an eco-friendly, cost-effective, and sustainable approach [20, 21]. Plant-based extracts are rich in bioactive compounds such as polyphenols, flavonoids, alkaloids, terpenoids, and vitamins, which act as reducing, capping, and stabilizing agents during nanoparticle formation [22].

Objectives of the Present Work

The main objective of this work is to develop a green and facile synthetic protocol for producing nickel oxide (NiO), manganese dioxide/manganese trioxide (MnO_2/Mn_2O_3), and trimanganese tetraoxide (Mn_3O_4, hausmannite) nanoparticles using an aqueous extract of *Helianthus annuus* seed husks (sunflower husks) as a biogenic reducing, capping, and stabilizing agent. The study further aims to evaluate their adsorptive performance toward removing Pb(II), Cd(II), and Cu(II) ions from aqueous solutions under different physicochemical conditions.

- Synthesizing NiO, MnO_2/Mn_2O_3, and Mn_3O_4 nanoparticles through an environmentally benign, cost-effective green method.

- Confirming nanoparticle formation using UVVis spectroscopy, and identifying the role of phytochemicals in reduction and stabilization via FTIR analysis.

- Determining crystalline structure and size using XRD, and investigating surface morphology by SEM.
- Assessing elemental composition using EDX and evaluating surface area through BET analysis.
- Studying the influence of adsorbent dose, pH, contact time, initial metal ion concentration, and temperature on adsorption efficiency.
- Modeling adsorption behavior using kinetic and isotherm models to understand the mechanisms involved.

Thesis Organization

This research work is divided into four main chapters:

- **Chapter I:** Provides a comprehensive literature review on metal oxide nanoparticles, including their properties, classification, synthesis methods, and environmental applications.
- **Chapter II:** Discusses water pollution by heavy metals, adsorption principles, and the factors affecting adsorption efficiency.
- **Chapter III:** Describes the experimental methodology, detailing the green synthesis of nanoparticles, characterization techniques, and adsorption experiments.
- **Chapter IV:** Presents and discusses the results on the green synthesis, structural characterization, and adsorption performance of NiO, MnO_2/Mn_2O_3, and Mn_3O_4 nanoparticles for the removal of Pb(II), Cd(II), and Cu(II) ions from wastewater.

Chapter I

Literature Review

Chapter I

Literature Review

I.1 Nanoscience and Nanotechnology

I.1.1 Definition

The term *nano* originates from Greek, meaning “dwarf” or extremely small, and refers to one-billionth of a meter. It is important to distinguish between **nanoscience** and **nanotechnology**. Nanoscience focuses on understanding materials and structures at the nanoscaletypically between 1 and 100 nanometerswhile nanotechnology applies this knowledge to develop practical tools and devices [23].

The conceptual roots of nanoscience date back to the fifth century B.C., during the era of Democritus and ancient Greek philosophers, who debated whether matter could be divided infinitely or if it consisted of fundamental, indivisible particles called atoms [24].

In the United States, nanotechnology is defined as “a science, engineering, and technology conducted at the nanoscale, where unique phenomena enable novel applications across a wide range of fields” [25].

It is essential to understand the distinction between nanoscience and nanotechnology. Nanoscience integrates physics, materials science, and biology to investigate materials at the atomic and molecular levels. In contrast, nanotechnology focuses on **manipulating matter at the molecular and nanoscale to create novel nanoparticles with controlled morphologies and sizes** [26]. The rapid development of this field opens new opportunities in both fundamental research and practical applications, such as the design of nanoscale materials and the study of their unique optical and physicochemical properties [27, 28].

I.1.2 Nanomaterials

Nanomaterials are materials with at least one dimension smaller than approximately 100 nanometers. At this scale, materials often exhibit unique optical, magnetic, electrical, and chemical properties, making them highly attractive for scientific research and technological applications [29].

Classification of Nanomaterials

Nanomaterials are generally classified into three categories [30]:

- **Nanocharged or nanoreinforced materials**: Materials obtained by incorporating nanoparticles into an organic or mineral matrix to enhance mechanical, optical, magnetic, or thermal properties, or to introduce new functionalities.
- **Surface nanostructured materials**: Surfaces engineered to acquire novel properties (e.g., hydrophilicity, abrasion resistance) or enhanced functionalities (e.g., hardness, adhesion).
- **Volume nanostructured materials**: Materials possessing an intrinsic nanometric structure that imparts specific physical properties.

I.2 Nanoparticles

A **nanoparticle** is an assembly of a few hundred to a few thousand atoms, with at least one dimension between 1 and 100 nm, and can be composed of metals, metal oxides, carbon, or organic materials [31, 32]. Compared to their bulk counterparts, nanoparticles exhibit distinct chemical, physical, and biological properties [33], making them highly valuable for a wide range of applications. Nanoparticles differ not only in composition but also in size, shape, and dimensions [34].

I.2.1 Nanoparticle Classification

Nanoparticles can be classified according to their size, structural form, and chemical composition.

Dimensionality [35]

- **Zero-dimensional (0D) nanoparticles**: Materials with no dimension in the nanoscale, arranged randomly, haphazardly, or in an ordered fashion, such as magnetic fluids or colloidal crystals for optical applications.
- **One-dimensional (1D) nanoparticles**: Materials shaped as nanowires or nanotubes.
- **Two-dimensional (2D) nanoparticles**: Materials forming thin layers, such as aggregated deposits or thick coatings fabricated via electrochemical deposition or plasma projection techniques.
- **Three-dimensional (3D) nanoparticles**: This category includes thin films with atomic-level porosity, colloidal systems [36], and densely packed nanoparticles in ceramics and metallic nanostructures [35, 37].

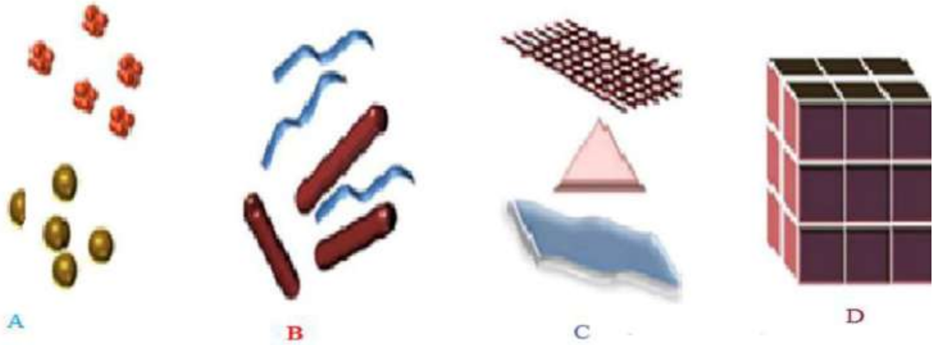

Figure I.1: Nanomaterial classification based on dimensions: A-zero-dimensional; B-one-dimensional; C-two-dimensional; D-three-dimensional

Nanoparticle Composition

Nanoparticles are generally classified into three main categories: carbon-based, inorganic, and organic nanoparticles.

Organic Nanoparticles Common examples of organic nanoparticles or polymer-based nanoparticles include micelles, ferritin, liposomes, and dendrimers. These nanoparticles are typically biodegradable and non-toxic. Certain types, such as liposomes and micelles, feature a hollow interior, often termed a **nanocapsule** (Figure I.2). They are also responsive to electromagnetic and thermal stimuli, including light and heat [38, 39].

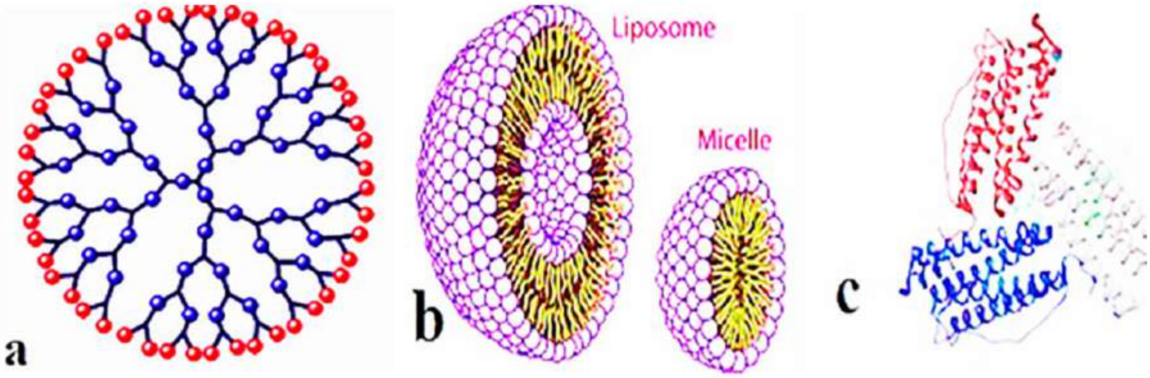

Figure I.2: Organic nanoparticles: a Dendrimers, b Liposomes and micelles, C Ferritin. micelles

Inorganic Nanoparticles Inorganic nanoparticles do not contain carbon and typically consist of metals or metal oxides.

- **Metal nanoparticles**: Metals can be engineered into nanoparticles using various synthesis methods. Common metals include aluminum, cadmium, cobalt, copper, gold, iron, lead, silver, and zinc [40, 41]. Metal nanoparticles exhibit crystalline or amorphous structures and can have shapes such as spheres or cylinders. They are distinguished by color, reactivity, and sensitivity to environmental factors such as heat, humidity, air, and sunlight.
- **Metal oxide nanoparticles**: Metal oxides are often synthesized to enhance the properties of their corresponding metal nanoparticles. They typically exhibit higher reactivity than pure metals, making them suitable for various applications [42]. Examples include zinc oxide, silicon dioxide, iron oxide, aluminum oxide, cerium oxide, titanium dioxide, nickel oxide, manganese oxide, and magnetite.

Carbon-Based Nanoparticles Carbon-based nanoparticles consist entirely of carbon [43, 44]. Examples include fullerenes, graphene, carbon nanotubes (CNTs), carbon nanofibers, carbon black, and occasionally nanoscale activated carbon, as illustrated in Figure I.3.

Nanoparticle Morphology

Important morphological traits include **aspect ratio, sphericity, and flatness** [45]. High aspect ratio nanoparticles, such as nanotubes or nanowires, can exhibit geometries including

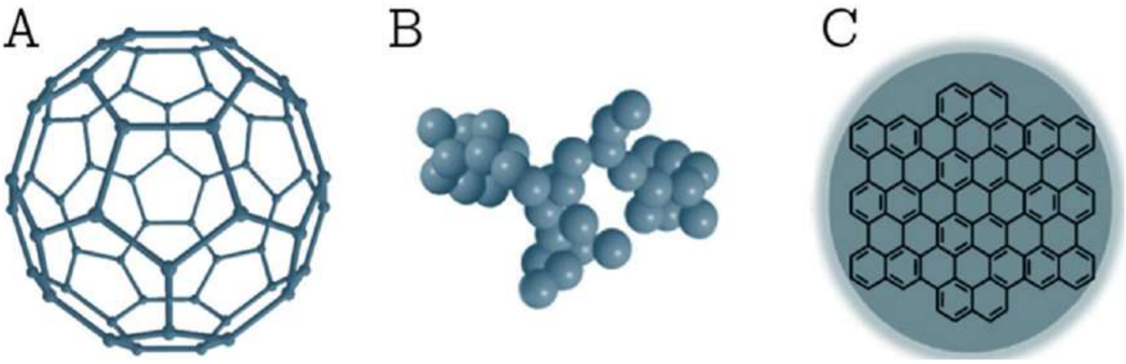

Figure I.3: Various kinds of NPs based on carbon: A C60 fullerene; B carbon black NPs; and C carbon quantum dots .

belts, zigzags, or helices. Low aspect ratio nanoparticles include shapes such as helix, pillar, prism, oval, cubic, and spherical forms. Nanoparticles are typically studied as colloids, suspensions, or powders [46].

I.2.2 Properties of Nanoparticles

Surface Properties

Nanoparticles exhibit unique properties primarily due to the high proportion of surface atoms relative to those in the core. As nanoparticles adopt a spherical shape, both their surface area-to-volume ratio and the fraction of surface atoms increase (Table I.1). This effect becomes more pronounced as particle size approaches the nanoscale, where the dominance of surface atoms significantly influences the overall behavior and characteristics of the nanoparticles [47].

Table I.1: Relationship between the number of surface atoms and particle size

Nanoparticle Size (nm)	Number of Atoms in the Particle	Proportion of Surface Atoms (%)
1	30	99
2	2.5×10^2	80
4	4×10^3	60
5	4.2×10^4	50
10	3×10^4	20

Optical Properties

Nanoparticles display optical behaviors that differ significantly from their bulk counterparts, including transmission, absorption, reflection, and emission of light. Due to their small size, electrons in nanoparticles are confined, resulting in **quantum confinement effects** [49, 50]. By modifying their size, shape, and surface functionalization, nanoparticles can exhibit a wide range of optical properties, which directly affect their perceived color. For example, spherical gold nanoparticles of 100 nm appear orange, whereas those around 25 nm appear green. Similarly, 100 nm spherical silver nanoparticles display a yellow color [50].

Electronic Properties

The electronic properties of metallic nanoparticles lie between those of bulk metals, which have continuous energy bands, and atoms, which have discrete energy states. Electrical resistance increases with decreasing particle size because a greater fraction of atoms resides on the particle surface [51].

I.2.3 Synthesis of Nanoparticles

Various techniques exist to synthesize nanoparticles (NPs) with controlled size, structure, shape, and composition. Two primary approaches are employed: **top-down** and **bottom-up** methods (Figure II.2).

Top-Down Approach The top-down approach involves breaking down bulk materials into smaller particles. While it can be less precise and produce defects, it is often simple and widely used. Common top-down techniques include mechanical milling, laser ablation, thermal decomposition, sputtering, and nanolithography [32, 52].

Bottom-Up Approach The bottom-up approach, also called the constructive method, builds nanoparticles from individual atoms or small clusters. This approach is generally more economical and minimizes material waste. Techniques include sol-gel processing, spinning, green synthesis, chemical vapor deposition, pyrolysis, and biosynthesis [53, 55].

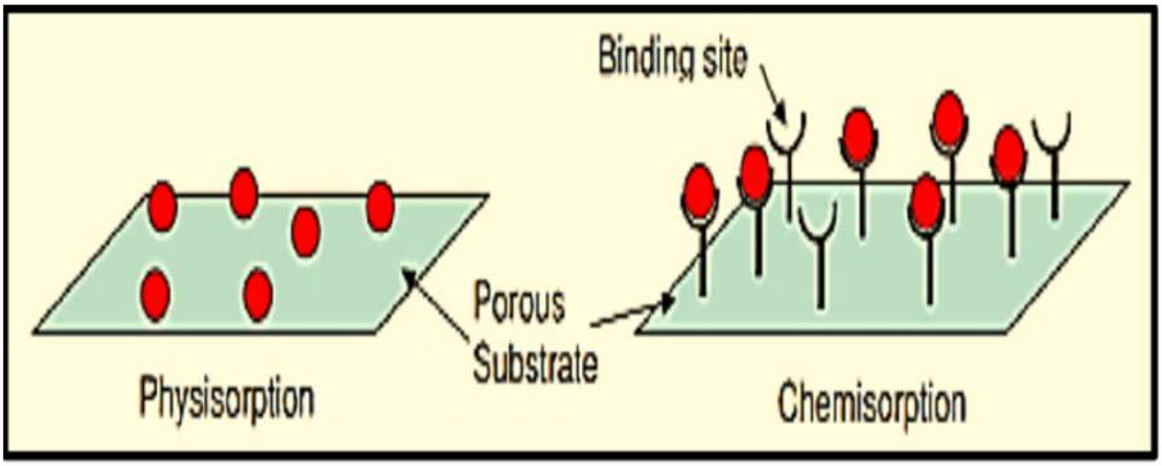

Figure I.4: Synthesis approaches for nanoparticles: top-down and bottom-up methods .

I.2.4 Green Synthesis of Nanoparticles Using Plant Extracts

The use of plants for nanoparticle synthesis offers accessibility, safety, and abundant metabolites that can act as natural reducing and stabilizing agents. Green synthesis relies on three main elements: a safe stabilizing agent, a non-toxic reducing agent, and an environmentally friendly solvent, typically water, ethanol, or a mixture of both [56]. Various plant partsleaves, fruits, roots, stems, and seedshave been employed in the synthesis of nanoparticles [57].

For example, living alfalfa plants have been used to produce gold nanoparticles ranging from 2 to 20 nm [58]. Similarly, silver, nickel, cobalt, zinc, and copper nanoparticles have been synthesized using plants such as *Helianthus annuus* (sunflower), *Medicago sativa* (alfalfa), and *Brassica juncea* (Indian mustard). These plants contain phytochemicals like alkaloids, phenols, terpenoids, quinones, amides, flavonoids, proteins, and alcohols, which facilitate reduction and stabilization of nanoparticles. Plant-based nanoparticles often exhibit enhanced biological potential compared to chemically synthesized ones and can be applied in bioengineering, agriculture, food technology, cosmetics, nanomedicine, and human health, while posing fewer adverse effects [59, 60].

The green synthesis process generally involves three stages: **reduction, growth, and termination** (Figure I.5). During reduction, metal ions are converted into zero-valent metal atoms by electron transfer facilitated by phytochemicals. During growth, these atoms aggregate into nanoparticles with various shapes, including linear, rod-shaped, triangular, hexagonal, or cubic. Finally, in the termination stage, the nanoparticles are stabilized by enrichment with phytoactive compounds possessing antioxidant properties [61, 62].

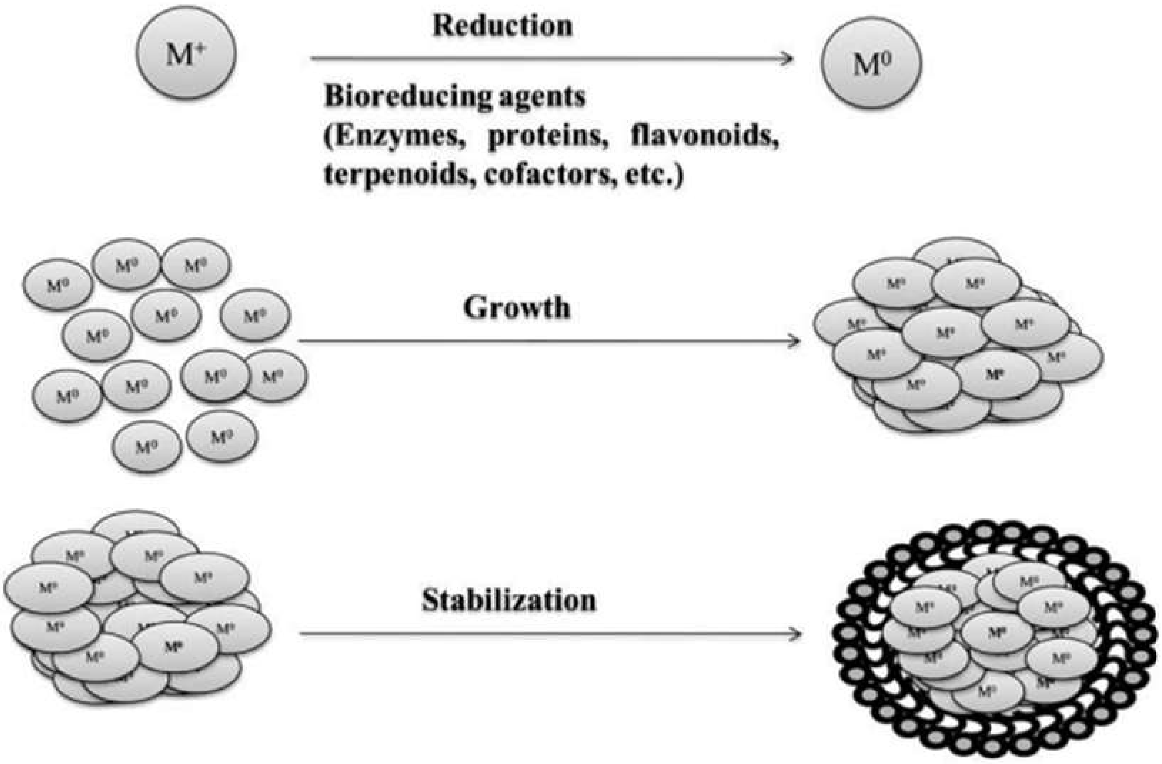

Figure I.5: Mechanism of nanoparticle synthesis using plant extracts.

I.3 Metal Oxide Nanoparticles

I.3.1 Nickel Oxide Nanoparticles (NiO)

Metal oxides are a diverse group of compounds formed by the combination of metals with oxygen. They play a crucial role in materials science, physics, and chemistry due to their wide range of structural arrangements and the ability of metal elements to form different types of bonds with oxygen. Consequently, metal oxides can exhibit metallic, semiconducting, or insulating behavior, making them highly versatile materials [63].

Nickel oxide (NiO) is of particular interest due to its magnetic and chemical characteristics [64]. NiO is a green crystalline solid with a cubic structure and ferromagnetic properties. Its unique electrical, magnetic, and optical features have attracted significant attention in scientific research. NiO also exhibits a relatively wide band gap of 3.64.0 eV [65, 67]. Some of its key properties are listed in Table I.2.

Table I.2: Physical properties of NiO

Property	NiO
Structure	Cubic
Band gap	3.64.0 eV
Refractive index	2.82
Density	6.67 g/cm^3
Melting point	1900 °C
Neel temperature (T_N)	523 K
Dielectric constant	10.31
Exciton binding energy	50 meV

Crystal Structure of NiO

Nickel oxide has a face-centered cubic (FCC) crystal structure, similar to sodium chloride (NaCl) [68, 69]. Oxygen (O^{2-}) and nickel (Ni^{2+}) ions occupy octahedral sites, as shown in Figure I.6.

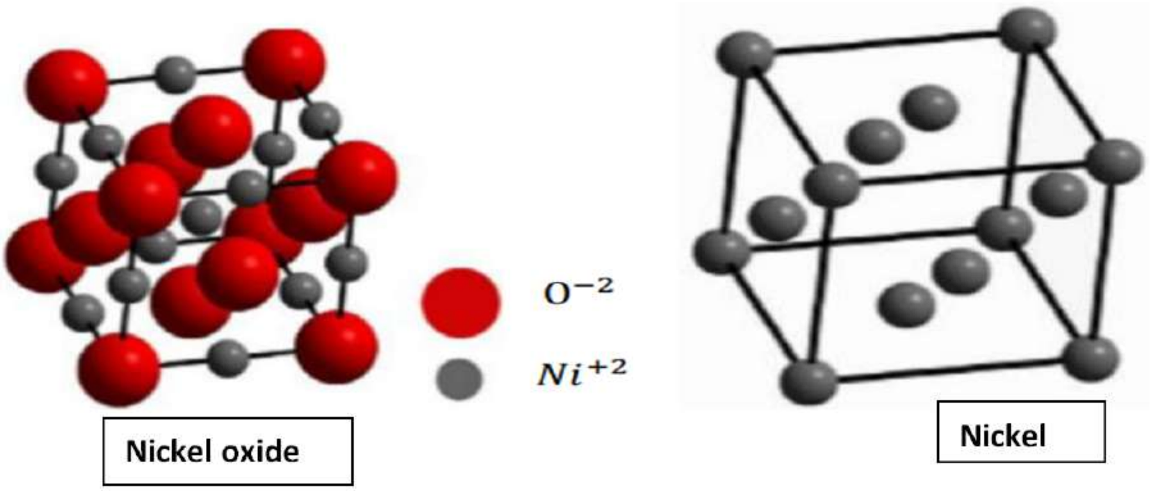

Figure I.6: Crystal structure of nickel oxide (NiO) .

I.3.2 Manganese Oxide Nanoparticles

Manganese oxides are increasingly studied due to their wide applications, high surface area, abundance of surface atoms, non-toxic nature, and well-defined physical and chemical properties across various crystal structures [70]. Manganese oxides exhibit multiple oxidation states (+2, +3, +4) and can form nanostructures such as MnO, MnO_2, Mn_2O_3, and Mn_3O_4 [71]. They are widely used as green catalysts in various chemical processes [72].

Manganese Dioxide (MnO_2)

Manganese dioxide occurs naturally as pyrolusite and has a blackish-brown color. Its empirical formula is MnO_2, with manganese and oxygen atoms forming an ionic bond. MnO_2 is suitable for semiconductor applications, is soluble in ammonia and water, but insoluble in acids [73]. Its main properties are summarized in Table I.3.

Table I.3: General properties of MnO_2.

Property	**MnO_2**
Molecular formula	MnO_2
Molar mass	86.9368 g/mol
Appearance	Brown-black solid
Density	5.026 g/cm^3
Melting point	535 °C (decomposes)
Solubility in water	Insoluble
Flash point	535 °C
Surface area (m^2/g)	2260
Band gap	2.32.5 eV

Crystal Structure of MnO_2

MnO_2 consists of one manganese atom bonded to two oxygen atoms via one sigma and one pi bond each. Figure I.7 shows its well-organized crystal structure.

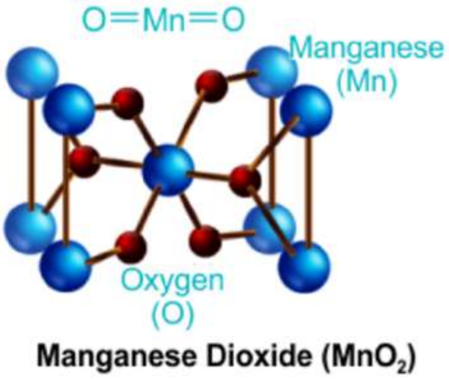

Figure I.7: Crystal structure of manganese dioxide (MnO_2).

Dimanganese Trioxide (Mn_2O_3)

Dimanganese trioxide is valued for its chemical stability, catalytic activity, and microbicidal properties [74, 75, 76]. Its physical and chemical properties are listed in Table I.4.

Table I.4: Physical and chemical properties of Mn_2O_3

Property	**Mn_2O_3**
Chemical formula	Mn_2O_3
Molar mass	157.8743 g/mol
Appearance	Brown or black crystalline
Density	4.50 g/cm^3
Melting point	888 °C
Solubility in water	Insoluble

Trimanganese Tetraoxide (Mn_3O_4)

Mn_3O_4, also known as hausmannite, contains manganese in both +2 and +3 oxidation states and can be represented as $MnOMn_2O_3$ [76, 77]. Its general properties are shown in Table I.5.

Table I.5: Physical and chemical properties of Mn_3O_4 .

Property	**Mn_3O_4**
Chemical formula	Mn_3O_4
Molar mass	228.812 g/mol
Appearance	Brownish-black powder
Density	4.8 g/cm^3
Melting point	1564 °C
Solubility in water	None

Crystal Structure of Mn_3O_4

Mn_3O_4 adopts a conventional spinel structure, with Mn^{2+} ions occupying tetrahedral sites and Mn^{3+} ions occupying octahedral sites. The lattice constants are $a = b = 5.765$ Å and $c = 9.442$ Å. The crystal structure is shown in Figure I.8.

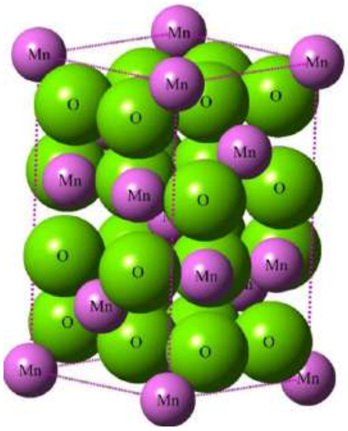

Figure I.8: Crystal structure of trimanganese tetraoxide (Mn_3O_4).

I.4 Synthesis and Applications of Metal Oxide Nanoparticles

I.4.1 Synthesis of Nickel Oxide Nanoparticles (NiO)

Nanoparticle synthesis can be broadly classified into two main approaches: **top-down** and **bottom-up** (Figure **??**). The top-down approach involves breaking down bulk materials into nanoscale components using various physical and chemical techniques [78]. This method allows for rapid and large-scale production of nanomaterials; however, it often introduces surface defects, which can alter the physical, chemical, and surface properties of the nanoparticles [79, 80].

In contrast, the **bottom-up approach** builds nanoparticles from atoms, molecules, or small clusters through self-assembly. Techniques include chemical methods such as sol-gel, precipitation, hydrothermal, solvothermal, and chemical reduction, as well as biological synthesis methods. The bottom-up approach is generally preferred because it produces nanoparticles with fewer defects, uniform composition, and controlled surface structures [80].

Several **physical and chemical methods** have been reported for the synthesis of NiO nanoparticles. Physical methods include mechanical milling [81, 82], sputtering [83], spray pyrolysis [84], chemical vapor deposition (CVD) [85], and laser ablation [86, 87]. For example, spray pyrolysis of nickel chloride hexahydrate yields NiO nanoparticles with average sizes of 25–30 nm [88], while CVD can also produce NiO nanoparticles [85]. Similarly, the anodic arc plasma technique has been employed to synthesize spherical NiO nanoparticles averaging 25 nm in size [89]. These physical methods, however, require high energy, specialized equipment, and skilled personnel, which can limit large-scale and cost-effective production.

Chemical synthesis techniques for NiO nanoparticles include hydrothermal [90], sonochemical [91], solvothermal [92], chemical reduction [93], sol-gel [94], and microemulsion [95] methods. Stabilizing agents, such as ethylene glycol, isopropanol, and nickel nitrate hexahydrate, are often used to control particle morphology [96]. Surfactants like Triton X-100 prevent aggregation and ensure uniform particle distribution. For instance, a simple solvothermal approach using citric acid as a chelating agent and nickel nitrate as a precursor successfully produces NiO nanoparticles with controlled morphology [97]. NiO nanoparticles have also been prepared via chemical precipitation without surfactants or capping agents [98], and through combustion using organic fuels [99].

I.4.2 Environmentally Friendly Production of Nickel Oxide Nanoparticles Using Plant Extracts

Recently, the use of plant extracts and their components for the synthesis of nanoparticles has gained significant attention due to its simplicity, cost-effectiveness, rapid process, and eco-friendly nature. Various plant species have been explored for the green synthesis of NiO nanoparticles. In this method, phytochemicals present in the plant extracts play a key role in reducing nickel ions [100, 101]. Functional groups such as the carbonyl and hydroxyl groups in amino acids, as well as the polyphenols and hydroxyl groups in flavonoids, contribute to the reduction process and help stabilize the formed nanoparticles.

For example:

- *Nephelium lappaceum* L. extract was successfully used to synthesize NiO nanocrystals of roughly 50 nm in size. The phenolic compounds in the extract were primarily responsible for the nanoparticle formation [102].
- NiO nanoparticles were biosynthesized using leaf extract from *Moringa oleifera* [103].
- *Azadirachta indica* extract was used to create oblong-shaped NiO nanoparticles of 12 nm, showing exceptional antibacterial activity against *S. aureus* and *E. coli* [104].
- An aqueous leaf extract of *Aegle marmelos* was employed to synthesize spherical NiO nanoparticles with sizes ranging from 8 to 10 nm. The plant extract acted as both reducing and capping agent. These nanoparticles demonstrated strong anticancer activity against A549 cell lines [100].
- Ali Talha Khalil et al. used *Sageretia tea* (Osbeck.) leaves to synthesize spherical NiO nanoparticles of 18 nm, as confirmed by XRD and SEM/TEM analyses. The biological effects of the nanoparticles were also studied [105].
- P. Kganyago et al. reported the green synthesis of NiO nanoparticles using *Monsonia burkeana* leaves. The resulting nanoparticles were spherical with an average size of 20 nm, as demonstrated by XRD and TEM studies [105].

To date, the biosynthesis of NiO nanoparticles has employed a variety of plant extracts with different phytochemical compositions. Despite the diversity of plant sources, the size, shape, and morphology of NiO nanoparticles can vary significantly depending on experimental parameters such as temperature, pH, contact time, and the concentrations of nickel ions and plant extract.

I.4.3 Eco-Friendly Synthesis of Manganese Oxide Nanoparticles Using Plant Extracts

Manganese oxides have attracted significant interest among the various 3*d* transition metal oxides due to their rich diversity in both structure and composition, encompassing phases such as MnO, Mn_5O_8, Mn_2O_3, MnO_2, and Mn_3O_4 [106].

For example:

- Khan et al. [107] used *Abutilon indicum* leaf extract to synthesize MnO nanoparticles with a diameter of approximately 85 nm. Phytomolecules such as flavonoids, phenolics, and carbohydrates contributed electrons via redox reactions, reducing Mn^+ to its zero-valent species, Mn^0, while other biomolecules including proteins and alkaloids helped stabilize Mn^0.

- *Viola betonicifolia* leaf extract was employed to produce MnO_2 nanoparticles, which exhibited superior cytotoxic, antibacterial, and antioxidant properties compared to the pure extract. Characterization revealed highly crystalline, spherical, and uniformly distributed MnO_2 nanoparticles with a size of 10.5 nm [108].

- Other plant extracts used for MnO_2 nanoparticle synthesis include green tea [109], *Leucaena leucocephala* [110], and *Caryota mitis* Lour (fishtail palm) flower [111].

- Diallo et al. [112] utilized manganese chloride and an *Aspalathus linearis* extract to synthesize Mn_3O_4 nanoparticles with diameters ranging from 18 to 28 nm.

- Additional studies reported Mn_3O_4 synthesis using extracts from *Simarouba glauca* leaf [113], Adalodakam [114], *Ananas comosus* (L.) peel [115], *Azadirachta indica* [116], *Costus woodsonii* flower [117], green gram powder [118], and others.

I.5 Applications of Nanoparticles

I.5.1 Application of Nickel Oxide Nanoparticles

NiO nanoparticles have recently garnered considerable attention due to their remarkable optical, electrical, and magnetic properties, along with their high chemical stability and excellent conductivity characteristics [119]. They have found use in various applications, including:

- Supercapacitor electrode materials.
- Diffusion bonding of stainless steel.
- Nitrobenzene hydrogenation.
- Low-temperature oxidation of carbon monoxide and propane.
- Catalysis of hydrogen auto-transfer and transfer hydrogenation reactions [120, 121].

NiO nanoparticles can also serve as environmentally friendly adsorbents to determine water's chemical oxygen demand (COD) and remove contaminants and dyes from tannery and textile industry effluents [122]. Under *in vitro* and greenhouse conditions, they exhibit antifungal activity against pathogens causing wilt in tomatoes and lettuce [123]. Additionally, NiO nanoparticles possess numerous catalytic and therapeutic properties, including antioxidant, anticancer, cytotoxic, antifungal, antibacterial, enzyme inhibition, and other remedial activities [124, 125]. Their unique surface area, capacity to release and absorb metal ions, and cytotoxic properties make them useful as biomedicines for therapeutic applications [126].

I.5.2 Application of Manganese Oxide Nanoparticles

Manganese oxide nanoparticles have attracted attention as anode materials in lithium-ion batteries due to their exceptional properties, low cost, low environmental impact, and high theoretical capacity [127]. Their distinct physical and chemical characteristics have enabled applications in molecular adsorption, ion exchange, catalysis, energy storage, and biosensors, making them highly valuable inorganic materials [128]. Moreover, MnO nanoparticles have been employed in wastewater treatment, supercapacitors, sensors, catalysis, and rechargeable batteries [129].

I.6 Helianthus annuus L. (Sunflower)

I.6.1 Taxonomical Classification

- Kingdom: Plantae
- Division: Angiospermae
- Subdivision: Eudicots
- Class: Asterids
- Order: Asterales
- Family: Asteraceae
- Subfamily: Helianthoideae [130]

Figure I.9: Flower of *Helianthus annuus* L.

I.6.2 Botanical Description

Helianthus annuus L., the common sunflower, is an annual herbaceous crop growing 13 m high [132]. Its name derives from Greek "helios" (sun) and "anthus" (flower), while *annuus* indicates it is annual. It is native to temperate regions (2025°C) and produces a large, yellow flower head that follows the sun.

- **Roots:** Initially tap-rooted, maturing to a large, fibrous, lateral root system.
- **Stems:** Spherical, branching, hispid, 30200 cm tall; herbage harsh and dull.

- **Leaves:** Upper leaves alternate, lower leaves mostly opposite; blades 420 cm long, 315 cm wide, serrated edges, acute apex.
- **Inflorescence:** Large composite heads, terminal or axillary, peduncles 220 cm long.
- **Flowers:** Single or double; yellow ray florets, brownish-purple disc florets, flat or convex receptacles [133].
- **Fruit:** Sunflower seeds with protective rinds; oilseed varieties have shells for pest protection [132].

I.6.3 Distribution

Helianthus annuus, commonly known as the sunflower, is a pervasive roadside weed. It is widely distributed in open habitats at elevations below 1900 meters across southern Canada, Mexico, and North America. As a species, *H. annuus* exhibits considerable diversity and readily hybridizes with several other species [134].

I.6.4 Phytochemistry and Chemical Constituents

The methanolic extract of *H. annuus* seeds has been reported to contain carbohydrates, flavonoids, tannins, alkaloids, saponins, phytosterols, steroids, and fixed oils, while lacking proteins, starch, and glycosides [135].

Kamal et al. identified allelochemicals in sunflower leaves, stems, and roots using thin layer chromatography (TLC) for alkaloids and spectrophotometry for phenols and flavonoids. The concentration of allelochemicals was found to be highest in the leaves, followed by the roots and stems [136].

Sunflower seed shells are rich in antioxidant phenolic compounds. Phenolic content in antioxidant seeds ranges from 2% to 4%, while 43% to 73% of phenolics are present in sunflower kernels [137].

I.6.5 Uses

Sunflower seeds are widely consumed by humans, either as roasted snacks or processed into oil. Peeled sunflower seeds are a common protein substitute, frequently incorporated into vegetarian diets [138].

Sunflower hulls, which represent 2130% of the total seed weight, are often considered a by-product. They can be used in small amounts as a source of fiber in animal feed, though excessive quantities may impair digestion. Hulls are commonly burned in oil extraction facilities to provide heat during processing and for the distillation of hexane solvent. They have also been processed into cylinders as artificial fireplace logs or used to heat public buildings near processing plants with minimal boiler modifications [137]. Additionally, sunflower hulls serve as a supplementary fuel source for coal-fired power plants [139].

Chapter II

Wastewater and the Adsorption Technique

Chapter II

Wastewater and the Adsorption Technique

Introduction

The majority of emerging pollutants in wastewater streams are chemical compounds that are not biodegradable, causing major issues for ecosystems and living organisms [140]. Both organic and inorganic pollutants originate from multiple sources such as households and industries, with long-lasting negative impacts on biodiversity and human and animal health [141]. Wastewater contains hazardous materials including heavy metals, which pose serious threats to the environment and human health, contributing to diseases like cancer and respiratory disorders [142]. Various techniques can remove heavy metals, such as chemical precipitation, biosorption, adsorption, filtering, and ion exchange. Among these, adsorption is the most effective, cost-efficient, and practical method [143].

II.1 Heavy Metal-Contaminated Wastewater

Heavy metals are major contaminants of freshwater ecosystems due to their toxicity and persistence. They are typically characterized by atomic densities exceeding 5 g/cmş and relative atomic masses between 63.5 and 200.6 [144]. Persistent in wastewater and non-biodegradable, heavy metals contribute to global environmental pollution [145, 146], highlighting the need for effective water quality control [147].

Sources include natural processes (weathering, soil erosion, volcanic eruptions, aerosols) and human activities such as industrial and municipal effluents. Industrial wastewater comes from metal smelting, electroplating, leather tanning, textiles, mineral extraction, and nuclear power, while urban wastewater originates from municipal discharges [148, 149, 150]. Heavy metals must be removed before discharge due to their non-biodegradable nature [145, 147].

II.1.1 Common Heavy Metals in Wastewater

Heavy metals accumulate in the environment, posing toxic risks and potential cancer hazards due to bioaccumulation [151, 152]. Table II.1 summarizes common heavy metals, their sources, affected organs, and permissible limits in drinking water according to WHO [153, 154, 155].

Table II.1: Common heavy metals in wastewater, sources, health effects, and permissible levels

Metal	Primary Sources	Affected Organs/Systems	Permitted Level (µg/L)
Lead (Pb)	Solder, alloys, paints, batteries, ammunition	Immune, hematological, cardiovascular, brain, lungs, spleen, liver, kidneys, reproductive	10
Arsenic (As)	Glass manufacturing, electronics	Kidneys, brain, lungs, skin, cardiovascular, metabolic, immune, endocrine	10
Copper (Cu)	Electrical, cable, plumbing	Gastrointestinal, lungs, liver, brain, kidneys, cornea, immune, hematological	2000
Zinc (Zn)	Brass coating, rubber, cosmetics, aerosol deodorants	Stomach, skin, anemia, nausea, vomiting, convulsions	3000
Chromium (Cr)	Tanneries, steel, pulp mills	Gastrointestinal, liver, kidneys, brain, pancreas, skin, lungs, reproductive	50
Cadmium (Cd)	Metal refineries, paints, batteries, steel/plastic industries	Brain, immune, cardiovascular, lungs, testes, liver, kidneys, bones	3
Mercury (Hg)	Refineries, industrial devices, electrical appliances, landfill runoff	Reproductive, cardiovascular, neurological, endocrine, lung, renal, liver, immune	6
Nickel (Ni)	Nickel alloys, stainless steel manufacturing	Skin, renal, pulmonary fibrosis, gastrointestinal, lungs	70

II.2 The Heavy Metal Remediation Technologies

Heavy metals can accumulate within human food chains through a process known as bioaccumulation, leading to progressively higher concentrations of metal ions that pose risks to living organisms. These contaminants often enter aquatic environments via various sources such as household and industrial discharges, agricultural runoff, and certain wastewater treatment practices [156].

To mitigate metal contamination in wastewater, a variety of treatment methods are employed. These methods are generally classified into three main categories: physical, chemical, and biological [157]. While biological approaches are typically slower and less efficient than physical or chemical treatments, they are often more cost-effective [158].

II.3 Adsorption

Currently, the most feasible and efficient method for removing heavy metals from wastewater is the adsorption process [159, 160]. Adsorption allows for the complete recovery of heavy metals from wastewater and provides operational and design flexibility.

The adsorption process involves transferring heavy metal ions (adsorbate) from the wastewater onto a solid surface called the adsorbent, where they attach either chemically or physically. Physical adsorption arises from mild van der Waals forces, whereas chemical adsorption occurs due to the formation of strong covalent bonds between the adsorbent and adsorbate [161, 162].

II.3.1 Types of Adsorption

Adsorption is classified as physical (physisorption) or chemical (chemisorption), depending on bond type and energy [163, 164, 165]. Figures II.1 and II.2 illustrate these processes.

II.3.1.1.Physical Sorption (Physisorption)

Physisorption occurs at low temperatures (<40 kJ/mol) and involves weak Van der Waals forces. It is rapid, reversible, and does not alter chemical composition [166, 167].

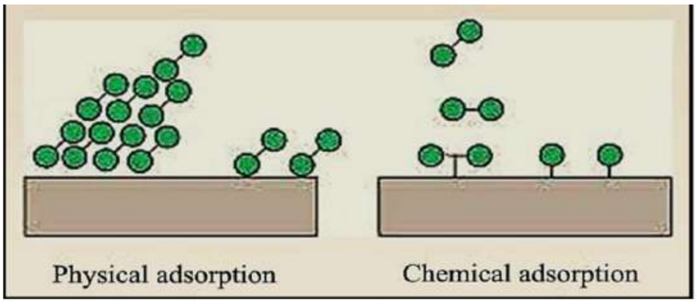

Figure II.1: Physical and chemical adsorption

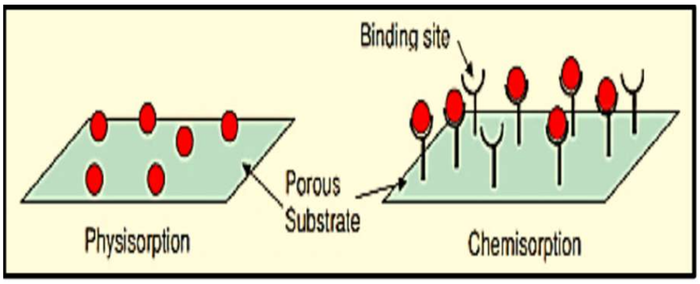

Figure II.2: Mechanism of physical and chemical adsorption

II.3.1.2.Chemical Sorption (Chemisorption)

Chemisorption involves ionic or covalent bonding, usually at high temperatures (>40 kJ/mol), potentially forming complexes with adsorbent surfaces [168, 169].

Table II.2: Comparison of physical and chemical adsorption

Criteria	Physical Adsorption	Chemical Adsorption
Specificity	Non-specific	Highly-specific
Nature	Depends on adsorbent	Depends on adsorbent
Reversibility	Reversible	Mainly irreversible
Enthalpy	20-40 kJ/mol	40-300 kJ/mol
Activation energy	Low	High
Adsorption layer	Multi-layer	Monolayer
Bonding	Weak Van der Waals, dipole-dipole	Strong ionic/covalent, chemical change

II.3.2 Mechanisms of Adsorption

The adsorption mechanism has four main steps [170, 171]:

1. Transport of solute to adsorbent boundary layer.

2. Diffusion through the boundary layer.

3. Transfer to active sites of adsorbent pores.

4. Adsorption into the solid phase.

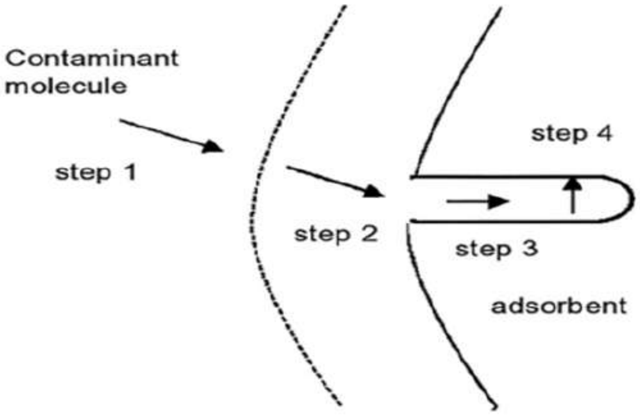

Figure II.3: Adsorption mechanism

II.4 Factors Affecting the Adsorption of Heavy Metals

A number of variables, such as temperature, pH, adsorbent dosage, initial concentration, and contact time, influence the efficiency of adsorption techniques [172].

II.4.1 Effect of Solution pH

The pH of the solution is a crucial parameter in the adsorption process, as determining the initial pH condition is key to optimizing pollutant removal. The pH affects the availability of hydrogen ions in functional groups, such as hydroxyl (OH), carboxyl (COOH), amine (NH), and metal ions on the adsorbent surface [173]. At lower pH levels, the abundance of H^+ ions tends to neutralize the negatively charged adsorbent surface, reducing electrostatic repulsion and facilitating diffusion, thereby enhancing the adsorption rate. However, studies have shown that adsorption efficiency generally improves at higher pH values and decreases as the pH lowers [174].

II.4.2 Effect of Adsorbent Dosage

The adsorbent dose is another important factor determining the adsorption efficiency of heavy metals. Increasing the adsorbent dose generally increases the amount of metal ions adsorbed due to more available active sites and higher surface area. However, beyond a certain point, the adsorption capacity tends to remain constant despite further increases in dosage [175, 176].

II.4.3 Effect of Contact Time

Contact time is used to characterize the adsorption capacity. The adsorption process requires a specific time to reach equilibrium, which corresponds to the stage where adsorption is complete [177]. The time required to reach maximum adsorption depends on the type of adsorbent and adsorbate.

II.4.4 Effect of Temperature

Temperature influences the physicochemical reactions involved in adsorption and is therefore a key factor. For exothermic adsorption processes, an increase in temperature typically decreases the reaction rate, while for endothermic processes, higher temperatures can enhance the adsorption rate [178].

II.4.5 Effect of Initial Concentration

The initial concentration of heavy metals significantly affects adsorption. Generally, as the initial concentration increases, the adsorption capacity also increases, because a higher concentration provides the driving force needed to overcome mass transfer resistance between the liquid and solid phases. However, higher initial concentrations may lead to a decrease in overall removal efficiency, as confirmed by several studies [177].

II.5 Adsorption Kinetics

The solute adsorption rate governs how long the adsorbate remains at the solution interface, as indicated by kinetic analysis. When designing and calculating adsorption systems, this rate plays a crucial role [179, 180]. The most commonly used kinetic models for adsorption studies are the pseudo-first-order and pseudo-second-order models.

II.5.1 Pseudo-First-Order Kinetics

The pseudo-first-order model, proposed by Lagergren, assumes a linear relationship between time and the amount of adsorbate accumulated on the adsorbent surface. It has been widely applied to characterize the adsorption behavior of organic and inorganic solutes on non-uniform solid surfaces. However, its applicability is generally limited to the first 20–30 minutes of adsorption and often fails to represent the entire contact time range in kinetic studies [181]. This model is usually expressed as:

$$\ln(q_e - q_t) = \ln q_e - k_1 t \tag{II.1}$$

where k_1 is the apparent rate constant, t is the contact time, and q_e and q_t are the amounts of metal ions adsorbed per unit mass of adsorbent at equilibrium and at time t, respectively [182].

II.5.2 Pseudo-Second-Order Kinetics

The pseudo-second-order model assumes that the adsorption rate is directly proportional to the square of the number of unoccupied active sites. This model provides a more accurate description of solute adsorption on solid surfaces compared to lower-order models [183]. It can be expressed as:

$$\frac{1}{q_t} = \frac{1}{q_e} - \frac{1}{k_2 q_e^2} \tag{II.2}$$

where k_2 is the rate constant of the pseudo-second-order adsorption process.

II.5.3 Intraparticle Diffusion Model

The intraparticle diffusion model can be employed to explain the diffusion mechanism within the adsorbent pores. Factors commonly affecting intraparticle diffusion include temperature, agitation speed, initial solute concentration, and physical properties of the adsorbent [184]. The intraparticle diffusion equation is given by:

$$q_t = k t^{0.5} + C \tag{II.3}$$

where k is the intraparticle diffusion rate constant and C represents the boundary layer effect [185].

II.6 Adsorption Isotherms

Adsorption isotherms are widely used to understand the adsorption mechanism. After the adsorption process, the residual concentration of metal ions is determined using an atomic absorption spectrophotometer. The efficiency of metal ion removal from the aqueous solution is subsequently calculated using the following formula [186]:

$$R\% = \frac{C_0 - C_e}{C_e} \times 100 \tag{II.4}$$

The metal uptake (q_e) at equilibrium can be determined using:

$$q_e = \frac{(C_0 - C_e)}{m} \times V \tag{II.5}$$

where C_0 and C_e are the initial and equilibrium metal concentrations (mg/L), V is the solution volume (L), and m is the adsorbent mass (g).

II.6.1 Classification of Adsorption Isotherms

Sorption isotherms have been categorized by several authors, including Gilles and Coll, according to their shape and initial slope [187, 188]. A summary of this classification is as follows (Figure II.4):

- **Kind “H” isotherms:** Dubbed “high affinity” isotherms, which are a special case of the “L” type. The solute exhibits extremely strong affinity for the solid, resulting in an initial slope so steep that it is practically infinite, even if thermodynamically unusual.

- **Kind “L” isotherms:** Known as “Langmuir” isotherms, they typically correspond to low solute concentrations in water. The convex shape of the isotherm indicates gradual saturation of the adsorbent. As C_e approaches zero, the slope of the isotherm remains constant, suggesting that bifunctional molecules adsorb flatly.

- **Kind “S” isotherms:** Termed “sigmoidal” isotherms, characterized by a distinct inflection point, generally resulting from at least two competing adsorption mechanisms.

This occurs, for instance, when adsorption of subsequent solute layers is favored after the first layer.

- **Kind "C" isotherms:** Called "constant partition" isotherms, represented by a straight line passing through the origin. This indicates that the distribution coefficient K_d (or q_e/C_e ratio) remains constant [188, 189].

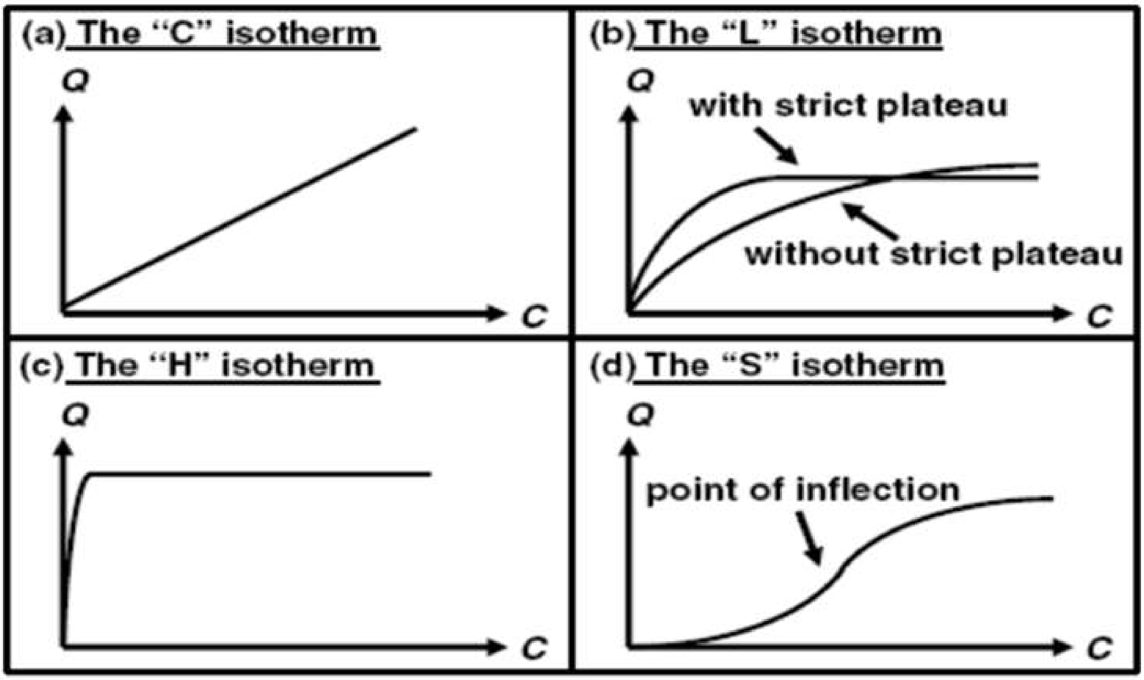

Figure II.4: Types of adsorption isotherms

II.6.2 Modeling of Adsorption Isotherms

When discussing solid-liquid adsorption, two-parameter models are most frequently employed in the literature, such as Freundlich, Langmuir, DubininRadushkevich, Temkin, and Elovich models.

Freundlich Isotherm

The Freundlich isotherm is an empirical model that considers the interference of the solute's adsorption in a mono-molecular layer. It assumes a heterogeneous adsorbent surface with distinct binding sites [190]. The non-linear form of the Freundlich isotherm is given by:

$$q_e = K_F C_e^{1/n} \tag{II.6}$$

where K_F is the adsorption capacity (L/mg) and $1/n$ is the adsorption intensity.

The value of $1/n$ characterizes the type of isotherm:

- $1/n = 0$: irreversible isotherm
- $0 < 1/n < 1$: favorable isotherm
- $1/n > 1$: unfavorable isotherm

The Freundlich isotherm can also be expressed in a linearized form:

$$\log q_e = \log K_F + \frac{1}{n} \log C_e \tag{II.7}$$

Langmuir Isotherm

The Langmuir model is the most widely used representation of adsorption phenomena in aqueous solutions [191]. It postulates that adsorption occurs on a finite number of distinct localized sites and that the adsorbed layer is monolayer (one molecule thick) [192]. The non-linear form is given by:

$$q_e = \frac{q_m K_L C_e}{1 + K_L C_e} \tag{II.8}$$

where K_L is the Langmuir equilibrium constant (L/mg), and q_m is the maximum monolayer adsorption capacity (mg/g).

The linearized form of the Langmuir isotherm is:

$$\frac{C_e}{q_e} = \frac{1}{q_m K_L} + \frac{C_e}{q_m} \tag{II.9}$$

Separation Factor (R_L) The separation factor R_L is a dimensionless constant that expresses the essential characteristics of the Langmuir isotherm and is defined as [193]:

$$R_L = \frac{1}{1 + K_L C_0} \tag{II.10}$$

The interpretation of R_L values is as follows [194]:

- $R_L = 0$: irreversible isotherm
- $0 < R_L < 1$: favorable

- $R_L = 1$: linear
- $R_L > 1$: unfavorable

II.6.3 Thermodynamics of Adsorption

According to thermodynamic theory, energy cannot be created or destroyed in an isolated system. During adsorption, a heat reactioneither exothermic or endothermicoccurs as the solute moves from the solution to the solid-liquid interface [195]. The system's equilibrium can be characterized by thermodynamic parameters such as entropy change (ΔS°), enthalpy change (ΔH°), and Gibbs free energy change (ΔG°). These parameters can be calculated using the Van't Hoff equation [196]:

$$\ln K_d = \frac{\Delta S^\circ}{R} - \frac{\Delta H^\circ}{RT} \tag{II.11}$$

where K_d is the thermodynamic distribution constant. The equilibrium constant can also be expressed as:

$$K_c = \frac{q_e}{C_e} \tag{II.12}$$

where q_e is the amount adsorbed at equilibrium (mg/g) and C_e is the equilibrium concentration of the metal ion in solution (mg/L).

Positive ΔH° values greater than 40 kJ/mol indicate that active sites strongly coordinate metal ions during chemisorption [197]. Negative ΔG° values at varying temperatures suggest that adsorption occurs favorably and spontaneously [198]. The entropy change, ΔS°, provides information about the degree of disorder at the adsorbent surface [199].

Gibbs free energy can be calculated as follows:

$$\Delta G^\circ = -RT \ln K_d \tag{II.13}$$

$$\Delta G^\circ = \Delta H^\circ - T\Delta S^\circ \tag{II.14}$$

Chapter III

Materials and Methods

Chapter III

Materials and Methods

III.1 Introduction

This chapter presents simple protocols for the green synthesis of NiO, MnO_2/Mn_2O_3, and Mn_3O_4 nanoparticles using extracts from Helianthus annuus seed husk shells (sunflower seeds). Additionally, the structural, optical, and morphological properties of the metal oxide nanoparticles were analyzed and confirmed using standard techniques such as energy dispersive X-ray analysis (EDX), scanning electron microscopy (SEM), X-ray diffraction (XRD), UV-Visible spectroscopy, Fourier transform infrared spectroscopy (FTIR), and BET surface area analysis.

III.2 Materials and Methods

III.2.1 Plant Waste: Sunflower Seed Shells

For green synthesis of NiO, MnO_2, and Mn_3O_4 nanoparticles, Helianthus annuus seed husks were chosen as reducing agents. White sunflower seed husks were purchased from a local market in Ouargla, Algeria (Figure III.1).

III.2.2 Chemical Products Used

All chemicals were stored in an inert environment and protected from direct sunlight. Table III.1 summarizes the chemical reagents used.

Figure III.1: Raw material: Helianthus annuus seed husks.

Table III.1: Chemical products used in this work

Chemical Products	Chemical Formula	Purity (%)	M (g/mol)
Manganese(II) nitrate tetrahydrate	$Mn(NO_3)_2$ů$4H_2O$	98	251.01
Nickel nitrate hexahydrate	$Ni(NO_3)_2$ů$6H_2O$	98	290.79
Cadmium sulfate hydrate	$3CdSO_4$ů$8H_2O$		769.51
Lead nitrate	$Pb(NO_3)_2$	99.5	331.21
Copper nitrate trihydrate	$Cu(NO_3)_2$ů$3H_2O$	99	241.60
Sodium hydroxide	NaOH	97	40
Hydrochloric acid	HCl	37	36.46

III.2.3 Methodology

III.2.3.1.Preparation of Extract

Sunflower seed shells were washed repeatedly with tap water and distilled water, dried at 60°C overnight, and ground into powder. For the extract, 9.2 g of powder was added to 100 mL double-distilled water, heated and stirred for 30 min at 70°C, then filtered through Whatman filter paper No. 2. The brown extract was stored at 4°C.

III.1.3.2.Green Synthesis of Nickel Oxide Nanoparticles (NiO-NPs)

20 mL of extract was added to 2 g $Ni(NO_3)_2$ in 100 mL double-distilled water. The mixture was heated at 80°C under constant stirring. NaOH (1M) was gradually added to adjust pH to 12. The reaction proceeded for 2 h, changing color from dark green to pistachio green. The precipitate was filtered, washed, dried at 100°C overnight, and calcined at 400°C for 2 h (Figure III.2).

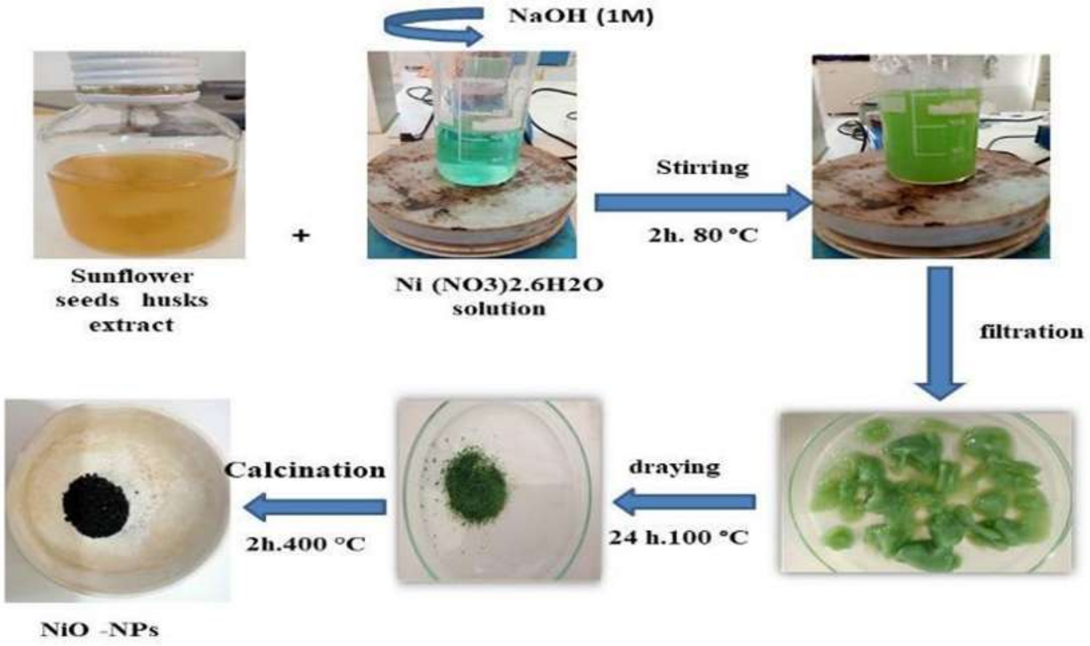

Figure III.2: Schematic of green synthesis of NiO nanoparticles.

III.1.3.3. Green Synthesis of MnO_2/Mn_2O_3 Nanoparticles

10 mL of extract was added to 50 mL solution containing 2 g $Mn(NO_3)_2$ů$4H_2O$, heated at 70°C under stirring (400 rpm) for 3.5 h. A black gel formed, transferred to a ceramic crucible, and calcined at 400°C for 2 h to obtain a black powder (Figure III.3).

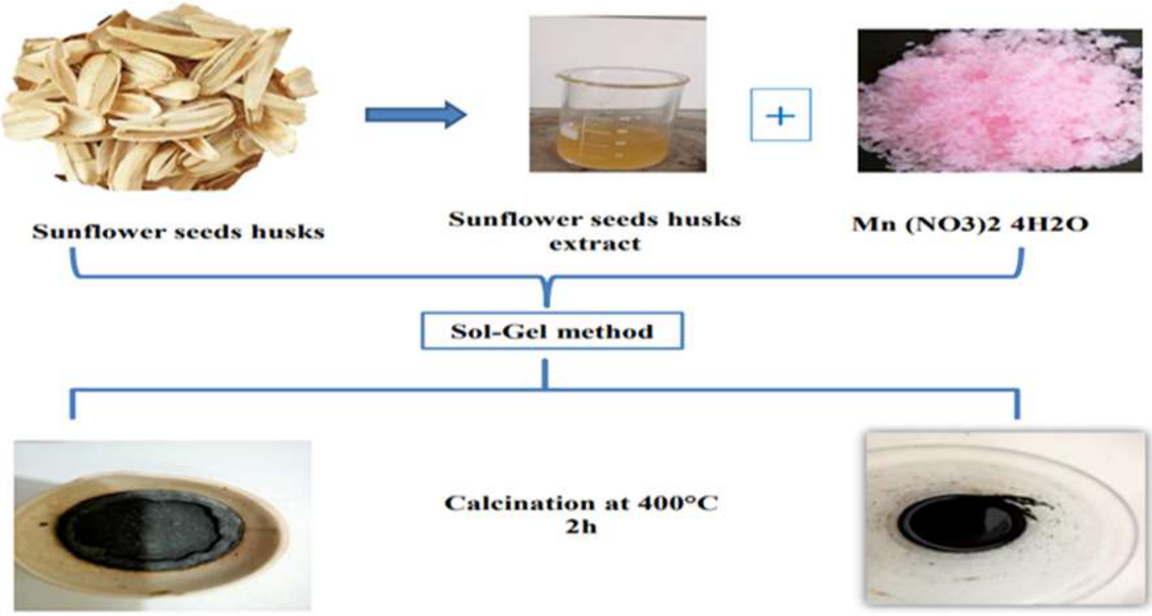

Figure III.3: Schematic of green synthesis of MnO_2/Mn_2O_3 nanoparticles.

III.1.3.4.Green Synthesis of Mn_3O_4 Nanoparticles

1.88 g $Mn(NO_3)_2$ was dissolved in 100 mL double-distilled water, heated for 10 min with stirring. 20 mL extract was added and stirred under same conditions. pH adjusted to 8 with NaOH (1M). Reaction lasted 2 h, color changed from pale yellow to dark brown. Precipitate was filtered, washed, dried at 100°C for 3 h, and calcined at 400°C for 2 h (Figure III.4).

Figure III.4: Schematic of green synthesis of Mn_3O_4 nanoparticles.

III.3 Methods of Characterisation

III.3.1 Structural and Morphological Properties

X-ray Diffraction (XRD)

The crystallographic information of the synthesised nanoparticles was obtained from powder XRD data acquired using a Proto diffractometer (University of El Oued). The X-ray source was Cu Kα radiation ($\lambda = 1.5406$ Å). Reflections were recorded at room temperature, with the 2θ angle scanned between 10° and 80°.

Determination of Nanoparticle Size The size of the crystals was determined using the Debye-Scherrer equation [200]:

$$D = \frac{K\lambda}{\beta \cos\theta} \tag{III.1}$$

where: D = crystallite size (nm), K = Scherrers constant (typically 0.9), λ = X-ray wavelength (Å), θ = Bragg diffraction angle, β = full width at half maximum (FWHM) in radians.

The obtained XRD data were further analysed for crystalline structure by comparison with the Joint Committee on Powder Diffraction Standards (JCPDS) library.

Scanning Electron Microscopy (SEM)

SEM is an analytical technique that uses an electron beam to scan a sample at high magnifications, producing high-resolution images for surface morphology examination. The morphology of the nanoparticle samples was analysed using a ZEISS EVA 15 scanning electron microscope (CRAPC-Ouargla), which provided information on particle size, shape, and surface characteristics.

Elemental composition was determined via energy-dispersive X-ray spectroscopy (EDX) using the same instrument. The ZEISS EVO 15 system features up to four single photodetectors with resolutions up to 24000 Œ 32000 pixels, a SmartSEM control panel with SE C2DX and Everhart-Thornley detectors, a color navigation camera for precise sample positioning, and an infrared camera [201].

BET Surface Area Analysis

The specific surface area of the synthesised nanoparticles was measured using the BET apparatus (CRAPC-Laghouat). The method involves adsorbing nitrogen gas molecules onto the surface of the solid sample at 196°C. The volume of adsorbed gas is then used to calculate the materials specific surface area.

BET analysis also provides information on pore size distribution and surface characteristics of the nanoparticles through statistical evaluation of the nitrogen adsorption isotherm.

III.3.2 Optical Properties

UV-Visible Absorption Spectroscopy

UV-Vis spectroscopy is one of the simplest and most effective techniques for confirming the formation of metal nanoparticles. The UV-Vis spectra of the synthesized nanoparticles were recorded using a Cary 100 Agilent spectrophotometer (CRAPC-Ouargla) in the wavelength range of 250800 nm. A quartz cuvette with a path length of 1 cm was used, and distilled water served as the reference for all measurements.

In UV-Vis spectroscopy, the sample is exposed to light within the UV-Vis range (typically 190900 nm). The wavelengths of absorbed light correspond to electronic transitions between energy levels in the material. The resulting absorption spectrum provides information about the compounds electronic structure, concentration, and sometimes its chemical environment.

Determination of Optical Band Gap (E_g) The optical band gap (E_g) of the nanoparticles can be estimated using the Tauc relation [202]:

$$(\alpha h\nu)^n = A(h\nu - E_g) \tag{III.2}$$

where: n = constant dependent on the type of electronic transition (1/2 for direct allowed, 2 for indirect allowed), α = absorption coefficient, A = proportionality constant, $h\nu$ = photon energy, E_g = optical band gap.

The Tauc plot involves extrapolating the linear portion of $(\alpha h\nu)^n$ versus $h\nu$ to intercept the energy axis, giving the estimated E_g value.

Fourier Transform Infrared Spectroscopy (FTIR)

FTIR spectroscopy (Cary 8000 Agilent, CRAPC-Ouargla) was used to identify the functional groups present in the nanoparticles in the range 4004000 cm^{-1}. This technique provides insights into chemical bonds and molecular interactions that contribute to nanoparticle formation and stabilization.

FTIR works by measuring the absorption of infrared light by the sample. Different functional groups absorb at characteristic vibration frequencies, producing peaks in the spectrum. These peaks reveal the presence of chemical bonds and provide information about surface capping agents and stabilizing molecules on the nanoparticle surface.

III.4 Adsorption Study of Pb(II), Cd(II), and Cu(II) Ions on Synthesized Nanoparticles (III.3)

Adsorption experiments were conducted at room temperature (25 ś 1°C) using Pb, Cd, and Cu ions as adsorbates and NiO, MnO_2/Mn_2O_3, and Mn_3O_4 nanoparticles as adsorbents. Stock solutions of each metal ion were prepared by dissolving appropriate amounts of copper(II) nitrate trihydrate ($Cu(NO_3)_2$ů$3H_2O$), lead nitrate ($Pb(NO_3)_2$), and cadmium sulfate hydrate ($3CdSO_4$ů$8H_2O$) in deionized water.

Batch adsorption experiments were performed by varying parameters such as pH (28), initial metal ion concentration (525 mg L^{-1}), contact time (1060 min), adsorbent dosage (10100 mg), and temperature (2555°C). Each experiment used 25 mL of solution with a defined concentration of metal ions.

Metal ion concentrations in the filtrates were measured using an atomic absorption spectrophotometer (Analytic Jena Contra A 800, Germany). The adsorption capacity (q_e, mg g^{-1}) and adsorption efficiency ($R\%$) were calculated using Equations (II.4) and (II.5), respectively. Adsorption isotherms were also determined (Figure III.5).

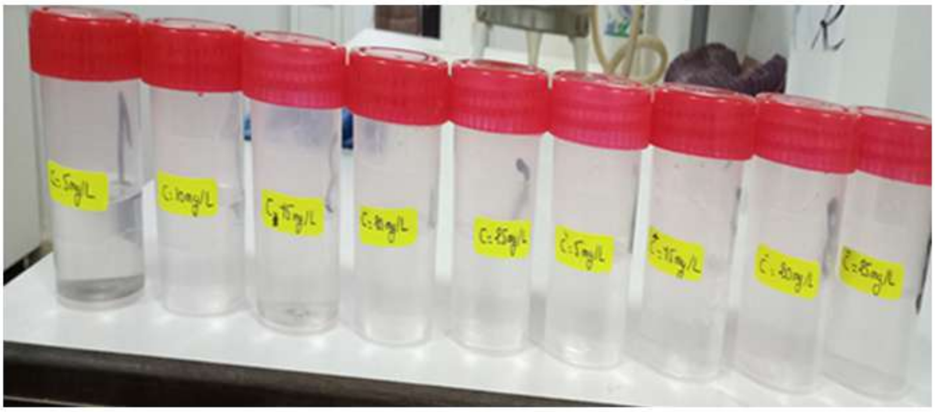

Figure III.5: Adsorption study of Pb(II), Cd(II), and Cu(II) ions on synthesized nanoparticles.

III.5 Study of the Factors Affecting Adsorption

The adsorption efficiency of heavy metal ions (Cu(II), Pb(II), and Cd(II)) onto $NiOMnO_2/Mn_2O_3Mn_3O_4$ nanoparticles is influenced by several operational parameters. In this study, the effects of adsorbent dosage, contact time, pH, initial ion concentration, and temperature were systematically investigated [203, 204].

III.5.1 Effect of Adsorbent Dosage

The adsorbent dosage determines the number of active sites available for adsorption [205, 206]. Experiments were performed using 25 mL of metal ion solution (20 mg L^{-1}) with varying adsorbent amounts from 10 to 100 mg, at pH 7, room temperature (25 °C), and a contact time of 30 minutes. Increasing the adsorbent dose generally improves removal efficiency due to the higher availability of adsorption sites until equilibrium is reached [207].

III.5.2 Effect of Contact Time

The kinetics of adsorption were studied by varying the contact time between 10 and 60 minutes, keeping the adsorbent dosage at 20 mg, pH 7, room temperature (25 °C), and shaking at 200 rpm [208, 209]. Rapid adsorption is usually observed at the initial stages due to a high concentration gradient and large number of vacant active sites, followed by a slower approach to equilibrium [210].

III.5.3 Effect of pH

Solution pH affects both the surface charge of the nanoparticles and the speciation of metal ions [211, 212]. In this study, pH was adjusted from 2 to 8 using 0.1 N NaOH or HCl solutions. Experiments were conducted at room temperature (25 °C) with 25 mL of metal ion solution (20 mg L^{-1}) and 20 mg of adsorbent, for 30 minutes. Adsorption efficiency typically increases with pH due to reduced competition with H^+ ions for active sites [213].

III.5.4 Effect of Initial Ion Concentration

The initial concentration of metal ions affects the mass transfer driving force between the aqueous phase and the adsorbent surface [214, 215]. Metal ion concentrations of 5, 10, 15, 20, and 25 mg L^{-1} were tested under optimal conditions. Higher concentrations increase adsorption capacity until the surface sites are saturated [216].

III.5.5 Effect of Temperature

The influence of temperature on adsorption was examined at 25, 35, 45, and 55 °C, with an adsorbent mass of 0.02 g and an initial ion concentration of 20 mg L^{-1}, at pH 7 and a contact time of 30 minutes [217, 218]. Temperature affects ion mobility and adsorption kinetics; adsorption may increase with temperature if the process is endothermic, or decrease if exothermic [219]. Detailed results are presented in Chapter IV.

Chapter IV

Results and Discussion

Chapter IV

Results and Discussion

IV.1 Mechanism of Plant-Mediated Synthesis of Nanoparticles

IV.1.1 NiO nanoparticles

In plant-mediated synthesis, the phytochemicals such as phenols, alkaloids, flavonoids, saponins, tannins, etc., present in plant extracts are responsible for reducing and stabilizing metal ions into the corresponding metal or metal oxide nanoparticles [203, 204]. According to published studies on the biogenesis of NiO nanoparticles, the active components in the plant extract react with nickel salts to either reduce or form complexes with the Ni(II) ions [102].

Research has indicated that phenolic compounds such as cinnamic acid, coumarin, catechol, ferulic acid, chlorogenic acid, caffeic acid, ellagic acid, protocatechuic acid, and salicylic acid are abundant in sunflower hull extracts [131, 205]. A plausible mechanism for the formation of NiO nanoparticles from Ni(II) ions and sunflower seed husk extract (SFSH) involves the chelation of nickel ions by hydroxyl groups from phenolic compounds (e.g., corilagin, catechol, ellagic acid), forming nickelphenolate complexes. These intermediates decompose during calcination, resulting in the formation of NiO nanoparticles. The proposed mechanism for the green synthesis of NiO nanoparticles is illustrated in Figure IV.1.

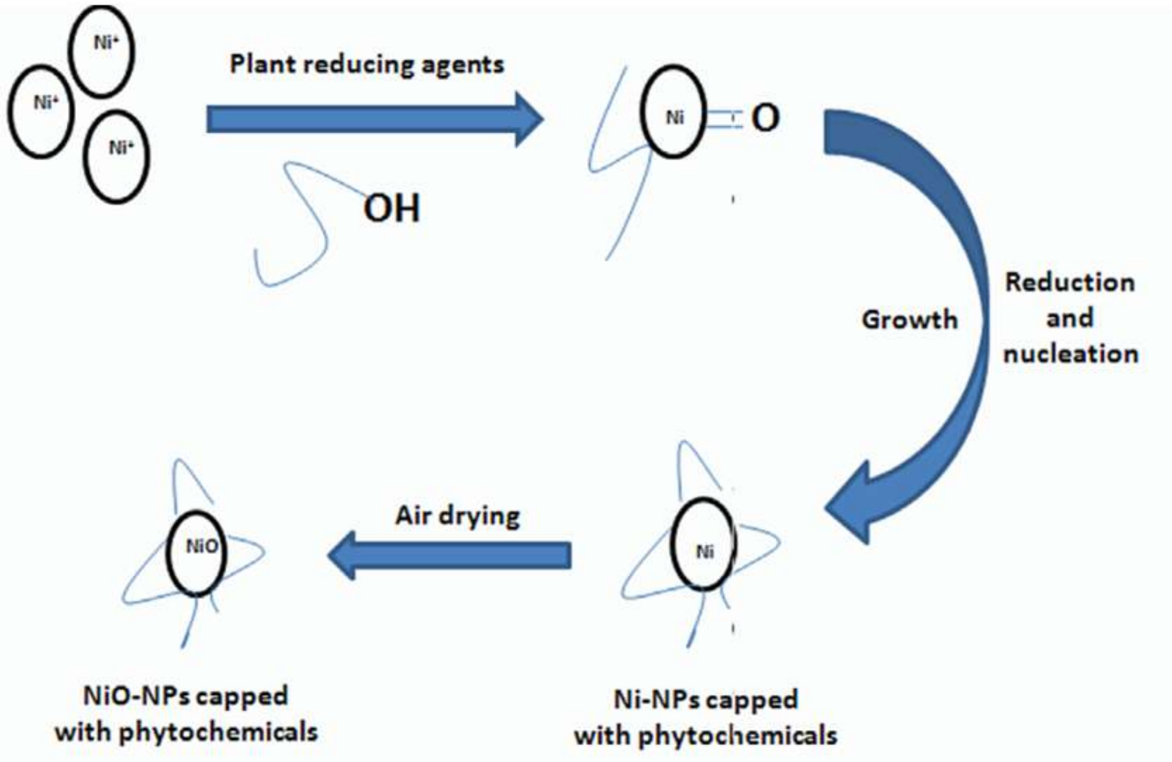

Figure IV.1: Mechanism of green synthesis of NiO nanoparticles.

IV.1.2 MnO_2/Mn_2O_3 Nanoparticles

The physicochemical properties of manganese oxide nanoparticles synthesized via green routes depend strongly on the type and concentration of natural reducing agents present in the plant extract, particularly antioxidants and polyphenolic compounds [206].

In this synthesis, manganese(II) nitrate reacts with the *SFSH* extract, which acts simultaneously as a reducing and stabilizing agent. The reduced manganese atoms subsequently combine with oxygenoriginating either from the atmosphere or from degraded phytochemicalsto form MnO_2 species. These tend to aggregate but are stabilized by organic constituents in the extract. Subsequent calcination at 400°C for 2 hours leads to the formation of mixed-phase MnO_2/Mn_2O_3 nanoparticles with enhanced structural stability and crystallinity.

IV.1.3 Mn_3O_4 (Hausmannite) Nanoparticles

The green synthesis of Mn_3O_4 nanoparticles involves the reduction of Mn^{2+} ions to $Mn(OH)_2$ by phenolic compounds in the plant extract, followed by a sequence of thermal decomposition and oxidation steps [207, 208]. The mechanism can be represented as follows Scheme:

$$\mathrm{Mn^{2+}} + 2\,\mathrm{OH^-} \rightarrow \mathrm{Mn(OH)_2} \tag{IV.1}$$

$$\mathrm{Mn(OH)_2} \rightarrow \mathrm{MnO} + \mathrm{H_2O} \tag{IV.2}$$

$$3\,\mathrm{MnO} + \tfrac{1}{2}\,\mathrm{O_2} \rightarrow \mathrm{Mn_3O_4} \tag{IV.3}$$

This Scheme: (1) The formation of Mn_3O_4 in an alkaline solution proceeds through the reduction of manganese salts to $Mn(OH)_2$. (2) This intermediate then undergoes thermal decomposition to form MnO. (3) Subsequently, the decomposed MnO species is rapidly oxidized in the presence of atmospheric oxygen to yield Mn_3O_4 nanoparticles.

IV.2 Characterization of Nanoparticles

IV.2.1 X-ray Diffraction (XRD)

The XRD pattern of green-synthesized NiO nanoparticles is shown in Figure **??**. The diffraction peaks observed at 2θ values of 37.19ř, 43.70ř, 62.96ř, 75.59ř, and 79.54ř correspond to the Miller indices (hkl) planes (111), (200), (220), (311), and (222), respectively. The peaks indicate a cubic structure with lattice constants $a = b = c = 4.16$ Å, consistent with JCPDS Card No. 01-073-1519 [209, 210]. The sharp peaks and absence of undefined peaks confirm high crystallinity and purity. Using Scherrers formula (Equation III.1), the crystallite size of NiO nanoparticles was calculated as 14.11 nm. The small size is attributed to the phenolic compounds in sunflower hull extract, which act as reducing and capping agents [100, 211].

Figure IV.3 shows the XRD patterns of MnO_2/Mn_2O_3 nanoparticles annealed at 400°C. Two crystalline phases were identified:

- MnO_2 (orthorhombic, JCPDS card No. 00-050-0866): peaks at 2θ = 37.70ř, 41.09ř, 43.18ř, 59.60ř, 65.48ř, 72.86ř corresponding to planes (011), (020), (111), (222), (002), (112).
- Mn_2O_3 (cubic, JCPDS card No. 00-001-1061): peaks at 2θ = 33.39ř, 38.67ř, 45.65ř, 49.72ř, 55.64ř, 57.04ř, 66.19ř corresponding to planes (222), (400), (332), (431), (440), (433), (622), lattice constant $a = b = c = 9.41$ Å.

The crystallite size of MnO_2/Mn_2O_3 nanoparticles was calculated to be 26.93 nm.

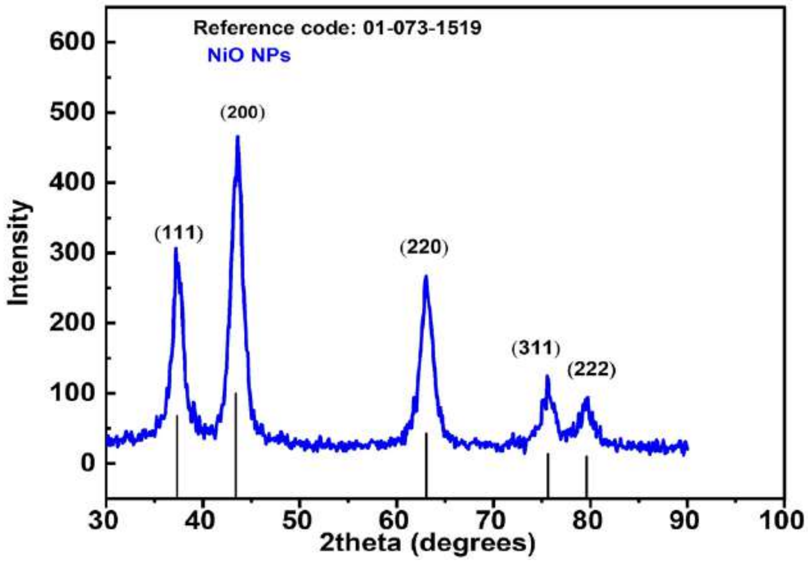

Figure IV.2: XRD pattern of biosynthesized NiO nanoparticles at 400 °C.

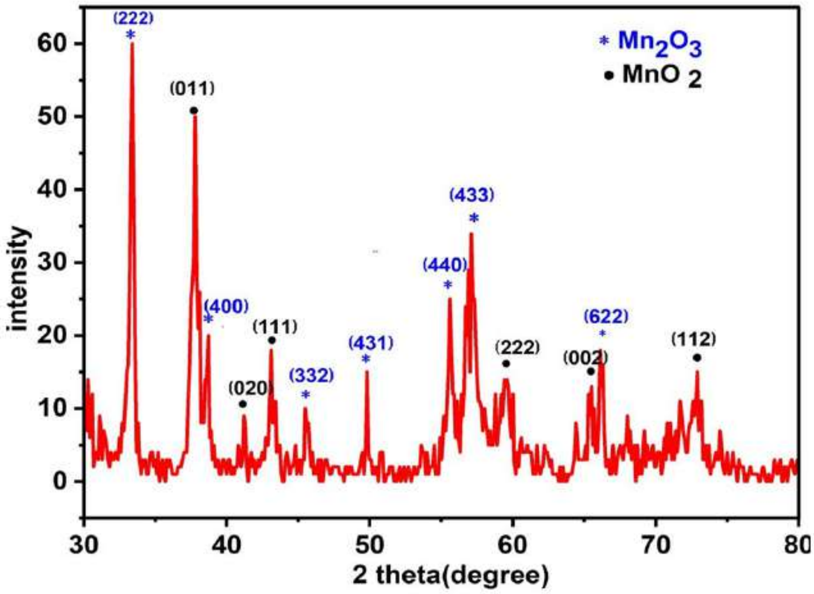

Figure IV.3: XRD pattern of biosynthesized MnO_2/Mn_2O_3 nanoparticles at 400 °C.

The XRD pattern of Mn_3O_4 nanoparticles annealed at 400 °C for 2 h is shown in Figure IV.4. The peaks observed at 2θ = 18.08ř, 29.07ř, 31.02ř, 32.68ř, 36.15ř, 38.35ř, 44.32ř, 51.45ř, 58.72ř, 60.18ř, 64.78ř correspond to planes (101), (112), (200), (103), (211), (004), (220), (105), (321), (224), (314). These peaks match the tetragonal hausmannite phase of Mn_3O_4 (JCPDS Card No. 00-001-1127), space group I41/amd, with lattice constants $a = b = 5.75$ Å and $c = 9.42$ Å [214, 215]. Using the Debye-Scherrer equation, the average particle size was estimated at 20.13 nm, slightly higher than in previous studies [116, 218], confirming the effectiveness of sunflower seed husk extract as a reducing and capping agent.

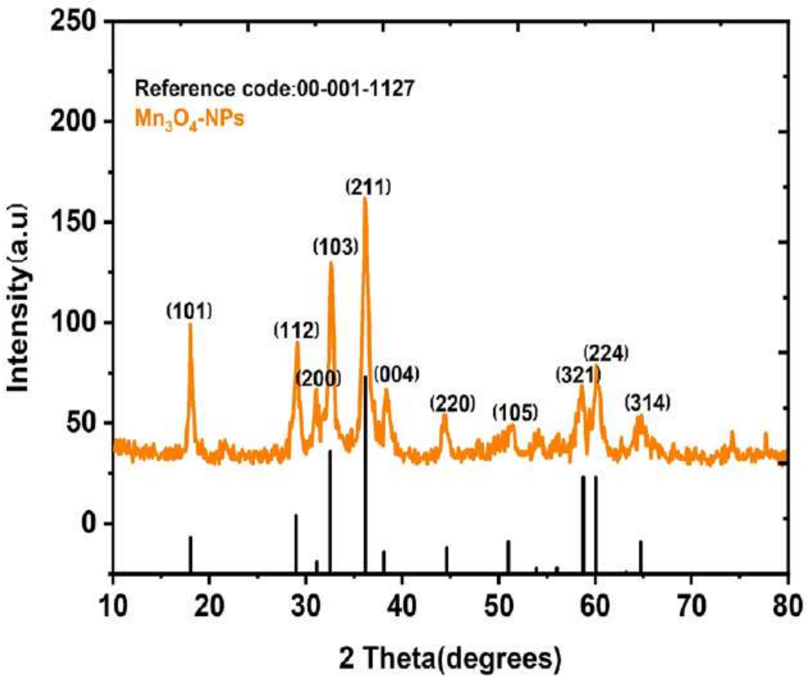

Figure IV.4: XRD pattern of biosynthesized Mn_3O_4 nanoparticles at 400 °C.

IV.2.2. Scanning Electron Microscopy (SEM-EDX)

The SEM images of NiO nanoparticles annealed at 400 °C are shown in Figure IV.5(a) and (b). The images reveal irregular particle morphology with noticeable agglomeration. Particle sizes range from 55 to 127 nm, with an average of 100 nm, as indicated in the histogram in Figure IV.5(c). The observed agglomeration may result from the high surface tension and surface energy of NiO nanoparticles [219], while the non-homogeneous morphology could be due to granule germination stages.

The EDX spectrum of NiO NPs (Figure IV.6(a)) displays three distinct peaks corresponding to nickel and one peak for oxygen, confirming the presence of these elements and the successful synthesis of NiO nanoparticles. The weight percentages were 56.44% Ni and 43.56% O, and the atomic percentages were 73.90% Ni and 26.10% O, in agreement with previous reports [220].

SEM images of green-synthesized MnO_2/Mn_2O_3 nanoparticles are presented in Figures IV.5(d) and (e). The particles exhibit a roughly spherical morphology with some degree of agglomeration. Particle sizes were determined to range from 30 to 100 nm, with an average of 73.4 nm, as calculated using ImageJ software (Figure IV.5(f)). The growth and aggregation of the nanoparticles are attributed to their high surface area and density [221]. EDX analysis (Figure IV.6(b)) shows the presence of Mn and O, with weight percentages of 63.82% and

36.18%, respectively, indicating that the majority of particles are MnO_2 nanoparticles.

Figure IV.5(g) and (h) illustrate the morphology of Mn_3O_4 nanoparticles. SEM analysis indicates that the Mn_3O_4 NPs have a spherical and porous surface structure with notable aggregation. Weak interparticle forces contribute to the formation of aggregates and sub-micron structures, while covalent or metallic linkages can stabilize these aggregates [222]. The average particle size was approximately 87 nm, as shown in Figure IV.5(i).

The EDX spectrum of Mn_3O_4 nanoparticles (Figure IV.6(c)) confirms the elemental composition, showing oxygen (25.63%) and manganese (74.37%) as the main constituents. No additional peaks were observed, indicating that the synthesized Mn_3O_4 (Hausmannite) is of high purity [223].

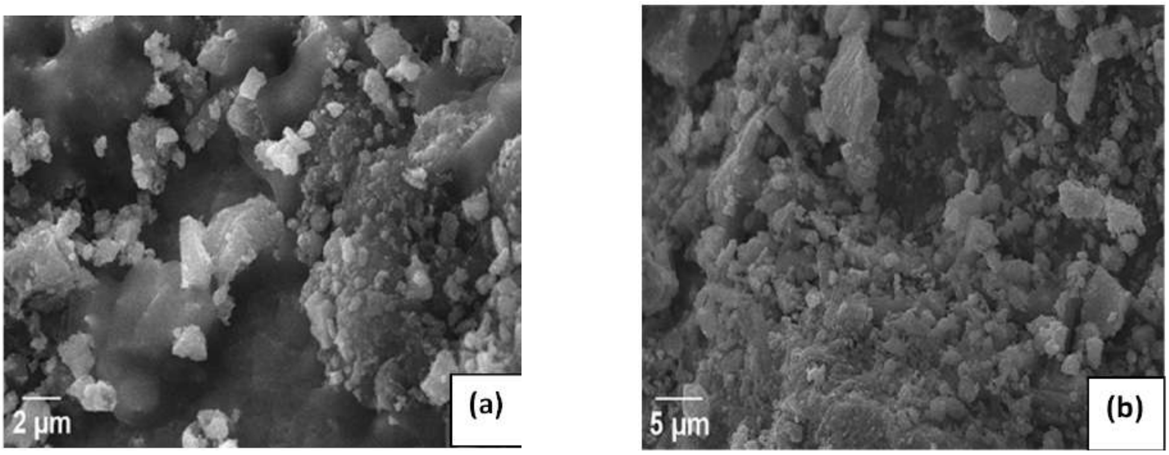

(a) NiO SEM **(b)** NiO SEM zoom / different region

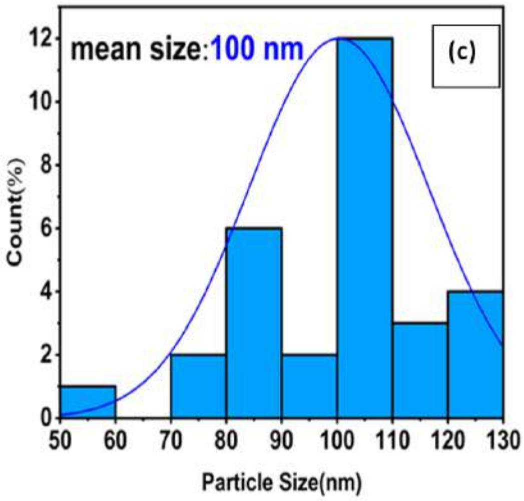

(c) NiO particle size distribution

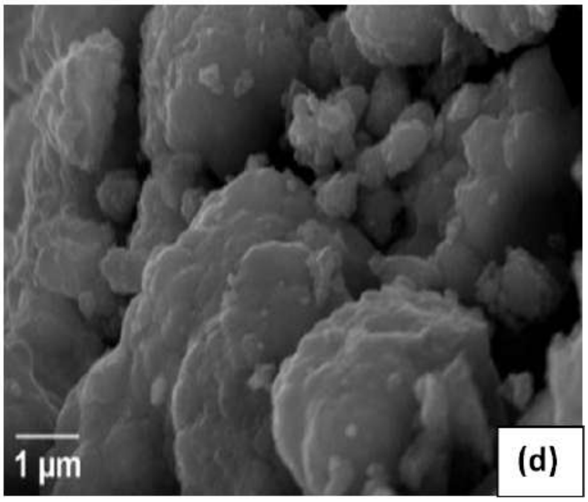

(d) MnO_2/Mn_2O_3 SEM

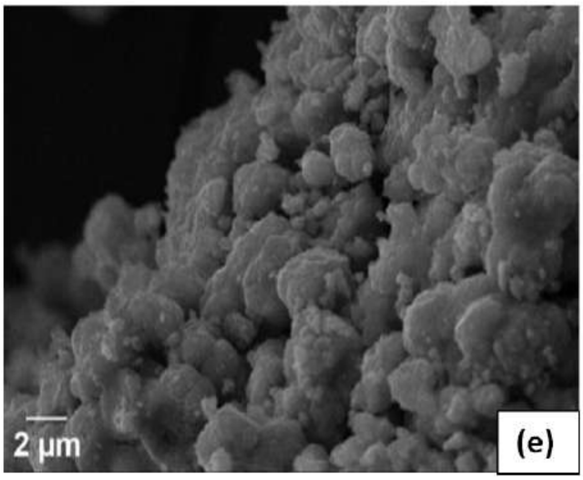

(e) MnO_2/Mn_2O_3 SEM zoom / different region

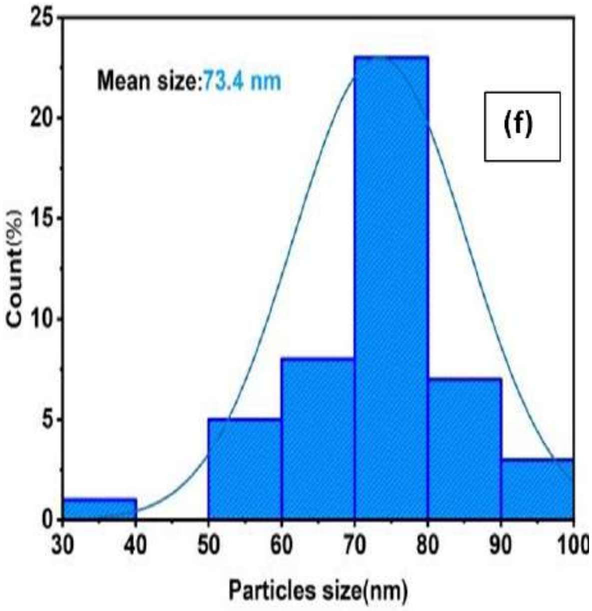

(f) MnO_2/Mn_2O_3 particle size distribution

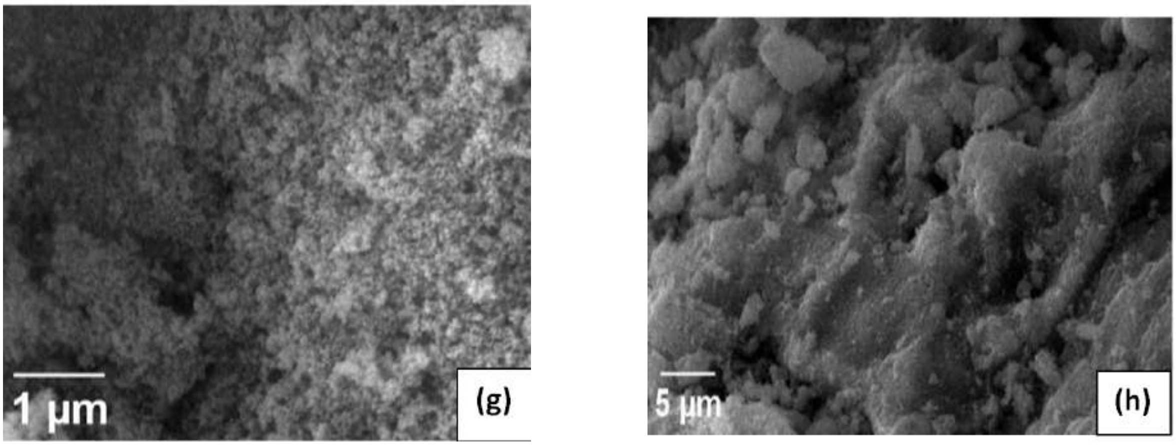

(g) Mn_3O_4 SEM

(h) Mn_3O_4 SEM zoom / different region

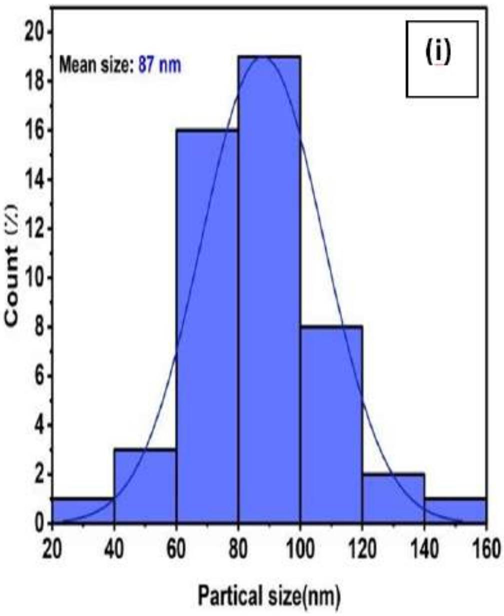

(i) Mn_3O_4 particle size distribution

Figure IV.5: SEM images and particle size distributions of the synthesized nanoparticles: (a,b) NiO SEM images, (c) NiO particle size distribution; (d,e) MnO_2/Mn_2O_3 SEM images, (f) MnO_2/Mn_2O_3 particle size distribution; (g,h) Mn_3O_4 SEM images, (i) Mn_3O_4 particle size distribution.

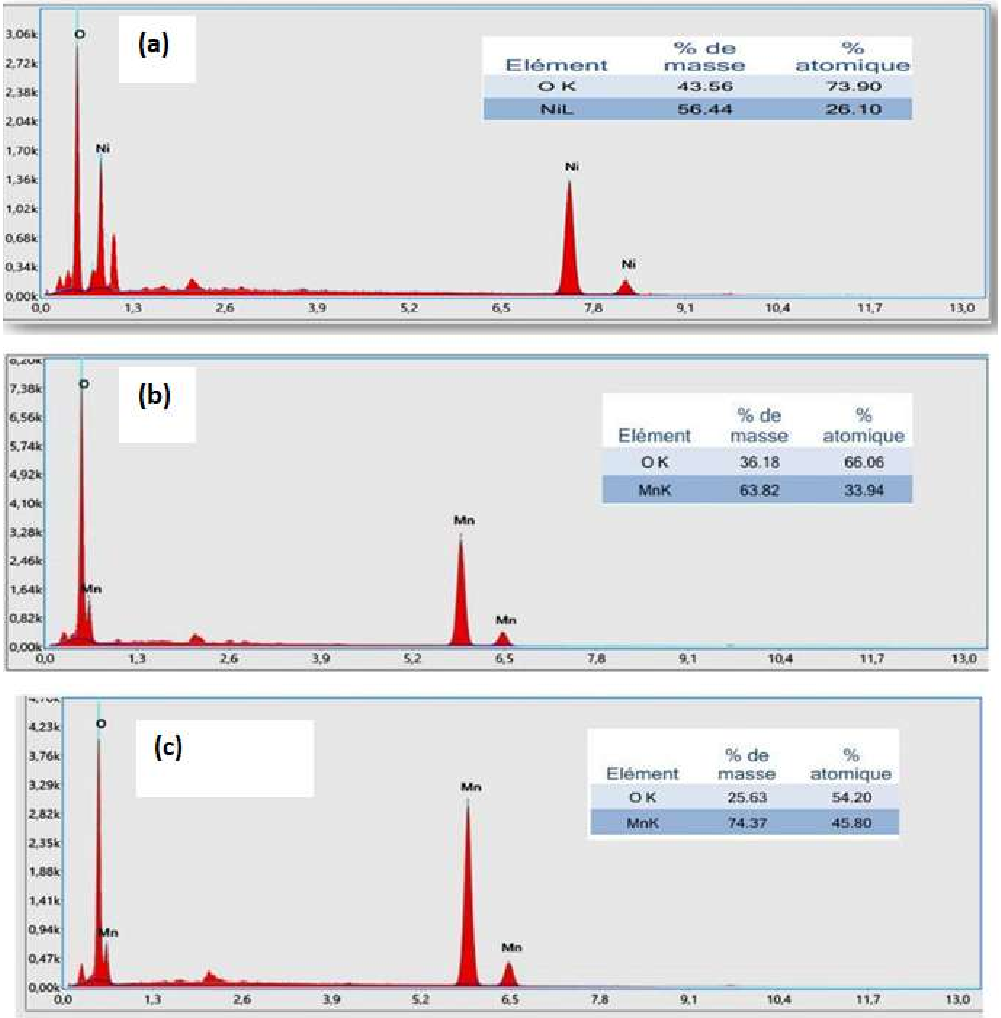

Elément	% de masse	% atomique
O K	43.56	73.90
NiL	56.44	26.10

Elément	% de masse	% atomique
O K	36.18	66.06
MnK	63.82	33.94

Elément	% de masse	% atomique
O K	25.63	54.20
MnK	74.37	45.80

Figure IV.6: EDX spectra of the synthesized nanoparticles: (a) NiO NPs, (b) MnO_2/Mn_2O_3 NPs, and (c) Mn_3O_4 NPs.

IV.2.2 UVVisible Spectroscopy and Band Gap Analysis

The optical properties and band gap energies of the synthesized nanoparticles were investigated using UVVisible spectroscopy.

NiO Nanoparticles Figures IV.7a and IV.7b present the UVVis absorption spectrum and the corresponding Tauc's plot for NiO nanoparticles. A strong absorption peak (λ_{max}) appeared at 298 nm, confirming the successful formation of NiO nanoparticles, consistent with previous reports [224]. This prominent band arises from the electronic transition from the valence band to the conduction band of the NiO semiconductor [225]. The optical band gap energy (E_g) was determined to be 3.60 eV (Figure IV.7b), verifying the semiconducting nature of the NiO nanoparticles [226, 227].

MnO_2/Mn_2O_3 Nanoparticles The UVVis spectrum of MnO_2/Mn_2O_3 nanoparticles was recorded in the 250800 nm range (Figure IV.8a). A broad absorption peak at 293 nm indicates the formation of MnO_2/Mn_2O_3 nanoparticles. The optical band gap energy, calculated using Tauc's method (Figure IV.8b), was 3.70 eV, which is higher than typical direct band gap values reported in the literature [228, 229]. This increase is attributed to the reduced particle size, which enhances electrochemical performance and improves the efficiency of energy conversion devices for environmental remediation [18, 230].

Mn_3O_4 Nanoparticles Figure IV.9a shows the UVVis absorption spectrum of Mn_3O_4 nanoparticles, with an absorption maximum at 296 nm. The Tauc's plot (Figure IV.9b) was used to determine the optical band gap, yielding $E_g = 3.70$ eV. This value is higher compared to similar materials in the literature [231, 232]. The observed increase in band gap is attributed to the quantum confinement effect arising from the small crystallite size of the synthesized Mn_3O_4 nanoparticles [233].

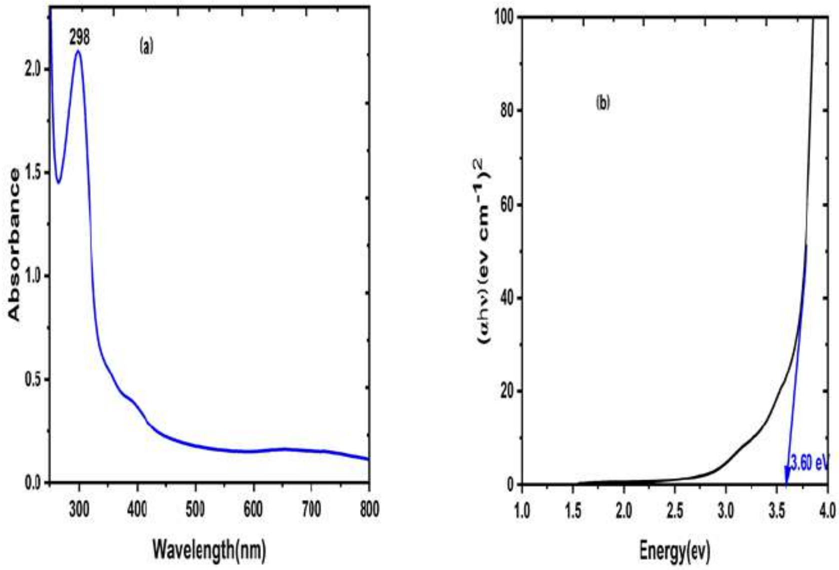

Figure IV.7: (a) UVVisible spectrum of NiO nanoparticles, (b) direct band gap transition determined using Tauc's method.

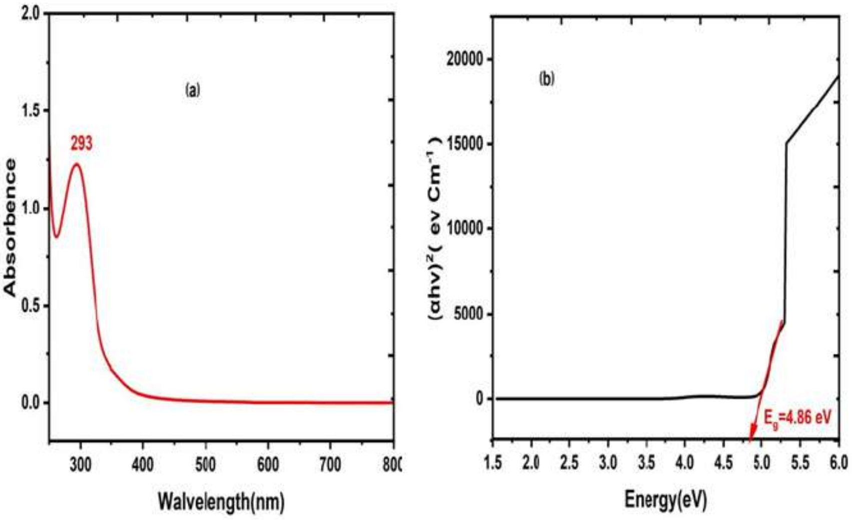

Figure IV.8: (a) UVVisible spectrum of MnO_2/Mn_2O_3 nanoparticles, (b) direct band gap transition using Tauc's method.

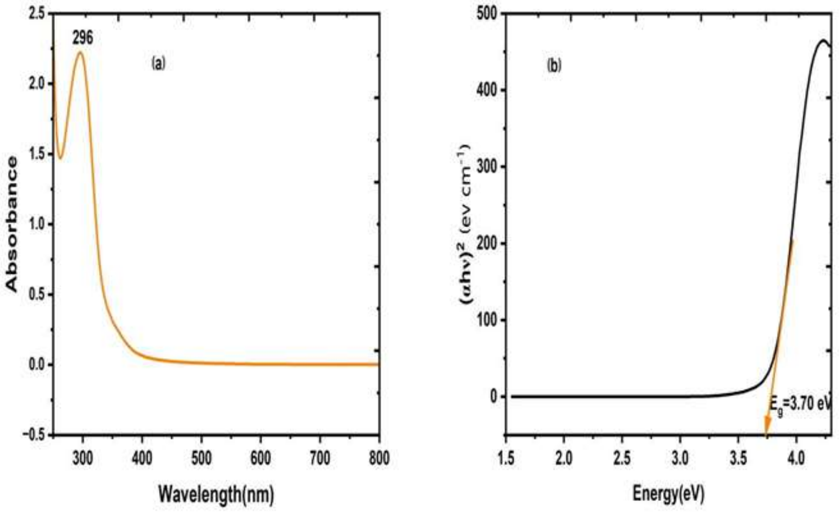

Figure IV.9: (a) UVVisible spectrum of Mn_3O_4 nanoparticles, (b) direct band gap transition using Tauc's method.

IV.2.3 Fourier Transform Infrared Spectroscopy (FTIR)

FTIR analysis was carried out to identify the functional groups present in the synthesized nanoparticles.

NiO Nanoparticles Figure IV.10 displays the FTIR spectrum of NiO nanoparticles annealed at 400 °C. The spectrum shows absorption bands in the range of 4004000 cm^{-1}. A broad band at 3330 cm^{-1} is attributed to O–H stretching vibrations from hydroxyl groups, while the band at 1626 cm^{-1} corresponds to the bending vibrations of water molecules (H–O–H) [234]. The band at 1732 cm^{-1} is assigned to the carbonyl group (C=O), and the intense band at 1345 cm^{-1} corresponds to C–O stretching vibrations. Peaks observed at 660, 827, and 981 cm^{-1} are associated with Ni–O vibrations, with the 1000400 cm^{-1} region characteristic of metal-oxygen stretching [235].

MnO_2/Mn_2O_3 Nanoparticles Figure IV.11 shows the FTIR spectra of MnO_2/Mn_2O_3 nanoparticles. The band around 2102 cm^{-1} is assigned to C–H stretching and bending vibrations [236], while the broad band at 1736 cm^{-1} corresponds to carbonyl groups (C=O). Peaks at 1364 and 1222 cm^{-1} are attributed to CN vibrations and carboxylic groups, respectively [237]. The bands at 454, 551, and 656 cm^{-1} are characteristic of Mn–O and Mn–O–Mn vibrations, confirming the formation of MnO_2/Mn_2O_3 nanoparticles [238].

Mn_3O_4 (Hausmannite) Nanoparticles Figure IV.12 presents the FTIR spectra of Mn_3O_4 nanoparticles calcined at 400 °C for 2 hours. The band at 2337 cm^{-1} is attributed to the CH_2 group, while bands at 1740 and 1366 cm^{-1} correspond to C=O and CN vibrations, respectively. The band at 592 cm^{-1} is associated with Mn–O tetrahedral vibrations, and the peak at 473 cm^{-1} is linked to octahedral Mn sites [239].

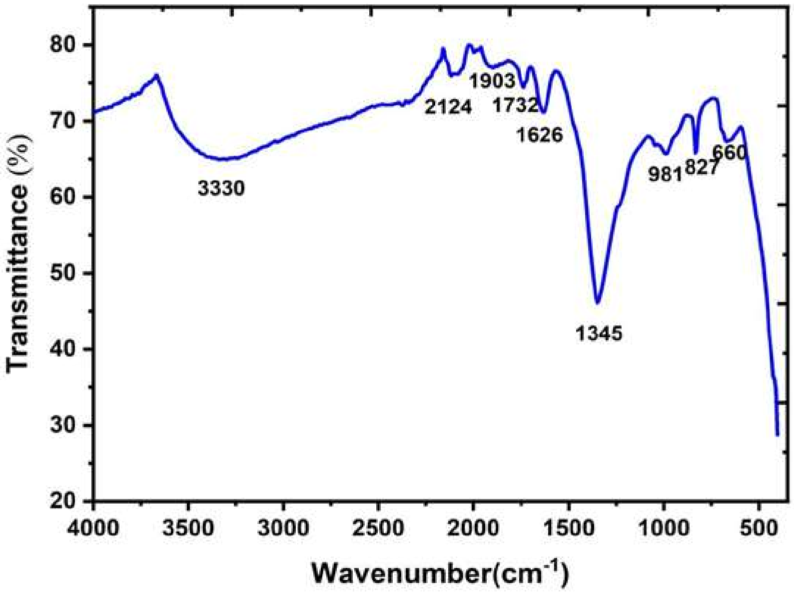

Figure IV.10: FTIR spectra of NiO nanoparticles annealed at 400 °C.

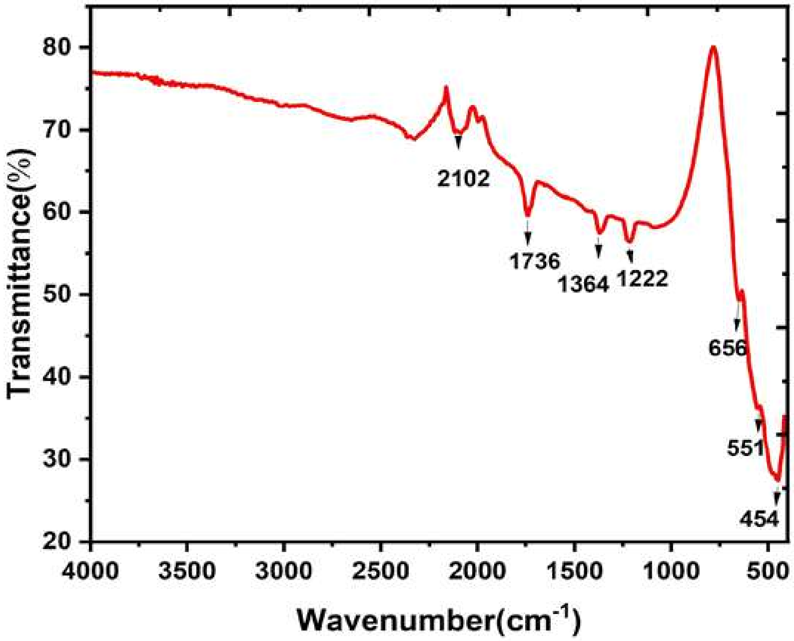

Figure IV.11: FTIR spectra of MnO_2/Mn_2O_3 nanoparticles annealed at 400 °C.

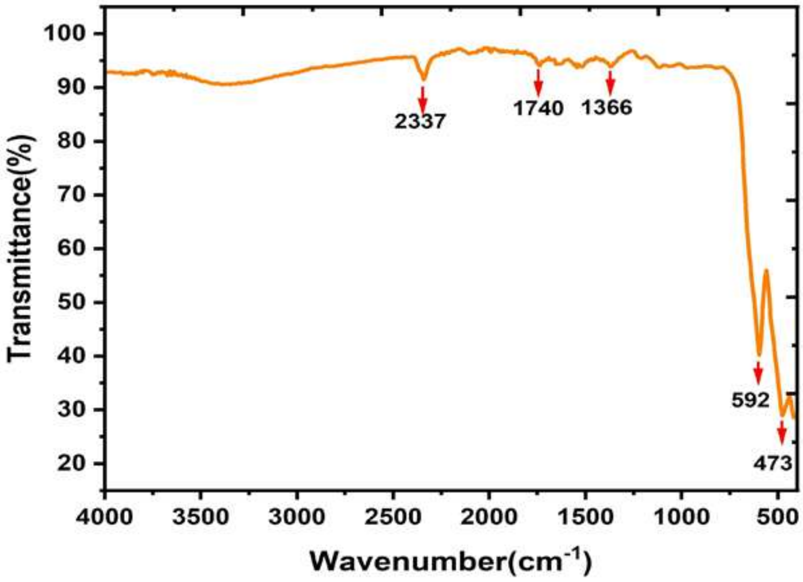

Figure IV.12: FTIR spectra of Mn_3O_4 nanoparticles annealed at 400 °C.

float

IV.2.4 BrunauerEmmettTeller (BET) Surface Area Analysis

The surface area of the synthesized nanoparticles was determined using the BrunauerEmmettTeller (BET) method, which relies on the physical adsorption of a gas on a solid surface to calculate the specific surface area corresponding to a monomolecular adsorbate layer [240].

AdsorptionDesorption Isotherms Figure IV.13 shows the nitrogen adsorptiondesorption isotherms of NiO, MnO_2/Mn_2O_3, and Mn_3O_4 nanoparticles. According to IUPAC classification, all samples exhibit type IV isotherms with H3 hysteresis loops, indicative of capillary condensation where N_2 molecules condense as multilayers filling mesopores. The mesoporous nature and high surface areas of the samples make them suitable for adsorption applications [240].

NiO Nanoparticles The specific surface area of NiO nanoparticles was found to be 29.54 $m^2\ g^{-1}$, with a pore volume of 0.09 $cm^3\ g^{-1}$ and an average pore diameter of 12.12 nm.

MnO_2/Mn_2O_3 Nanoparticles The BET analysis indicated a specific surface area of 62.99 $m^2\ g^{-1}$, a pore size of 16.12 nm, and a pore volume of 0.18 $cm^3\ g^{-1}$ for MnO_2/Mn_2O_3 nanoparticles.

Mn_3O_4 (Hausmannite) Nanoparticles Mn_3O_4 nanoparticles displayed a relatively small surface area of 4.18 $m^2\ g^{-1}$, with mean pore diameter and pore volume of 28 nm and 0.007 $cm^3\ g^{-1}$, respectively, according to BJH analysis. These values confirm that Mn_3O_4 nanoparticles are mesoporous, consistent with previous reports on pure Mn_3O_4 [241].

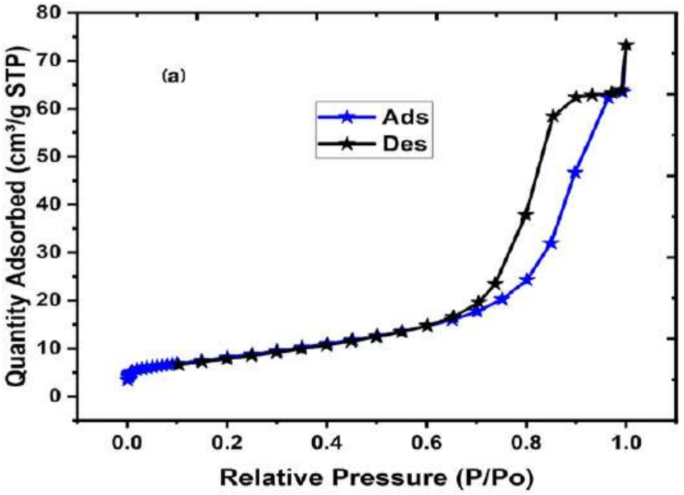

(a) NiO

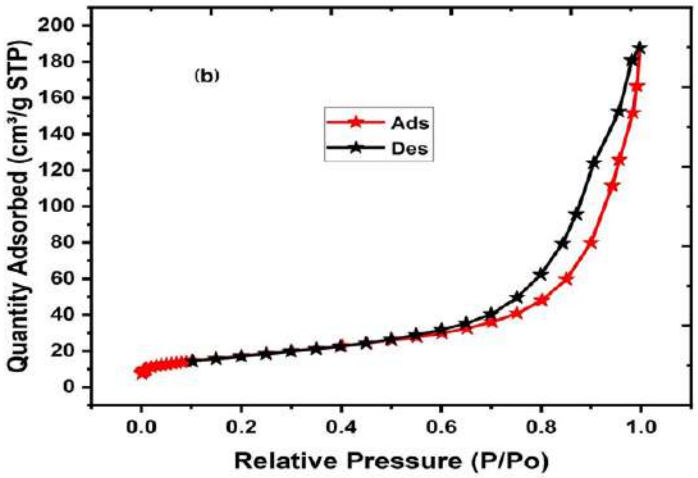

(b) MnO_2/Mn_2O_3

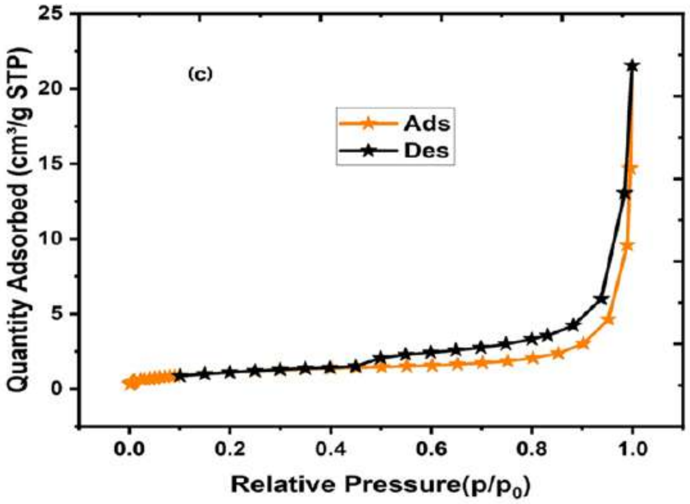

(c) Mn_3O_4

Figure IV.13: Nitrogen adsorptiondesorption isotherms of the synthesized nanoparticles.

IV.3 Adsorption Study of Cd^{2+}, Pb^{2+}, and Cu^{2+} Ions on NiO, MnO_2/Mn_2O_3, and Mn_3O_4 NPs

IV.3.1 Factors Influencing Adsorption Process

IV.3.1.1. Effect of pH

pH is another significant factor affecting the ability of an adsorbent to remove heavy metal ions. The effect of pH on the elimination efficiency of Cd^{2+}, Pb^{2+}, and Cu^{2+} was investigated by adjusting the pH from 2 to 8 while keeping all other parameters constant (initial metal ion concentration: 20 $\mathrm{mg\,L^{-1}}$, contact time: 30 min, shaking speed: 200 rpm, adsorbent dose: 20 mg, and room temperature).

As shown in Figure IV.3.1(a), for all metal ions, the removal efficiency of NiO nanoparticles increased at basic pH compared to acidic pH. At alkaline conditions (pH 8), the elimination percentages of Pb(II), Cd(II), and Cu(II) were 97.52%, 99.73%, and 99.94%, respectively, while at acidic pH (pH 2), the removal efficiencies were 62.5%, 65.05%, and 99.90%, respectively.

The sorption capacities of MnO_2/Mn_2O_3 nanoparticles for Pb(II), Cd(II), and Cu(II) at different pH values are presented in Figure IV.15(a). According to the results, sorption capacity increases with rising pH. Under alkaline conditions (pH 8), the elimination of Pb(II), Cu(II), and Cd(II) reached 97.51%, 99.90%, and 99.71%, respectively. At acidic conditions, Pb(II) removal was 42% at pH 5, while Cu(II) and Cd(II) removal at pH 2 were 62.42% and 99.51%, respectively.

Furthermore, Figure IV.16(a) illustrates the removal performance of Mn_3O_4 nanoparticles toward Pb(II), Cd(II), and Cu(II). The results showed that the removal efficiency significantly increased with increasing pH. At pH 2, the elimination of Pb(II), Cu(II), and Cd(II) was 20.85%, 12.8%, and 31.65%, respectively. However, at pH 8, the efficiencies increased to 99.78%, 99.86%, and 78.5%, respectively.

The reduced adsorption of metal ions at low pH values may be attributed to the high concentration of hydrogen ions, which compete with M^{2+} ions for the active sorption or ion-exchange sites, thereby decreasing the number of available binding sites [242]. Conversely, as the pH increases, the surface of the adsorbent becomes more negatively charged and more hydroxyl (OH) groups are formed, enhancing the adsorption of metal ions [243].

IV.3.1.2. Effect of Adsorbent Dosage

The effect of adsorbent dosage on the removal efficiency of metal ions was evaluated by varying the amount of adsorbent from 10 mg to 100 mg under fixed conditions (contact time: 30 min, shaking speed: 200 rpm, room temperature, pH 7, and initial metal ion concentration of 20 $\mathrm{mg\,L^{-1}}$).

Nickel oxide nanoparticles exhibited optimal elimination capacities of 92.50% and 99.91% for Pb(II) and Cu(II), respectively. These results indicate that increasing the adsorbent dosage enhances the metal removal efficiency, with optimal dosages of 20 mg for Pb(II) and 40 mg for Cu(II), as shown in Figure IV.3.1(b). Additionally, the removal efficiency of Cd(II) increased with the increase in dosage, reaching a maximum efficiency of 99.70%. This behavior can be attributed to the increased number of accessible adsorption sites on the NiO nanoparticle surface.

Pb(II) and Cu(II) removal efficiencies also increased significantly, most likely due to the greater availability of adsorption sites on NiO-NPs [244]. However, after reaching the optimal dosage, the efficiency began to decline with further dosage increases. This decline may be attributed to particle overcrowding, resulting in the overlap or aggregation of adsorption sites. Excessively high adsorbent dosage can reduce the effective surface area available for metal binding, leading to decreased adsorption efficiency, particularly when large quantities of NiO-NPs were dispersed in synthetic wastewater [245].

As shown in Figures IV.15(c) and IV.16(c), increasing the dosage of MnO_2/Mn_2O_3 and Mn_3O_4 nanoparticles from 10 mg to 20 mg resulted in a noticeable improvement in Pb(II) and Cd(II) removal efficiencies. MnO_2/Mn_2O_3 NPs achieved 79.83% (Pb) and 99.56% (Cd), while Mn_3O_4 NPs achieved 72% removal for Cd(II). Moreover, increasing the dosage from 10 mg to 100 mg significantly enhanced Cu(II) removal from 97.48% to 99.86% using MnO_2/Mn_2O_3 NPs. For Mn_3O_4 NPs, the removal efficiencies of Pb^{2+} and Cu^{2+} increased from 23.25% and 28.5% at 10 mg to 98.65% and 84.57% at 100 mg, respectively.

In general, metal ion removal efficiency increases with increasing adsorbent dosage due to the greater availability of surface area and binding sites. However, beyond a certain dosage, the efficiency may decrease [246, 247]. When the nanoparticle dosage becomes too high, adsorption may decline due to site overlap, particle aggregation, or distribution of identical cations over a much larger surface area. During the early stages, when heavy metal concentration is relatively high, increasing nanosorbent dosage accelerates the adsorption process until saturation is reached. Once equilibrium is established, excess adsorption sites remain unused because the remaining metal ions in solution are insufficient to occupy them [248].

IV.3.1.3. Effect of Contact Time

Contact time plays a crucial role in metal ion sorption, as it influences the extent to which active sites on the adsorbent surface are occupied. The effect of contact time on the removal efficiency of the studied metal ions was examined over a period of 10–60 minutes under fixed conditions (room temperature, shaking speed of 200 rpm, adsorbent dosage of 20 mg, pH 7, and initial ion concentration of 20 $\mathrm{mg\,L^{-1}}$).

According to the results presented in Figure IV.3.1(c), Pb(II) adsorption onto NiO nanoparticles reached a maximum removal efficiency of 74.73% within the first 10 minutes, after which the rate began to decline. This behavior can be attributed to the diffusion of M^{2+} ions from the outer surface into the micropores as active sites become progressively occupied, which reduces the adsorption rate [249]. The slight decrease after ten minutes may also be due to repulsive interactions between the adsorbed metal ions and those still in solution [250]. Cd(II) and Cu(II) showed effective removal efficiencies of 93.97% and 99.96%, respectively, after 30 minutes. This rapid increase in the early stages is likely due to the abundance of available active sites on the nanoadsorbent surface, whereas the slower increase at later stages results from the gradual depletion of these active sites over time [251, 252].

Figure IV.15(d) illustrates the effect of contact time on the removal of Pb(II), Cd(II), and Cu(II) using MnO_2/Mn_2O_3 nanoparticles. Pb(II) exhibited a removal efficiency of 77.95% after 50 minutes, while Cu(II) and Cd(II) achieved efficiencies of 99.69% and 99.62%, respectively, after 60 minutes. The adsorption of Pb(II) was initially rapid before slowing after 10 minutes, likely due to the diffusion of M^{2+} ions from the outermost surface into internal pores as active sites became increasingly occupied [253]. For Cu(II), the removal efficiency improved with longer contact times, consistent with extended interaction between metal ions and available adsorption sites. As observed previously, adsorption was rapid initially due to the abundance of vacant sites, followed by a slower approach to equilibrium as available sites decreased [251, 252].

For Mn_3O_4 nanoparticles, the maximum adsorption efficiencies were 98.09% for Pb(II), 73.33% for Cd(II), and 24.55% for Cu(II), as shown in Figure IV.16(d). These results demonstrate that metal ion removal efficiency increases with time, consistent with the progressive occupation of available active sites on the adsorbent surface.

IV.3.1.4. Effect of Initial Metal Ion Concentration

Under optimal experimental conditions, the adsorption of the selected heavy metals from artificially contaminated water was investigated by varying the initial metal ion concentrations (5, 10, 15, 20, and 25 $\mathrm{mg\,L^{-1}}$).

As shown in Figure IV.3.1 (d), adsorption of metal ions onto nickel oxide nanoparticles decreases with increasing initial metal concentration. The removal efficiencies of Pb(II), Cd(II), and Cu(II) decreased from 92.30%, 99.83%, and 99.88% at lower concentrations to 77.45%, 99.64%, and 99.74%, respectively, at higher concentrations.

Figure IV.15(d) presents the adsorption of Pb(II), Cu(II), and Cd(II) onto MnO_2/Mn_2O_3 nanoparticles. Similar to the trend observed for NiO-NPs, the removal efficiencies declined as the initial concentration increased. At the lowest concentration, the highest removal efficiencies recorded for Pb(II), Cu(II), and Cd(II) were 94.03%, 99.95%, and 99.82%, respectively.

According to Figure IV.16(d), Mn_3O_4 nanoparticles exhibited high adsorption efficiencies at low initial concentrations of Pb^{2+}, Cd^{2+}, and Cu^{2+}, achieving 99.22%, 89.43%, and 99%, respectively.

These observations confirm a strong inverse correlation between adsorption efficiency and initial metal ion concentration. At low concentrations, a higher proportion of metal ions can be adsorbed due to the abundance of available active sites on the nanosorbent surface. In contrast, at higher concentrations, the number of active adsorption sites becomes insufficient relative to the number of metal ions present, resulting in decreased removal efficiencies [254].

IV.3.1.5. Effect of Temperature

The influence of temperature on the adsorption of lead, cadmium, and copper ions was examined over a wide temperature range (298, 308, 318, and 328 K).

Figures IV.3.1(e) and IV.15(e) show that increasing the temperature from 298 to 328 K enhanced the adsorption of metal ions onto NiO and MnO_2/Mn_2O_3 nanoadsorbents. This increase may be attributed to the higher kinetic energy of the system at elevated temperatures, which improves the mobility and diffusion rate of metal ions toward the adsorbent surface.

Furthermore, the interaction between metal ions and the active sites on these nanomaterials appears to be endothermic in nature, suggesting that the adsorption process may involve chemisorption [255].

In contrast, Figure IV.16(e) shows that for Mn_3O_4 nanoparticles, the removal efficiency of Pb(II), Cd(II), and Cu(II) decreased as the temperature increased from 298 to 328 K. Specifically, the removal percentages decreased from 98.17% to 89% for Pb(II), from 98.2% to 89% for Cd(II), and from 73% to 66.19% for Cu(II). This decline indicates that higher temperatures weaken the interactions between the metal ions and active adsorption sites on the Mn_3O_4 surface. Thus, the adsorption process in this case appears to be exothermic, resulting in reduced biosorption at elevated temperatures [256].

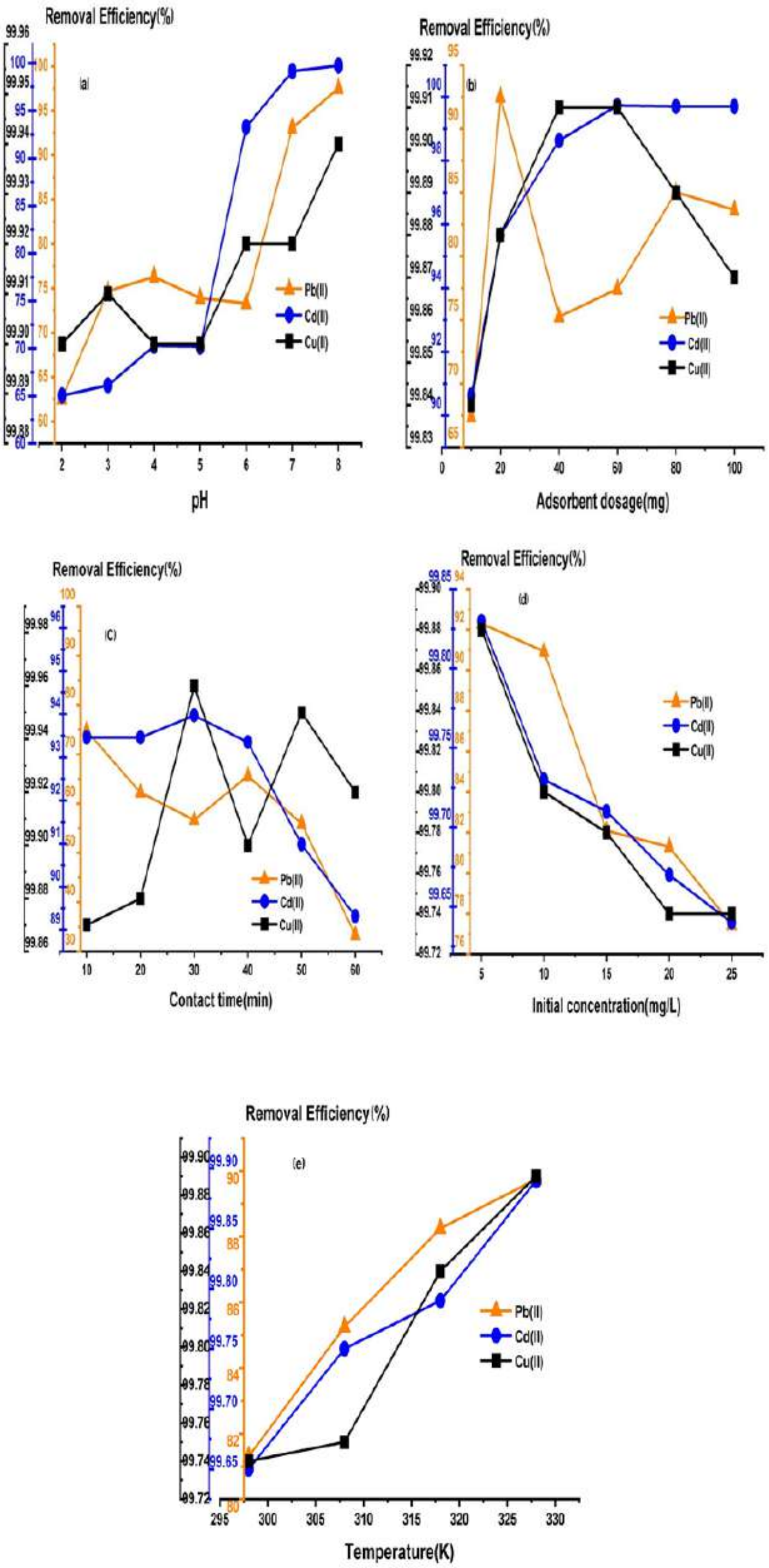

Figure IV.14: Selective adsorption of Pb(II), Cd(II), and Cu(II) ions onto NiO nanoparticles: (a) effect of pH, (b) effect of adsorbent dosage, (c) effect of contact time, (d) effect of initial concentration, and (e) effect of temperature.

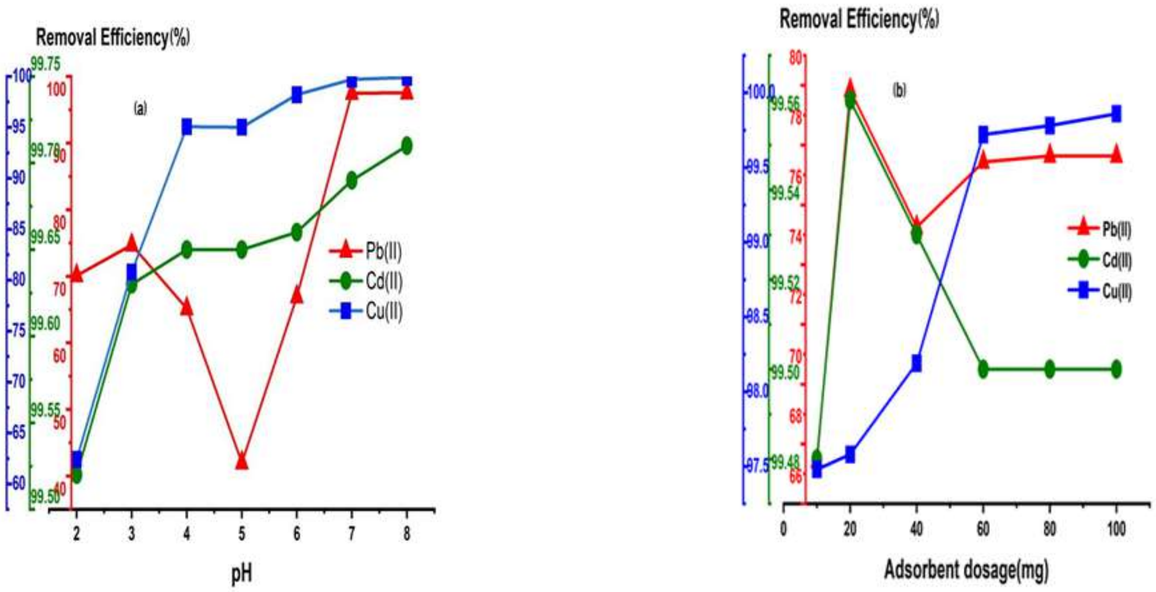

(a) Effect of pH **(b)** Effect of adsorbent dosage

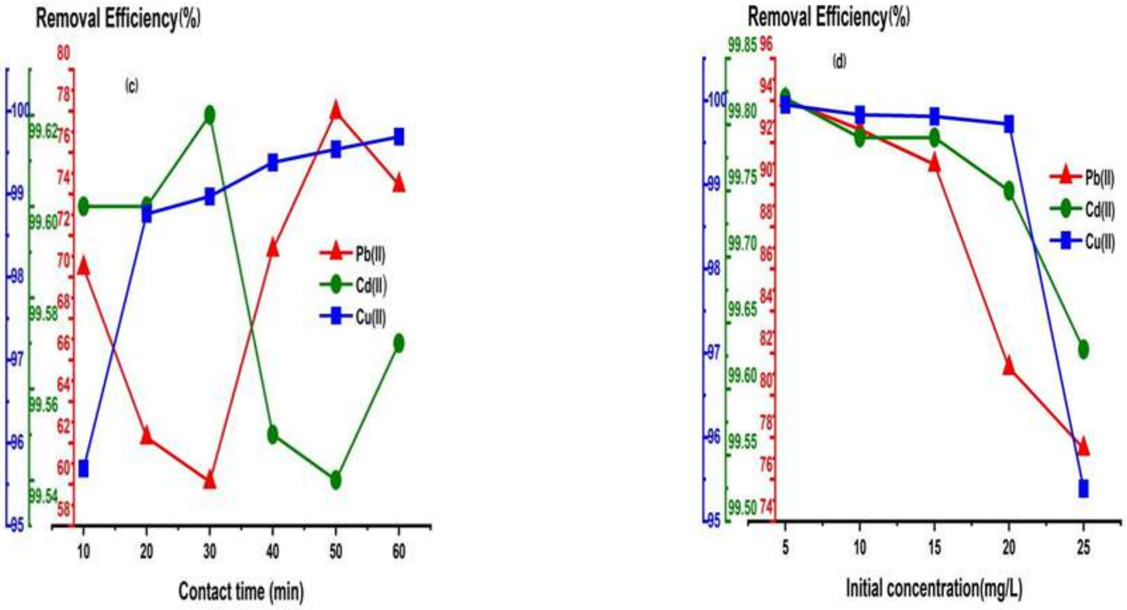

(c) Effect of contact time **(d)** Effect of initial concentration

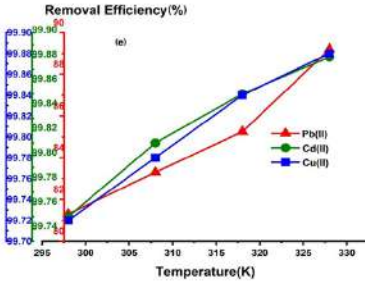

(e) Effect of temperature

Figure IV.15: Selective adsorption of Pb(II), Cd(II), and Cu(II) ions onto MnO_2/Mn_2O_3 nanoparticles: (a) effect of pH, (b) effect of adsorbent dosage, (c) effect of contact time, (d) effect of initial concentration, and (e) effect of temperature.

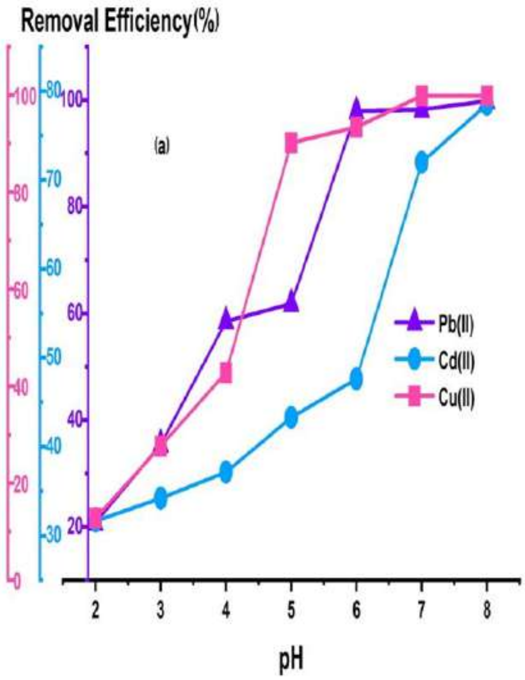

(a) Effect of pH

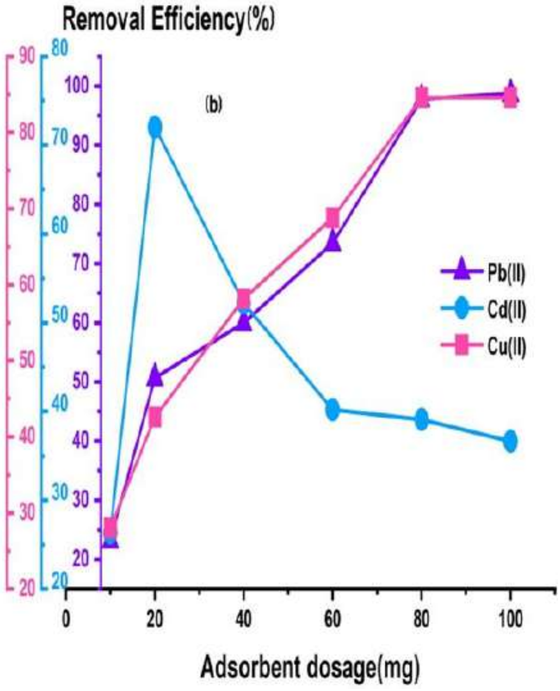

(b) Effect of adsorbent dosage

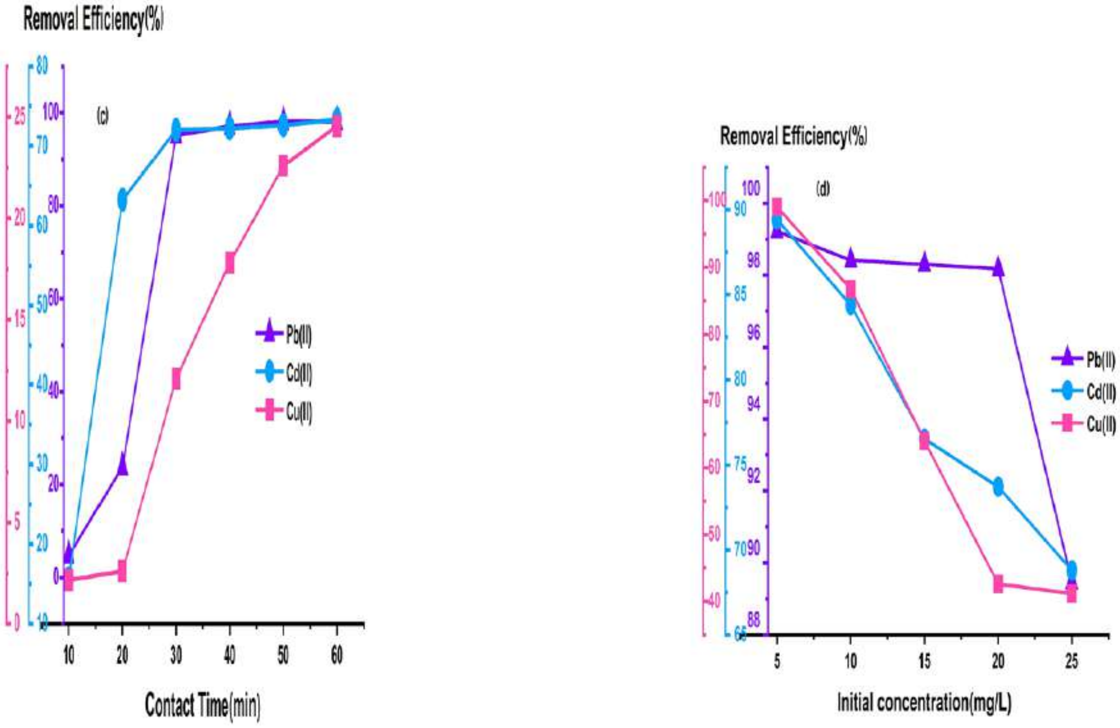

(c) Effect of contact time **(d)** Effect of initial concentration

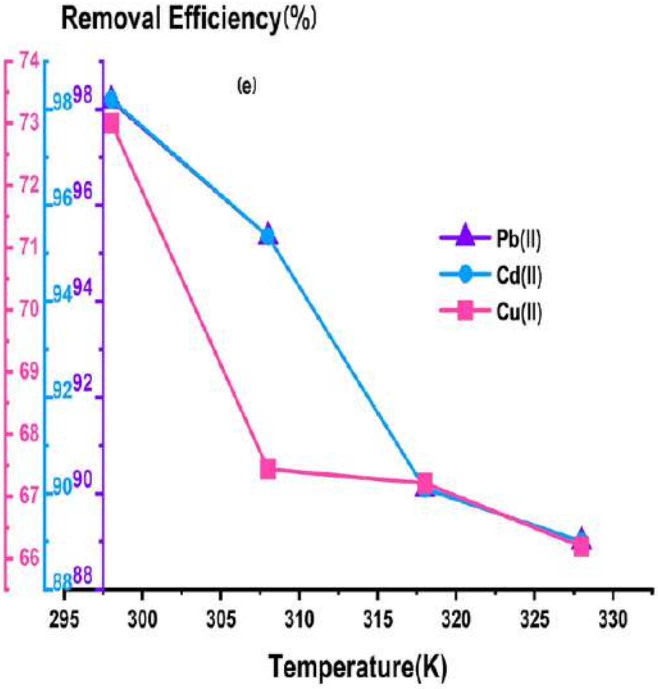

(e) Effect of temperature

Figure IV.16: Selective adsorption of Pb(II), Cd(II), and Cu(II) ions onto Mn_3O_4 nanoparticles: effects of pH, adsorbent dosage, contact time, initial concentration, and temperature.

IV.4 Adsorption Isotherm

In this study, the adsorption process was analyzed using the Freundlich and Langmuir isotherm models. These models were employed to identify the heterogeneous and homogeneous characteristics of the experimental data.

Figure IV.17 and Table IV.1 present the isotherm parameters for the adsorption of Pb(II), Cd(II), and Cu(II) onto NiO nanoparticles. As observed, the R^2 values of the Freundlich model are greater than those of the Langmuir model, confirming that the adsorption of the studied metal ions is better described by the Freundlich model. This suggests that the NiO nanoparticle surface is heterogeneous, allowing the formation of a multilayer adsorption. A suitable condition for the Freundlich isotherm is indicated by the adsorption intensity parameter n, which was calculated to be between 1 and 10 [**?**]. Specifically, the n values for Pb(II), Cd(II), and Cu(II) adsorption were 1.91, 1.45, and 1.37, respectively, suggesting favorable adsorption conditions, in agreement with previous studies [258, 259]. According to the Langmuir model, the theoretical maximum adsorption capacities ($q_{\max}$) followed the order: Cu (943.39 $\mathrm{mg\,g^{-1}}$) $>$ Cd (684.93 $\mathrm{mg\,g^{-1}}$) $>$ Pb (16.19 $\mathrm{mg\,g^{-1}}$).

Figure IV.18 and Table IV.1 show the isotherm parameters for Pb(II), Cd(II), and Cu(II) adsorption onto MnO_2/Mn_2O_3 nanoparticles. The high R^2 values indicate that the Langmuir model fits the experimental data better than the Freundlich model, suggesting monolayer adsorption on homogeneous sites. The Langmuir separation factor R_L indicates the favorability of adsorption: unfavorable ($R_L > 1$), linear ($R_L = 1$), favorable ($0 < R_L < 1$), or irreversible ($R_L = 0$) [248]. For Pb(II), Cd(II), and Cu(II), the computed R_L values were 0.04, 0.32, and 0.76, respectively, confirming favorable adsorption. The theoretical maximum adsorption capacities ($q_{\max}$) followed the order: Cu (2000 $\mathrm{mg\,g^{-1}}$) $>$ Cd (526.31 $\mathrm{mg\,g^{-1}}$) $>$ Pb (26.24 $\mathrm{mg\,g^{-1}}$).

Figure IV.19 and Table IV.1 present the Langmuir and Freundlich isotherm constants for Pb(II), Cd(II), and Cu(II) adsorption onto Mn_3O_4 nanoparticles. The higher R^2 values indicate that the experimental data are best described by the Langmuir model, confirming monolayer adsorption on homogeneous sites. The Langmuir separation factor R_L values were 0.24, 0.02, and 0.19 for Pb(II), Cd(II), and Cu(II), respectively, indicating favorable adsorption for all initial metal ion concentrations. The maximum adsorption capacities ($q_{\max}$) calculated from the Langmuir model followed the order: Pb (196.07 $\mathrm{mg\,g^{-1}}$) $>$ Cu (57.47

mg g^{-1}) > Cd (11.12 mg g^{-1}). caption subcaption

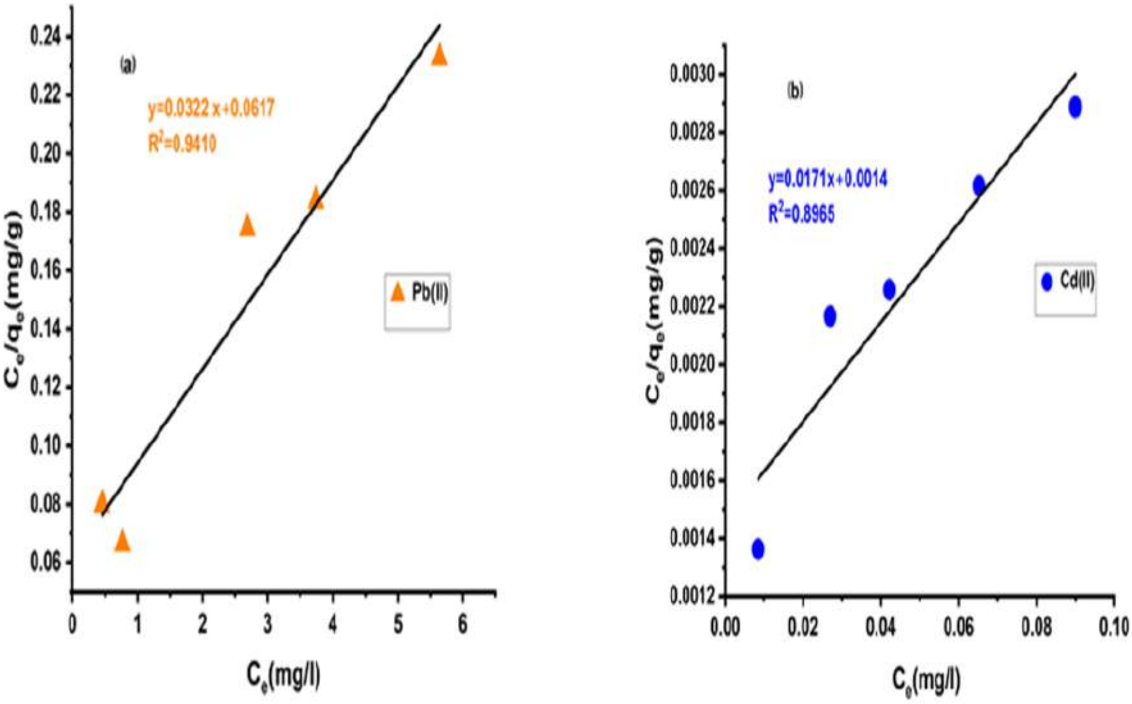

(a) Langmuir - Pb(II)

(b) Langmuir - Cd(II)

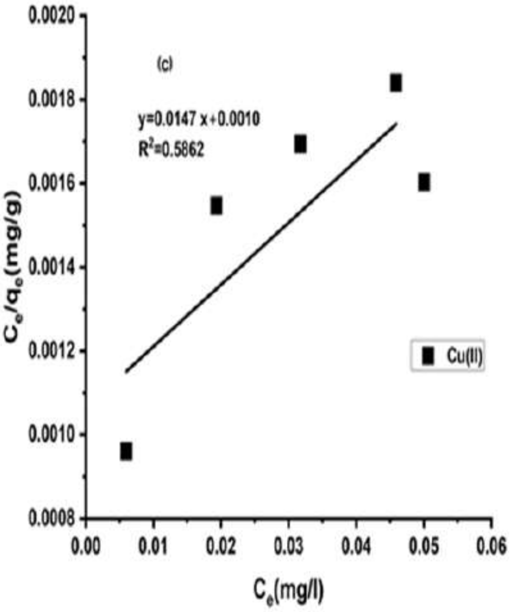

(c) Langmuir - Cu(II)

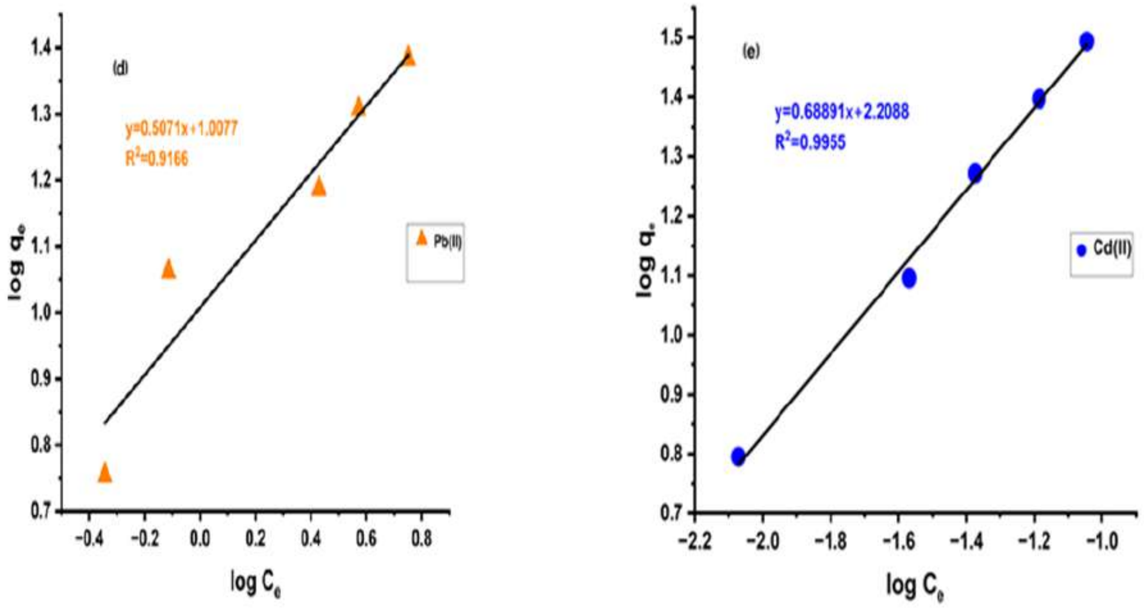

(d) Freundlich - Pb(II)

(e) Freundlich - Cd(II)

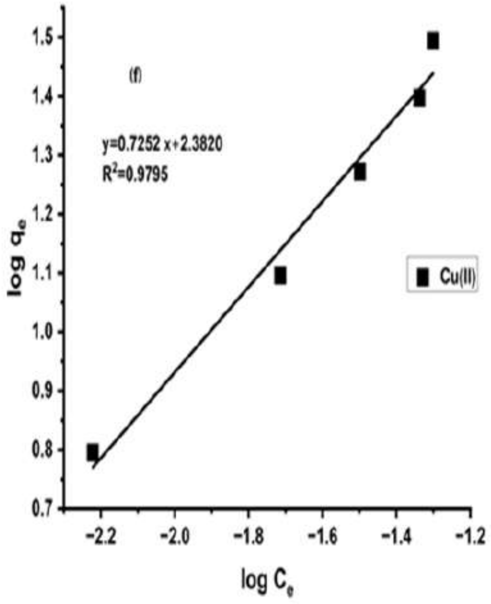

(f) Freundlich - Cu(II)

Figure IV.17: Langmuir (ac) and Freundlich (df) adsorption isotherms of Pb(II), Cd(II), and Cu(II) ions onto NiO nanoparticles.

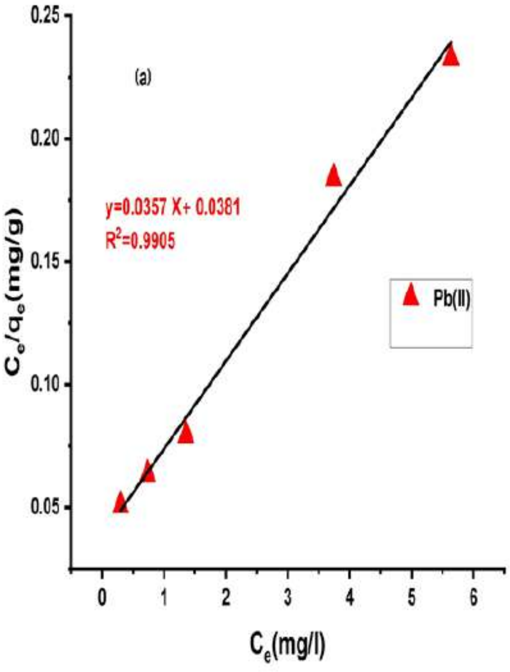

(a) Langmuir - Pb(II)

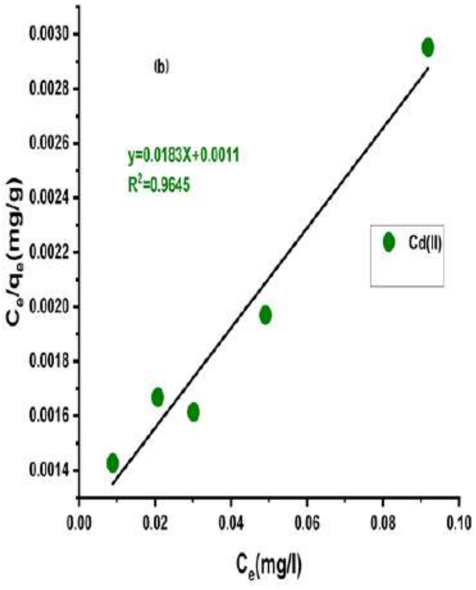

(b) Langmuir - Cd(II)

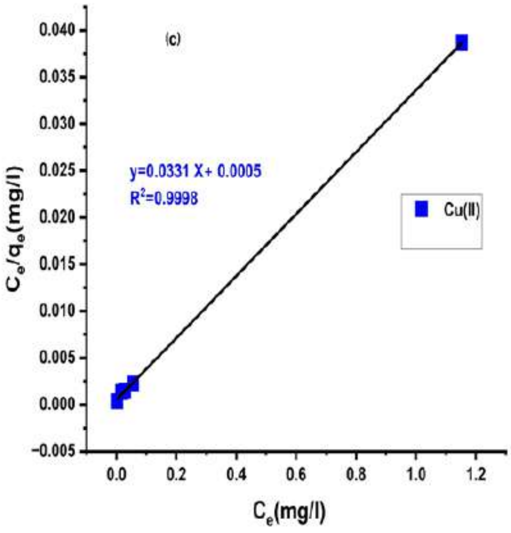

(c) Langmuir - Cu(II)

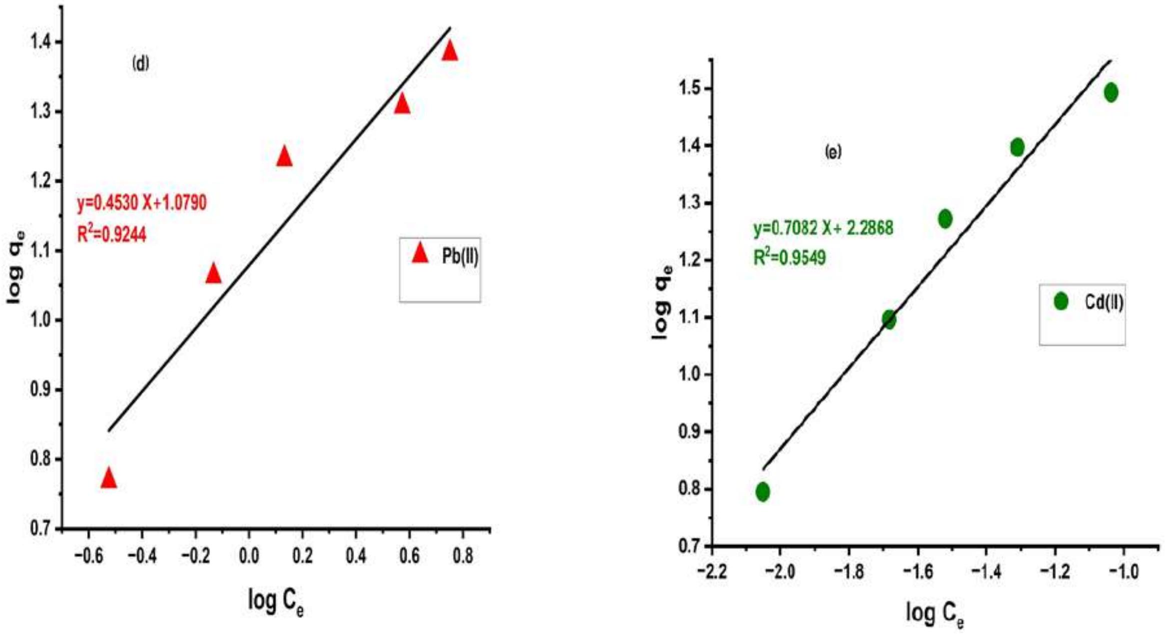

(d) Freundlich - Pb(II)

(e) Freundlich - Cd(II)

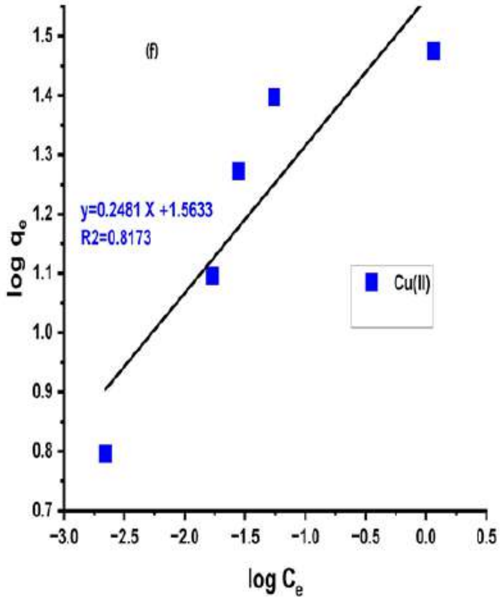

(f) Freundlich - Cu(II)

Figure IV.18: Langmuir (ac) and Freundlich (df) adsorption isotherms of Pb(II), Cd(II), and Cu(II) ions onto MnO_2/Mn_2O_3 nanoparticles.

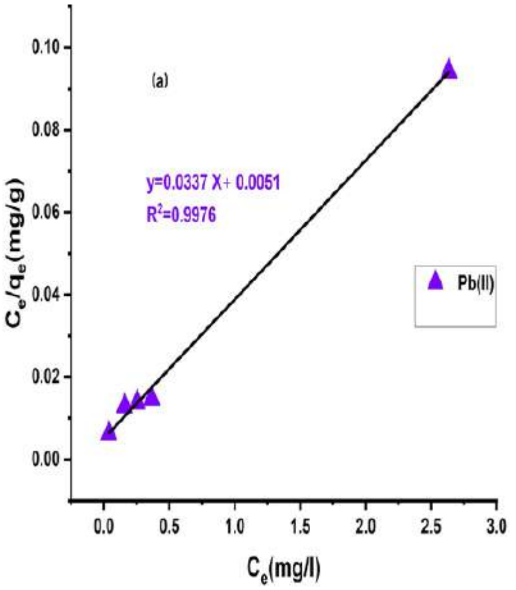

(a) Langmuir - Pb(II)

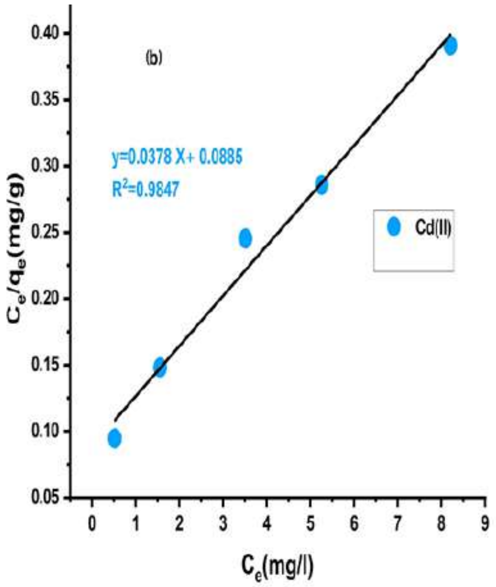

(b) Langmuir - Cd(II)

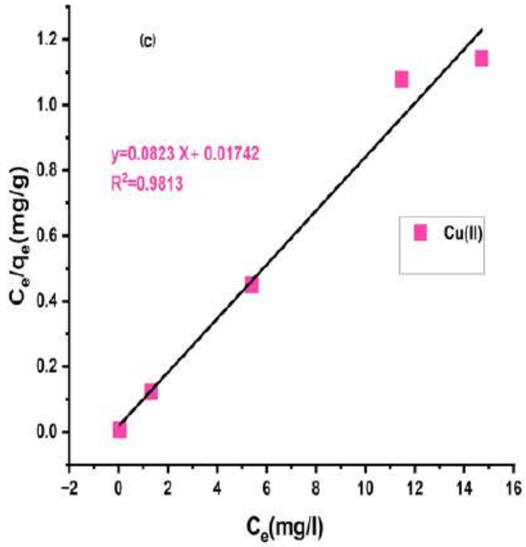

(c) Langmuir - Cu(II)

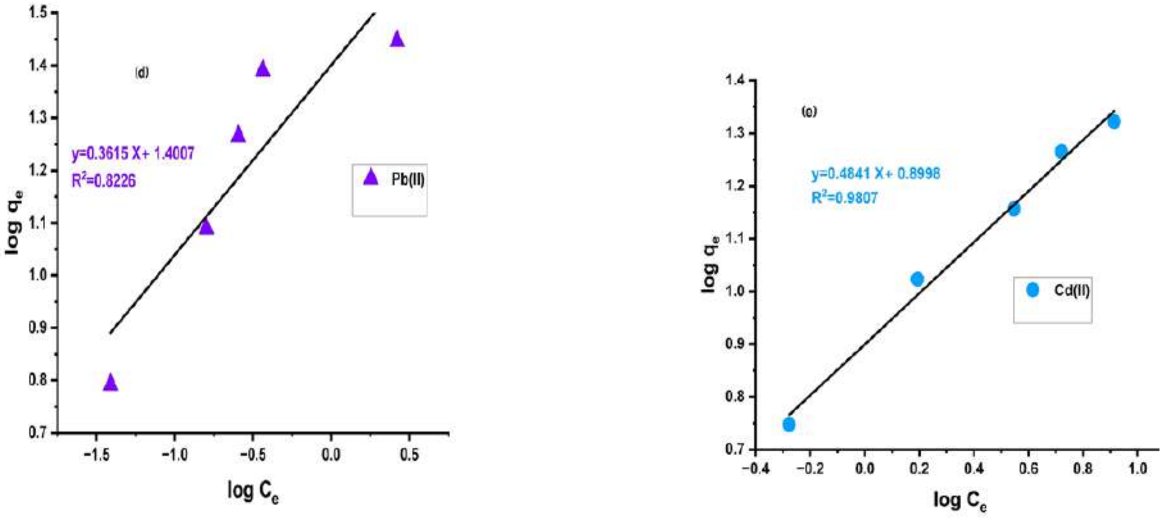

(d) Freundlich - Pb(II)

(e) Freundlich - Cd(II)

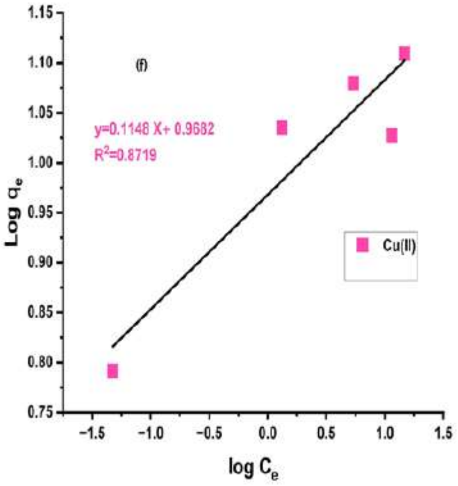

(f) Freundlich - Cu(II)

Figure IV.19: Langmuir (ac) and Freundlich (df) adsorption isotherms of Pb(II), Cd(II), and Cu(II) ions onto Mn_3O_4 nanoparticles.

Table IV.1: Estimated isotherm model parameters for Pb(II), Cd(II), and Cu(II) adsorption on NiO, MnO_2/Mn_2O_3, and Mn_3O_4 nanoparticles from wastewater under the conditions: $C_0 =$ 20 $\mathrm{mg\,L^{-1}}$, $pH = 7$, $m = 0.02$ g, $T = 25 \pm 2\,°$C, and $t = 30$ min.

Isotherm Model	Parameter	NiO NPs			MnO_2/Mn_2O_3 NPs			Mn_3O_4 NPs		
		Pb	Cd	Cu	Pb	Cd	Cu	Pb	Cd	Cu
Langmuir	$q_{\max}$ (mg/g)	16.19	684.93	943.39	26.24	526.31	2000	196.00	11.29	57.47
	K_L (L/mg)	1.91	0.08	0.07	1.06	0.10	0.015	0.15	2.34	0.21
	R_L	0.04	0.51	0.56	0.04	0.32	0.76	0.24	0.02	0.19
	R^2	0.94	0.89	0.58	0.99	0.96	0.99	0.99	0.984	0.98
Freundlich	K_f (mg/g)	10.18	161.75	241.00	11.99	193.55	36.58	25.15	7.93	8.67
	n	1.91	1.45	1.37	2.20	1.41	4.03	2.76	2.06	8.71
	R^2	0.91	0.99	0.97	0.92	0.95	0.81	0.82	0.980	0.87

IV.5 Adsorption Kinetics

The adsorption kinetics of the synthesized nanoparticles were evaluated to understand their adsorption behavior. The most important factors influencing sorbent efficiency are rapid adsorption, high equilibrium capacity (q_e), and short contact time. The adsorption kinetics of M^{2+} ions were modeled using the pseudo-first-order and pseudo-second-order equations (Equations (II.1) and (II.2) in Chapter II). In these models, k_1 ($\mathrm{min^{-1}}$) represents the pseudo-first-order rate constant, q_t is the amount adsorbed at time t, q_e is the adsorption capacity at equilibrium, and k_2 ($\mathrm{g\,mg^{-1}\,min^{-1}}$) is the pseudo-second-order rate constant. The most suitable model was selected based on the correlation coefficient (R^2).

According to the modeling results (Table IV.2 and Figures IV.20–IV.21), the adsorption of Pb(II), Cd(II), and Cu(II) onto NiO and MnO_2/Mn_2O_3 nanoparticles follows pseudo-second-order kinetics, as indicated by higher R^2 values. Moreover, the q_e values calculated from the pseudo-second-order equation closely match the experimental q_e values, confirming the validity of this model. The pseudo-second-order model correlates adsorption capacity with the number of active sites on the nanosorbent surface [260]. It is well known that this model suggests a chemisorption mechanism involving covalent bonding and ion-exchange forces [261].

In contrast, Pb(II), Cd(II), and Cu(II) adsorption on Mn_3O_4 nanoparticles showed very low correlation coefficients for the pseudo-second-order model (Table IV.2 and Figure IV.22).

Additionally, the calculated and experimental q_e values were inconsistent. However, the pseudo-first-order model gave excellent linearity with high R^2 values and good agreement between calculated and experimental q_e. This indicates that adsorption onto Mn_3O_4 occurs mainly through physical adsorption. Similar findings were reported in previous studies that successfully described Pb(II) and Cd(II) adsorption using pseudo-first-order kinetics [262, 263].

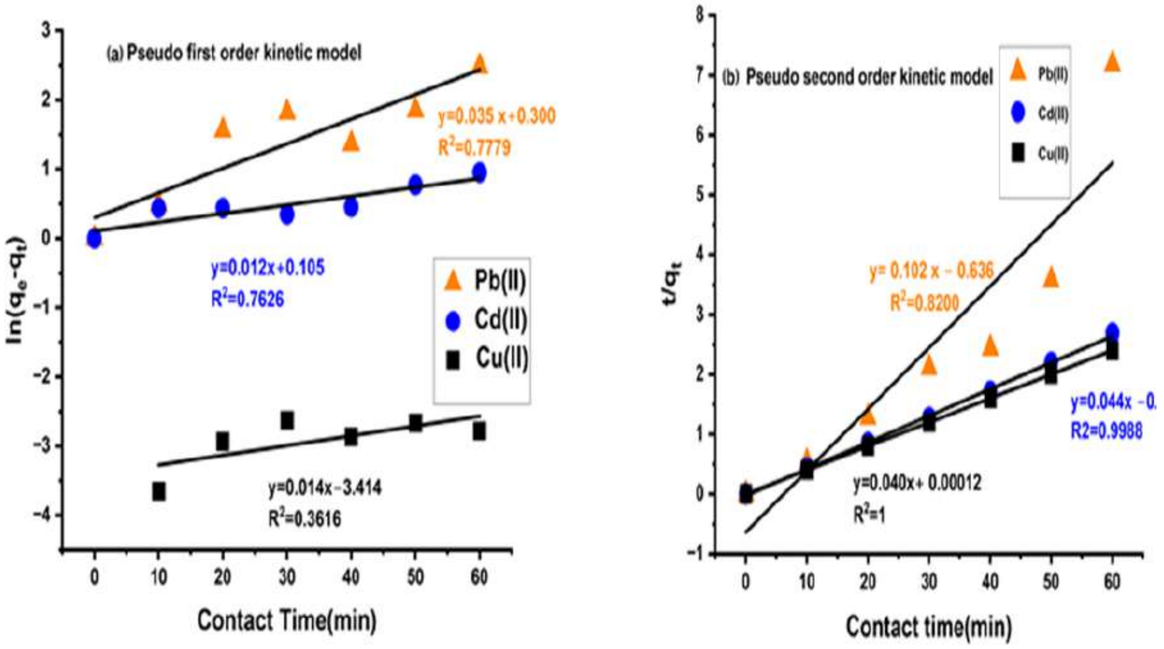

Figure IV.20: (a) Pseudo-first-order and (b) pseudo-second-order kinetic models for Pb(II), Cd(II), and Cu(II) adsorption onto NiO nanoparticles ($C_0 = 20\ \mathrm{mg\,L^{-1}}$, dose = 0.02 g, pH = 7).

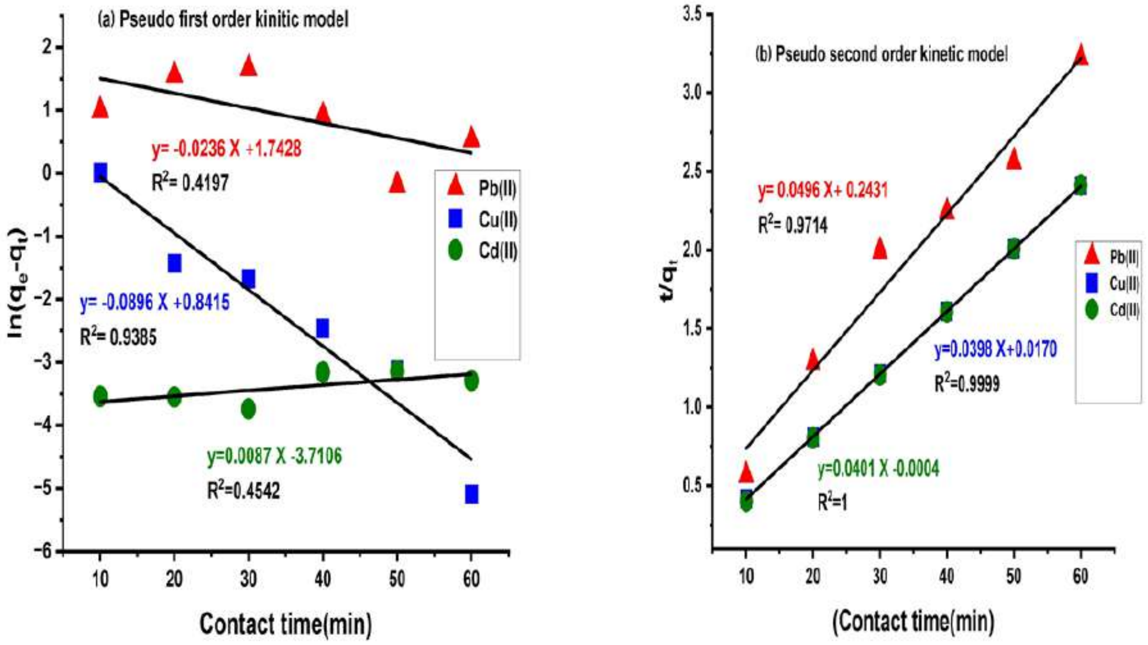

Figure IV.21: (c) Pseudo-first-order and (d) pseudo-second-order kinetic models for Pb(II), Cd(II), and Cu(II) adsorption onto MnO_2/Mn_2O_3 nanoparticles under the same conditions.

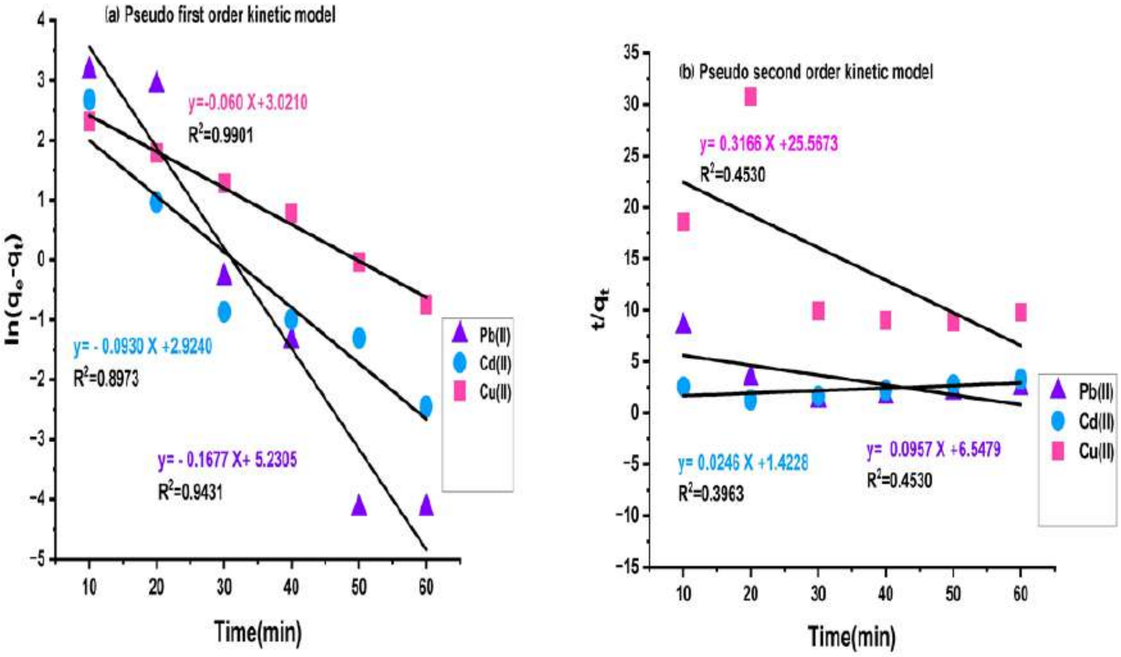

Figure IV.22: (e) Pseudo-first-order and (f) pseudo-second-order kinetic models for Pb(II), Cd(II), and Cu(II) adsorption onto Mn_3O_4 nanoparticles under the same conditions.

Table IV.2: Kinetic model parameters for Pb(II), Cd(II), and Cu(II) adsorption onto NiO, MnO_2/Mn_2O_3, and Mn_3O_4 nanoparticles from wastewater under the conditions: $C_0 = 20$ mg L^{-1}, pH = 7, $m = 0.02$ g, $T = 25 \pm 2\,°C$, and $t = 30$ min.

Model	Parameter	NiO NPs			MnO_2/Mn_2O_3 NPs			Mn_3O_4 NPs		
		Pb	Cd	Cu	Pb	Cd	Cu	Pb	Cd	Cu
$q_{e,\mathrm{exp}}$ (mg/g)		18.68	23.49	24.99	19.48	24.90	24.92	24.52	18.33	6.13
Pseudo-first order	$q_{e,\mathrm{cal}}$ (mg/g)	51.35	21.11	40.03	5.71	0.02	2.31	186.8	18.61	20.51
	k_1 (1/min)	-0.03	-0.01	-0.01	0.02	-0.008	0.08	0.167	0.093	0.060
	R^2	0.77	0.76	0.36	0.41	0.45	0.93	0.94	0.89	0.99
Pseudo-second order	$q_{e,\mathrm{cal}}$ (mg/g)	9.72	22.47	24.98	20.14	24.93	25.12	10.44	40.65	3.15
	k_2 (g/mgůmin)	-0.01	-0.07	-0.04	0.01	-4.02	0.09	0.000	4×10^{-3}	0.003
	R^2	0.82	0.99	1.00	0.97	1.00	0.99	0.45	0.39	0.45

IV.6 Adsorption Thermodynamics

The thermodynamic behavior of Pb(II), Cd(II), and Cu(II) adsorption onto NiO, MnO_2/Mn_2O_3, and Mn_3O_4 nanoparticles was examined at different temperatures (298, 308, 318, and 328 K). The thermodynamic parameters—standard Gibbs free energy change ($\Delta G°$), enthalpy change ($\Delta H°$), and entropy change ($\Delta S°$)—were calculated using Equations (II.13) and (II.14). The estimated parameters are summarized in Table IV.3.

Figures (IV.24–IV.26) illustrate the thermodynamic plots for the adsorption of Pb(II), Cd(II), and Cu(II) ions onto the three nano-adsorbents. The linearity of the plots confirms the applicability of the thermodynamic model, with correlation coefficients of $R^2 = 0.9896$, 0.9768, and 0.9330 for Pb^{2+}; $R^2 = 0.9390$, 0.9434, and 0.7657 for Cd^{2+}; and $R^2 = 0.9131$, 0.9428, and 0.9839 for Cu^{2+} adsorption onto NiO, MnO_2/Mn_2O_3, and Mn_3O_4 NPs, respectively.

Table IV.3: Estimated thermodynamic parameters for Pb(II), Cd(II), and Cu(II) adsorption onto NiO, MnO_2/Mn_2O_3, and Mn_3O_4 nanoparticles from wastewater under the conditions: $C_0 = 20$ mg L^{-1}, pH = 7, $m = 0.02$ g, and $t = 30$ min.

Adsorbent	**Metal ion**	ΔH° (kJ/mol)	ΔS° (kJ/molůK)	ΔG° (kJ/mol)		
				25°C	35°C	45°C
NiO NPs	Pb(II)	19.253	0.078	-4.193	-5.063	-5.920
	Cd(II)	29.728	0.148	-14.554	-15.907	-16.949
	Cu(II)	25.113	0.134	-15.290	-15.950	-17.600
MnO_2/Mn_2O_3 NPs	Pb(II)	17.842	0.073	-4.193	-4.686	-5.228
	Cd(II)	19.931	0.118	-15.390	-16.680	-17.794
	Cu(II)	23.492	0.129	-15.109	-16.270	-17.639
Mn_3O_4 NPs	Pb(II)	-53.121	-0.1445	-10.419	-8.306	-6.428
	Cd(II)	-8.061	-0.017	-3.017	-2.435	-2.487
	Cu(II)	-1.851	-0.007	0.246	0.339	0.394

From Table IV.3, all ΔG° values for Pb(II), Cd(II), and Cu(II) adsorption onto NiO and MnO_2/Mn_2O_3 nanoparticles are negative, indicating that the adsorption is spontaneous and thermodynamically favorable. The negative values additionally suggest that the adsorption mechanism is predominantly physical rather than chemical [264].

However, the adsorption of Cu(II) ions onto Mn_3O_4 nanoparticles exhibits positive ΔG° values over the temperature range 298–328 K, suggesting that this process is non-spontaneous under the studied conditions.

Consistent with previously reported trends regarding the effect of temperature [253], the positive ΔH° values for NiO and MnO_2/Mn_2O_3 indicate that the adsorption process is endothermic. The relatively low magnitude of ΔH° suggests that the adsorption requires minimal energy input, which agrees with the observed increase in adsorption capacity with rising temperature. The positive ΔS° values further indicate an increase in randomness at the solid–liquid interface during adsorption.

In contrast, Mn_3O_4 nanoparticles exhibit negative ΔH° values, indicating an exothermic adsorption process. The negative ΔS° values imply decreased randomness at the interface and suggest that no significant structural changes occur within the adsorbent during the adsorption of metal ions onto Mn_3O_4 nanoparticles [265].

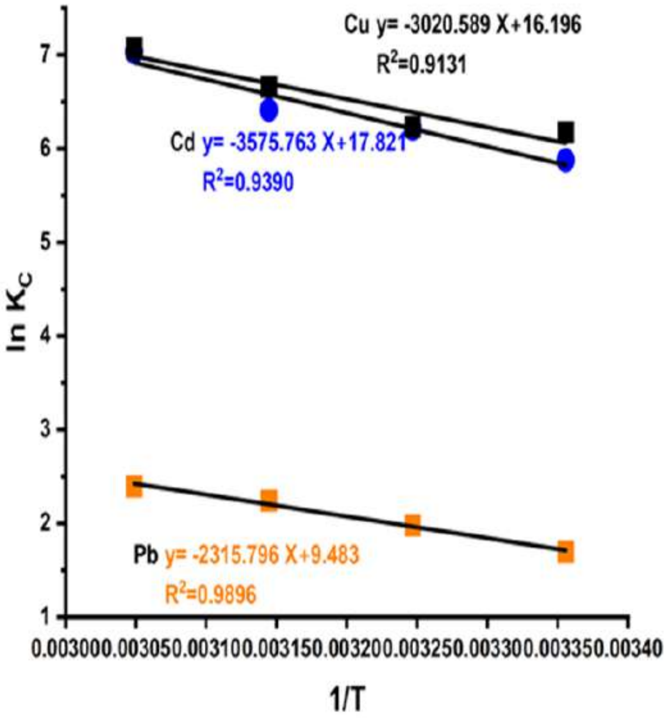

Figure IV.23: Thermodynamic isotherm of Pb(II), Cd(II), and Cu(II) ions adsorption on NiO nanoparticles.

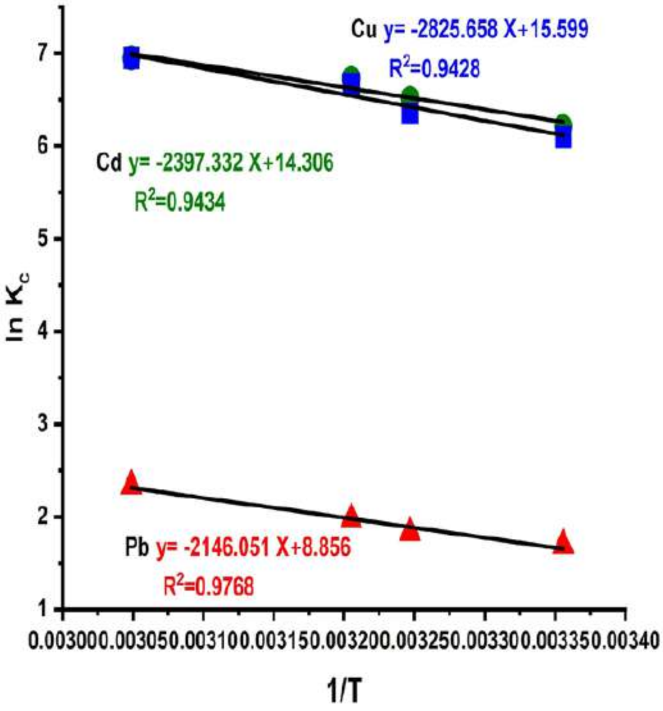

Figure IV.24: Thermodynamic isotherm of Pb(II), Cd(II), and Cu(II) ions adsorption on MnO_2/Mn_2O_3 nanoparticles.

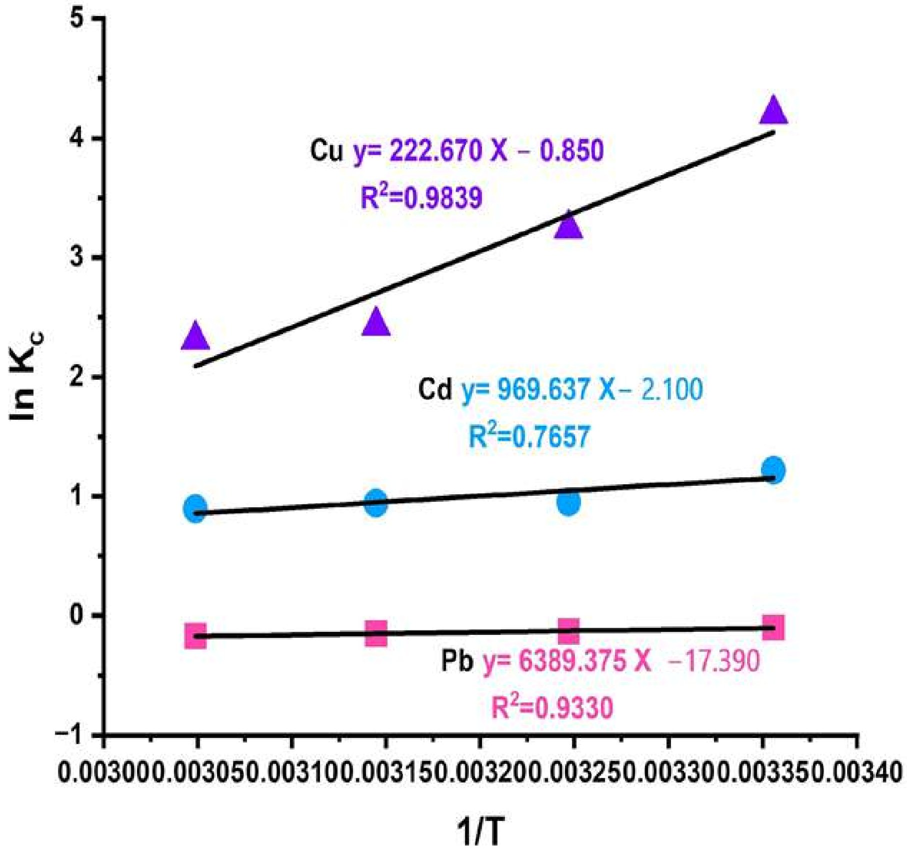

Figure IV.25: Thermodynamic isotherm of Pb(II), Cd(II), and Cu(II) ions adsorption on Mn_3O_4 nanoparticles.

.

General Conclusion

General Conclusion

The green synthesis of metal oxide nanoparticles represents a sustainable and eco-friendly alternative to conventional chemical methods. In this study, NiO, MnO_2/Mn_2O_3, and Mn_3O_4 nanoparticles were successfully synthesized using *Helianthus annuus* seed husk extract, an abundant agricultural waste serving as both a reducing and stabilizing agent. This facile, low-cost, and environmentally benign approach demonstrates the potential of plant-mediated synthesis for advanced nanomaterials.

Comprehensive characterization via UVVis, FT-IR, XRD, SEM, EDX, and BET confirmed the formation of crystalline nanoparticles with average sizes of 14.11 nm (NiO), 26.93 nm (MnO_2/Mn_2O_3), and 20.3 nm (Mn_3O_4) as calculated using the Scherrer equation.

The adsorption performance toward Pb(II), Cd(II), and Cu(II) ions was systematically evaluated under varying parameters (adsorbent dose, initial metal concentration, pH, contact time, and temperature). Optimal removal efficiencies reached 81.30%, 99.64%, and 99.74% for NiO–NPs; 81.31%, 99.75%, and 99.72% for MnO_2/Mn_2O_3–NPs; and 98.17%, 73.70%, and 42.60% for Mn_3O_4–NPs, respectively.

Kinetic modeling indicated pseudo-second-order adsorption for NiO and MnO_2/Mn_2O_3, while Mn_3O_4 followed pseudo-first-order kinetics. Equilibrium studies revealed that the Langmuir isotherm best described MnO_2/Mn_2O_3 and Mn_3O_4 adsorption, reflecting monolayer coverage, whereas NiO adsorption fit the Freundlich model, indicative of surface heterogeneity. The maximum adsorption capacities (q_m) based on Langmuir modeling were 16.19, 684.93, and 943.39 mg/g for NiO; 26.24, 526.31, and 2000 mg/g for MnO_2/Mn_2O_3; and 196, 11.29, and 57.47 mg/g for Mn_3O_4 toward Pb(II), Cd(II), and Cu(II), respectively.

Thermodynamic analysis showed negative ΔG° values for Pb(II), Cd(II), and Cu(II) adsorption on NiO and MnO_2/Mn_2O_3, confirming a spontaneous, predominantly physical adsorption process. In contrast, Cu(II) adsorption on Mn_3O_4 exhibited positive ΔG°, indicating non-spontaneous behavior under the studied conditions.

Overall, green-synthesized NiO and Mn oxide nanoparticles are efficient, sustainable, and cost-effective nanosorbents, demonstrating strong potential for heavy metal removal, wastewater purification, and broader environmental remediation. Future work should explore scale-up synthesis, adsorbent regeneration, and reuse in continuous systems. Furthermore, combining these nanoparticles with biopolymers, carbon-based materials, or magnetic supports could enhance selectivity, recovery, and adsorption capacity. Comprehensive ecotoxicological and life-cycle assessments are also recommended to ensure environmental safety and guide the development of next-generation green nanosorbents for industrial applications.

Bibliography

Bibliography

[1] Mahmoud, A.E.D., et al., Green copper oxide nanoparticles for lead, nickel, and cadmium removal from contaminated water. *Scientific Reports*, 2021. 11(1): p. 12547.

[2] El Din Mahmoud, A. and M. Fawzy, Bio-based Methods for Wastewater Treatment: Green Sorbents, in *Phytoremediation: Management of Environmental Contaminants*, Volume 3, A.A. Ansari, et al., Editors. 2016, Springer International Publishing: Cham. p. 209–238.

[3] Ergüvenerler, F., . Targan, and V.N. Tirtom, Removal of lead from aqueous solutions by low cost and waste biosorbents (lemon, bean and artichoke shells). *Water Science and Technology*, 2020. 81(1): p. 159–169.

[4] Sigel, H. and R. Sigel, *Metal Ions in Biological Systems*, Volume 43: Biogeochemical Cycles of Elements, 2005: CRC Press.

[5] World Health Organization, *World Health Statistics 2010*, 2010: WHO.

[6] Zaini, M.A.A., R. Okayama, and M. Machida, Adsorption of aqueous metal ions on cattle-manure-compost based activated carbons. *Journal of Hazardous Materials*, 2009. 170(2–3): p. 1119–1124.

[7] Bilal, M., et al., Waste biomass adsorbents for copper removal from industrial wastewatera review. *Journal of Hazardous Materials*, 2013. 263: p. 322–333.

[8] Hu, X.-J., et al., Removal of Cu(II) ions from aqueous solution using sulfonated magnetic graphene oxide composite. *Separation and Purification Technology*, 2013. 108: p. 189–195.

[9] Lan, S., et al., Synthesis and characterization of hyaluronic acid-supported magnetic microspheres for copper ions removal. *Colloids and Surfaces A: Physicochemical and Engineering Aspects*, 2013. 425: p. 42–50.

[10] Al-Gheethi, A., et al., Bioaugmentation process of secondary effluents for reduction of pathogens, heavy metals and antibiotics. *Journal of Water and Health*, 2016. 14(5): p. 780–795.

[11] Qiao, Y., et al., Remediation of cadmium in soil by biochar-supported iron phosphate nanoparticles. *Ecological Engineering*, 2017. 106: p. 515–522.

[12] Thines, R., et al., Application potential of carbon nanomaterials in water and wastewater treatment: a review. *Journal of the Taiwan Institute of Chemical Engineers*, 2017. 72: p. 116–133.

[13] Schneider, A., et al., Perspectives on adsorption technology as an effective strategy for continuous downstream bioprocessing. *Journal of Chemical Technology & Biotechnology*, 2022. 97(9): p. 2305–2316.

[14] El-Enein, S.A., et al., Adsorption of selected metals ions in solution using nano-bentonite particles: Isotherms and kinetics. *Environmental Processes*, 2020. 7: p. 463–477.

[15] Saleem, J., et al., Production and applications of activated carbons as adsorbents from olive stones. *Biomass Conversion and Biorefinery*, 2019. 9: p. 775–802.

[16] Venkatalakshmi, N., H.J. Kini, and H.B. Naik, Green-synthesized nickel oxide nanoparticles: magnetic and biomedical applications. *Inorganic Chemistry Communications*, 2023. 151: p. 110490.

[17] Sahila, S., et al., A novel green and eco-friendly synthesis of nickel oxide nanoparticles by auto combustion technique using Allium cepa bulb extract and their dielectric behaviour. *Chemical Data Collections*, 2022. 38: p. 100837.

[18] Dessie, Y., S. Tadesse, and R. Eswaramoorthy, Physicochemical parameter influences and their optimization on the biosynthesis of MnO2 nanoparticles using *Vernonia amygdalina* leaf extract. *Arabian Journal of Chemistry*, 2020. 13(8): p. 6472–6492.

[19] Reddy, R.N. and R.G. Reddy, Synthesis and electrochemical characterization of amorphous MnO2 electrochemical capacitor electrode material. *Journal of Power Sources*, 2004. 132(1–2): p. 315–320.

[20] Olajire, A. and A. Mohammed, Green synthesis of nickel oxide nanoparticles and studies of their photocatalytic activity in degradation of polyethylene films. *Advanced Powder Technology*, 2020. 31(1): p. 211–218.

[21] Dewi, N.O.M. and Y. Yulizar, *Euphorbia heterophylla* L. leaf extract-mediated synthesis of MnO2 nanoparticles and its characterization. *Materials Today: Proceedings*, 2020. 22: p. 199–204.

[22] Uddin, S., et al., Green synthesis of nickel oxide nanoparticles using leaf extract of *Berberis balochistanica*: Characterization, and diverse biological applications. *Microscopy Research and Technique*, 2021. 84(9): p. 2004–2016.

[23] Mansoori, G.A. and T.A.F. Soelaiman, Nanotechnology An Introduction for the Standards Community. *Journal of ASTM International*, 2005. 2: p. 1–21.

[24] Bayda, S., et al., The History of Nanoscience and Nanotechnology: From Chemical-Physical Applications to Nanomedicine. *Molecules*, 2019. 25(1).

[25] Durlo, A., 1950–2022: A History of Nanotechnology into Physical and Mathematical Relationship, 2023, Université de Lille.

[26] Bhatia, S., *Natural polymer drug delivery systems*, 2016: Springer.

[27] Saratale, R.G., et al., A comprehensive review on green nanomaterials using biological systems: Recent perception and their future applications. *Colloids and Surfaces B: Biointerfaces*, 2018. 170: p. 20–35.

[28] Suman, T., et al., Biosynthesis, characterization and cytotoxic effect of plant mediated silver nanoparticles using *Morinda citrifolia* root extract. *Colloids and Surfaces B: Biointerfaces*, 2013. 106: p. 74–78.

[29] Alagarasi, A., Chapter-introduction to nanomaterials. Indian Institute of Technology Madras, 2013: p. 1–24.

[30] Mekuye, B. and B. Abera, Nanomaterials: An overview of synthesis, classification, characterization, and applications. *Nano Select*, 2023. 4: p. 486–501.

[31] Piard, J., et al., Synthèse et détermination de la taille de nanoprismes d'argent. *Le Bulletin de l'Union des Professeurs de Physique et de Chimie*, 2016. 110(988): p. 1339–1368.

[32] Hasan, S., A review on nanoparticles: their synthesis and types. *Research Journal of Recent Sciences*, 2015. 2277: p. 2502.

[33] Smita, S., et al., Nanoparticles in the environment: assessment using the causal diagram approach. *Environmental Health*, 2012. 11(1): p. S13.

[34] Cho, E.J., et al., Nanoparticle characterization: state of the art, challenges, and emerging technologies. *Molecular Pharmaceutics*, 2013. 10(6): p. 2093–2110.

[35] NANOMATERIAUX, L., Effets sur la santé de lhomme et sur lenvironnement, 2006, Afsset July.

[36] Buzea, C., I. Pacheco, and K. Robbie, Nanomaterials and nanoparticles: sources and toxicity. *Biointerphases*, 2007. 2: MR17–71.

[37] Cho, G., et al., Ion exchange: an advanced synthetic method for complex nanoparticles. *Nano Convergence*, 2019. 6: p. 1–17.

[38] Tiwari, D.K., J. Behari, and P.S. Prasenjit Sen, Application of nanoparticles in wastewater treatment, 2008.

[39] Ealia, S.A.M. and M.P. Saravanakumar, A review on the classification, characterization, synthesis of nanoparticles and their application. In *IOP Conference Series: Materials Science and Engineering*, 2017, IOP Publishing.

[40] Salavati-Niasari, M., F. Davar, and N. Mir, Synthesis and characterization of metallic copper nanoparticles via thermal decomposition. *Polyhedron*, 2008. 27(17): p. 3514–3518.

[41] Singh, A.K., *Engineered nanoparticles: structure, properties and mechanisms of toxicity*, 2015: Academic Press.

[42] Ijaz, I., et al., Detailed review on chemical, physical and green synthesis, classification, characterizations and applications of nanoparticles. *Green Chemistry Letters and Reviews*, 2020. 13(3): p. 223–245.

[43] Bhaviripudi, S., et al., CVD synthesis of single-walled carbon nanotubes from gold nanoparticle catalysts. *Journal of the American Chemical Society*, 2007. 129(6): p. 1516–1517.

[44] Joudeh, N. and D. Linke, Nanoparticle classification, physicochemical properties, characterization, and applications: a comprehensive review for biologists. *Journal of Nanobiotechnology*, 2022. 20(1): p. 262.

[45] TEREA, H., Application of cellulose/ZnO nanocomposite on the removal of toxic pollutants from aqueous solutions, 2023, University of Kasdi Merbah–Ouergla.

[46] Yan, K., T. Lafleur, and J. Liao, Facile synthesis of palladium nanoparticles supported on multi-walled carbon nanotube for efficient hydrogenation of biomass-derived levulinic acid. *Journal of Nanoparticle Research*, 2013. 15: p. 1–7.

[47] Buffet, P.-E., Évaluation du risque environnemental des nanoparticules métalliques: biodisponibilité et risque potentiel pour deux espèces clés des écosystèmes estuariens, 2012, Nantes.

[48] Li, W., Elaboration par un procédé de précipitation de nanoparticules aux propriétés contrôlées: application à la magnétite, 2011, Institut National Polytechnique de Lorraine.

[49] Bhagyaraj, S.M. and O.S. Oluwafemi, Nanotechnology: the science of the invisible, in *Synthesis of Inorganic Nanomaterials*, 2018, Elsevier. p. 1–18.

[50] Khan, I., K. Saeed, and I. Khan, Nanoparticles: Properties, applications and toxicities. *Arabian Journal of Chemistry*, 2019. 12(7): p. 908–931.

[51] Huang, C., et al., Effect of structure: A new insight into nanoparticle assemblies from inanimate to animate. *Science Advances*, 2020. 6(20): p. eaba1321.

[52] Arole, V. and S. Munde, Fabrication of nanomaterials by top-down and bottom-up approachesan overview. *J. Mater. Sci*, 2014. 1: p. 89–93.

[53] Khan, F.A., Synthesis of nanomaterials: methods & technology. *Applications of Nanomaterials in Human Health*, 2020: p. 15–21.

[54] Rane, A.V., et al., Methods for synthesis of nanoparticles and fabrication of nanocomposites, in *Synthesis of Inorganic Nanomaterials*, 2018, Elsevier. p. 121–139.

[55] Altammar, K.A., A review on nanoparticles: characteristics, synthesis, applications, and challenges. *Frontiers in Microbiology*, 2023. 14: p. 1155622.

[56] Nath, D. and P. Banerjee, Green nanotechnologya new hope for medical biology. *Environmental Toxicology and Pharmacology*, 2013. 36(3): p. 997–1014.

[57] Narayanan, K.B. and N. Sakthivel, Green synthesis of biogenic metal nanoparticles by terrestrial and aquatic phototrophic and heterotrophic eukaryotes and biocompatible agents. *Advances in Colloid and Interface Science*, 2011. 169(2): p. 59–79.

[58] Gardea-Torresdey, J.L., et al., Formation and growth of Au nanoparticles inside live alfalfa plants. *Nano Letters*, 2002. 2(4): p. 397–401.

[59] Rani, A., N. Kumar, and M. Kumar, Environmentally friendly green approaches and applications of nanoparticles, in *Metal OxideBased Carbon Nanocomposites for Environmental Remediation and Safety*, 2023, CRC Press. p. 21–63.

[60] Hano, C. and B.H. Abbasi, Plant-based green synthesis of nanoparticles: Production, characterization and applications, 2021, MDPI. p. 31.

[61] Nasrollahzadeh, M., et al., Recent developments in the biosynthesis of Cubased recyclable nanocatalysts using plant extracts and their application in chemical reactions. *The Chemical Record*, 2019. 19(2-3): p. 601–643.

[62] Dinesh, G.K., M. Pramod, and S. Chakma, Sonochemical synthesis of amphoteric Cu0-Nanoparticles using *Hibiscus rosa-sinensis* extract and their applications for degradation of 5-fluorouracil and lovastatin drugs. *Journal of Hazardous Materials*, 2020. 399: p. 123035.

[63] Fernández-García, M. and J. Rodriguez, Metal Oxide Nanoparticles, *Encycl. Inorg. Bioinorg. Chem*, 2011: p. 1–11.

[64] Peck, M.A. and M.A. Langell, Comparison of nanoscaled and bulk NiO structural and environmental characteristics by XRD, XAFS, and XPS. *Chemistry of Materials*, 2012. 24(23): p. 4483–4490.

[65] Wang, J., et al., Preparation of NiO two-dimensional grainy films and their high-performance gas sensors for ammonia detection. *Nanoscale Research Letters*, 2015. 10: p. 1–6.

[66] Olaitan, A.D., et al., Transition metal oxide nanoparticles as surfaces for surface-assisted laser desorption/ionization mass spectrometry of asphaltenes. *Petroleum Science and Technology*, 2017. 35(19): p. 1917–1924.

[67] Kannan, K., et al., Nanostructured metal oxides and its hybrids for photocatalytic and biomedical applications. *Advances in Colloid and Interface Science*, 2020. 281: p. 102178.

[68] De Los Santos Valladares, L., et al., Characterization of Ni thin films following thermal oxidation in air. *Journal of Vacuum Science & Technology B*, 2014. 32(5).

[69] Djeddou, M., Influence de température de propriétés des couches minces d'oxyde de nickel dopé fer et élaboré par la technique spray pneumatique. *Mémoire de Magister*, Université Med Khider Biskra, 2017.

[70] Sharma, S., P. Chauhan, and S. Husain, Structural and optical properties of Mn2O3 nanoparticles its gas sensing applications. *Advanced Materials Proceedings*, 2016. 1(2): p. 220–225.

[71] Jassem, E., A. Mustafa, and N. Umran, The effect of temperature on structural and optical properties of manganese oxide nanoparticles. *Journal of Physics: Conference Series*, 2019. 1279: p. 012004.

[72] Jassal, V., et al., *Sapindus mukorossi*-mediated green synthesis of some manganese oxide nanoparticles interaction with aromatic amines. *Applied Physics A*, 2016. 122: p. 1–12.

[73] Yadav, P., A. Bhaduri, and A. Thakur, Manganese Oxide Nanoparticles: An Insight into Structure, Synthesis and Applications. *ChemBioEng Reviews*, 2023. 10.

[74] Liu, Y.-H., et al., Birnessite-type manganese dioxide nanosheets on metalorganic frameworks with high catalytic activity in ozone decomposition. *ACS Applied Nano Materials*, 2023. 6(9): p. 7794–7801.

[75] Al-Wasidi, A.S., et al., Preparation of Cr2O3, MnO2, Fe2O3, NiO, CuO, and ZnO oxides using their glycine complexes as precursors for in situ thermal decomposition. *Egyptian Journal of Chemistry*, 2020. 63(3): p. 1109–1118.

[76] Reyes, V., O. Martínez, and G. Hernández, National center for biotechnology information. Plant Breeding. Universidad Autónoma Agraria Antonio Narro, Calzada Antonio Narro, 1923.

[77] Kaczmarczyk, J., et al., Thermodynamic stability, redox properties, and reactivity of Mn3O4, Fe3O4, and Co3O4 model catalysts for N2O decomposition: resolving the origins of steady turnover. *ACS Catalysis*, 2016. 6(2): p. 1235–1246.

[78] Singh, S., et al., Optical properties of selenium quantum dots produced with laser irradiation of water suspended Se nanoparticles. *The Journal of Physical Chemistry C*, 2010. 114(41): p. 17374–17384.

[79] Pareek, V., et al., Synthesis and applications of noble metal nanoparticles: a review. *Advanced Science, Engineering and Medicine*, 2017. 9(7): p. 527–544.

[80] Thakkar, K.N., S.S. Mhatre, and R.Y. Parikh, Biological synthesis of metallic nanoparticles. *Nanomedicine: Nanotechnology, Biology and Medicine*, 2010. 6(2): p. 257–262.

[81] Ahmadisoltansaraei, K. and J. Moghaddam, Preparation of NiO nanoparticles from Ni(OH)2ůNiCO3ů4H2O precursor by mechanical activation. *International Journal of Minerals, Metallurgy, and Materials*, 2014. 21: p. 726–735.

[82] Balamurugan, S., et al., Simple and efficient way of synthesizing NiO nanoparticles by combustion followed by ball milling method. *Nanoscience and Nanotechnology Letters*, 2015. 7(2): p. 89–93.

[83] Hotovy, I., et al., NiO-based nanostructured thin films with Pt surface modification for gas detection. *Thin Solid Films*, 2006. 515(2): p. 658–661.

[84] Ukoba, K., A. Eloka-Eboka, and F. Inambao, Review of nanostructured NiO thin film deposition using the spray pyrolysis technique. *Renewable and Sustainable Energy Reviews*, 2018. 82: p. 2900–2915.

[85] Moravec, P., et al., NiO x nanoparticle synthesis by chemical vapor deposition from nickel acetylacetonate. *Materials Sciences and Applications*, 2011. 2(04): p. 258.

[86] Gondal, M., T.A. Saleh, and Q. Drmosh, Synthesis of nickel oxide nanoparticles using pulsed laser ablation in liquids and their optical characterization. *Applied Surface Science*, 2012. 258(18): p. 6982–6986.

[87] Baig, U., et al., Laser induced anchoring of nickel oxide nanoparticles on polymeric graphitic carbon nitride sheets using pulsed laser ablation for efficient water splitting under visible light. *Nanomaterials*, 2020. 10(6): p. 1098.

[88] Reguig, B., et al., Properties of NiO thin films deposited by intermittent spray pyrolysis process. *Applied Surface Science*, 2007. 253(9): p. 4330–4334.

[89] Wei, Z., et al., Characterization of NiO nanoparticles by anodic arc plasma method. *Journal of Alloys and Compounds*, 2009. 479(1-2): p. 855–858.

[90] Safa, S., et al., Hydrothermal synthesis of NiO nanostructures for photodegradation of 4-nitrophenol. *Desalination and Water Treatment*, 2016. 57(46): p. 21982–21989.

[91] Parsae, Z., Synthesis of novel amperometric urea-sensor using hybrid synthesized NiO-NPs/GO modified GCE in aqueous solution of cetrimonium bromide. *Ultrasonics Sonochemistry*, 2018. 44: p. 120–128.

[92] Qing, Z., et al., Solvothermal synthesis and photocatalytic properties of NiO ultrathin nanosheets with porous structure. *Applied Surface Science*, 2015. 328: p. 525–530.

[93] Deng, X. and Z. Chen, Preparation of nano-NiO by ammonia precipitation and reaction in solution and competitive balance. *Materials Letters*, 2004. 58(3-4): p. 276–280.

[94] Tadic, M., et al., Magnetic properties of NiO (nickel oxide) nanoparticles: Blocking temperature and Neel temperature. *Journal of Alloys and Compounds*, 2015. 647: p. 1061–1068.

[95] Han, D., et al., Synthesis and size control of NiO nanoparticles by water-in-oil microemulsion. *Powder Technology*, 2004. 147(1-3): p. 113–116.

[96] Zorkipli, N.N.M., N.H.M. Kaus, and A.A. Mohamad, Synthesis of NiO nanoparticles through sol-gel method. *Procedia Chemistry*, 2016. 19: p. 626–631.

[97] Nathan, T., et al., Nanostructured NiO for electrochemical capacitors: synthesis and electrochemical properties. *Journal of Solid State Electrochemistry*, 2008. 12: p. 1003–1009.

[98] Abdallah, A., H. Basma, and R. Awad, Preparation, characterization, and application of nickel oxide nanoparticles in glucose and lactose biosensors. *Mod. Appl. Sci.*, 2019. 13(6): p. 99.

[99] Srikesh, G. and A.S. Nesaraj, Synthesis and characterization of phase pure NiO nanoparticles via the combustion route using different organic fuels for electrochemical capacitor applications. *Journal of Electrochemical Science and Technology*, 2015. 6(1): p. 16–25.

[100] Ezhilarasi, A.A., et al., Green synthesis of NiO nanoparticles using *Aegle marmelos* leaf extract for the evaluation of in-vitro cytotoxicity, antibacterial and photocatalytic properties. *Journal of Photochemistry and Photobiology B: Biology*, 2018. 180: p. 39–50.

[101] Abbasi, B.A., et al., Plant-mediated synthesis of nickel oxide nanoparticles (NiO) via *Geranium wallichianum*: Characterization and different biological applications. *Materials Research Express*, 2019. 6(8): p. 0850a7.

[102] Yuvakkumar, R., et al., Rambutan (*Nephelium lappaceum* L.) peel extract assisted biomimetic synthesis of nickel oxide nanocrystals. *Materials Letters*, 2014. 128: p. 170–174.

[103] Ezhilarasi, A.A., et al., Green synthesis of NiO nanoparticles using *Moringa oleifera* extract and their biomedical applications: Cytotoxicity effect of nanoparticles against HT-29 cancer cells. *Journal of Photochemistry and Photobiology B: Biology*, 2016. 164: p. 352–360.

[104] Helan, V., et al., Neem leaves mediated preparation of NiO nanoparticles and its magnetization, coercivity and antibacterial analysis. *Results in Physics*, 2016. 6: p. 712–718.

[105] Kganyago, P., et al., Synthesis of NiO nanoparticles via a green route using *Monsonia burkeana*: the physical and biological properties. *Journal of Photochemistry and Photobiology B: Biology*, 2018. 182: p. 18–26.

[106] Hoseinpour, V. and N. Ghaemi, Green synthesis of manganese nanoparticles: Applications and future perspectiveA review. *Journal of Photochemistry and Photobiology B: Biology*, 2018. 189: p. 234–243.

[107] Khan, S.A., et al., Green synthesis of MnO nanoparticles using *Abutilon indicum* leaf extract for biological, photocatalytic, and adsorption activities. *Biomolecules*, 2020. 10(5): p. 785.

[108] Lu, H., et al., Biogenic synthesis of MnO2 nanoparticles with leaf extract of *Viola betonicifolia* for enhanced antioxidant, antimicrobial, cytotoxic, and biocompatible applications. *Frontiers in Microbiology*, 2021. 12: p. 761084.

[109] Khezeli, T., A. Daneshfar, and F. Kardani, In-situ functionalization of MnO2 nanoparticles by natural tea polyphenols: a greener sorbent for dispersive solid-phase extraction of parabens from wastewater and cosmetics. *Microchemical Journal*, 2023. 190: p. 108751.

[110] Munir, R., et al., Biosynthesis of *Leucaena leucocephala* leaf mediated ZnO, CuO, MnO2, and MgO based nano-adsorbents for Reactive Golden Yellow-145 (RY-145) and Direct Red-31 (DR-31) dye removal from textile wastewater to reuse in agricultural purpose. *Separation and Purification Technology*, 2023. 306: p. 122527.

[111] Rahmat, M., et al., Plant-assisted synthesis and characterization of MnO2 nanoparticles for removal of crystal violet dye: an environmental remedial approach. *Environmental Science and Pollution Research*, 2023. 30(20): p. 57587–57598.

[112] Diallo, A., et al., Green synthesis of single phase hausmannite Mn3O4 nanoparticles via *Aspalathus linearis* natural extract. *SN Applied Sciences*, 2021. 3: p. 1–11.

[113] Nair Sreekala, G., F. Abdullakutty, and B. Beena, Green synthesis, characterization, and photocatalytic degradation efficiency of Trimanganese Tetroxide nanoparticle. *International Journal of Nano Dimension*, 2019. 10(4): p. 400–409.

[114] Prasad, A.S., Green synthesis of nanocrystalline manganese (II, III) oxide. *Materials Science in Semiconductor Processing*, 2017. 71: p. 342–347.

[115] Thanigaivel, A., et al., Chemicals isolated from *Justicia adhatoda* Linn reduce fitness of the mosquito, *Aedes aegypti* L. *Archives of Insect Biochemistry and Physiology*, 2017. 94(4): p. e21384.

[116] Sharma, J.K., et al., *Azadirachta indica* plant-assisted green synthesis of Mn3O4 nanoparticles: Excellent thermal catalytic performance and chemical sensing behavior. *Journal of Colloid and Interface Science*, 2016. 472: p. 220–228.

[117] Van Tran, T., et al., Green synthesis of Mn3O4 nanoparticles using *Costus woodsonii* flowers extract for effective removal of malachite green dye. *Environmental Research*, 2022. 214: p. 113925.

[118] Sumantha, H., et al., Green synthesis and characterization of Mn3O4 nanoparticles for photocatalytic and supercapacitors. *Ionics*, 2023. 29(2): p. 733–749.

[119] Anand, G.T., et al., Structural and optical properties of nickel oxide nanoparticles: Investigation of antimicrobial applications. *Surfaces and Interfaces*, 2020. 18: p. 100460.

[120] Morozov, Y.G., O. Belousova, and M. Kuznetsov, Preparation of nickel nanoparticles for catalytic applications. *Inorganic Materials*, 2011. 47: p. 36–40.

[121] Wu, X., et al., Nickel nanoparticles prepared by hydrazine hydrate reduction and their application in supercapacitor. *Powder Technology*, 2012. 224: p. 162–167.

[122] Pandian, C.J., R. Palanivel, and S. Dhananasekaran, Green synthesis of nickel nanoparticles using *Ocimum sanctum* and their application in dye and pollutant adsorption. *Chinese Journal of Chemical Engineering*, 2015. 23(8): p. 1307–1315.

[123] Ahmed, A., D.R. Yadav, and Y.S. Lee, Applications of nickel nanoparticles for control of Fusarium wilt on lettuce and tomato. *Int. J. Innov. Res. Sci. Eng. Technol*, 2016. 5(5): p. 7378–7385.

[124] Sana, S.S., et al., Biogenesis and application of nickel nanoparticles: a review. *Current Pharmaceutical Biotechnology*, 2021. 22(6): p. 808–822.

[125] Moavi, J., F. Buazar, and M.H. Sayahi, Algal magnetic nickel oxide nanocatalyst in accelerated synthesis of pyridopyrimidine derivatives. *Scientific Reports*, 2021. 11(1): p. 6296.

[126] Rossi, L.M., A.D. Quach, and Z. Rosenzweig, Glucose oxidasemagnetite nanoparticle bioconjugate for glucose sensing. *Analytical and Bioanalytical Chemistry*, 2004. 380: p. 606–613.

[127] Liu, X., et al., A review on the synthesis of manganese oxide nanomaterials and their applications on lithiumion batteries. *Journal of Nanomaterials*, 2013. 2013(1): p. 736375.

[128] Sahib, R.S. and J.A. Naser, Preparation, characterization and surface area properties of manganese oxide nanoparticles. *Annals of the Romanian Society for Cell Biology*, 2021: p. 2962–2969.

[129] Ociski, D., et al., Water treatment residuals containing iron and manganese oxides for arsenic removal from waterCharacterization of physicochemical properties and adsorption studies. *Chemical Engineering Journal*, 2016. 294: p. 210–221.

[130] Saini, S. and S. Sharma, *Helianthus annuus* (Asteracea): a review. *International Journal of Pharma Professionals Research*, 2011. 2(4): p. 465–470.

[131] De'Nobili, M.D., et al., Sunflower (*Helianthus annuus* L.) seed hull waste: composition, antioxidant activity, and filler performance in pectin-based film composites. *Frontiers in Nutrition*, 2021. 8: p. 777214.

[132] Dwivedi, A. and G. Sharma, A review on Heliotropism plant: *Helianthus annuus* L. *The Journal of Phytopharmacology*, 2014. 3(2): p. 149–155.

[133] Pal, D., Sunflower (*Helianthus annuus* L.) seeds in health and nutrition, in *Nuts and Seeds in Health and Disease Prevention*, 2011, Elsevier. p. 1097–1105.

[134] Wojtaszek, J. and C. Maier, A microscopic review of the sunflower and honeybee mutualistic relationship. 2014.

[135] Subashini, R. and S.U. Rakshitha, Phytochemical screening, antimicrobial activity and in vitro antioxidant investigation of methanolic extract of seeds from *Helianthus annuus* L. *Chem Sci Rev Lett*, 2012. 1(1): p. 30–34.

[136] Kamal, J., Quantification of alkaloids, phenols and flavonoids in sunflower (*Helianthus annuus* L.). *African Journal of Biotechnology*, 2011. 10(16): p. 3149–3151.

[137] Adeleke, B.S. and O.O. Babalola, Oilseed crop sunflower (*Helianthus annuus*) as a source of food: Nutritional and health benefits. *Food Science & Nutrition*, 2020. 8(9): p. 4666–4684.

[138] Nwokolo, E. and J. Smartt, Food and feed from legumes and oilseeds. 1996.

[139] Crum, C., J. Prescott, and P. Christensen, Genetic approaches to increased nutritional value in oilseed meal. 1993.

[140] Singh, S., et al., Applications of nanoparticles in wastewater treatment. *Nanobiotechnology in Bioformulations*, 2019: p. 395–418.

[141] Karfa, P., K.C. Majhi, and R. Madhuri, Bringing awareness to the darker side of nanoparticles. *The ELSI Handbook of Nanotechnology: Risk, Safety, ELSI and Commercialization*, 2020: p. 135–163.

[142] Ali, A., K. Saeed, and F. Mabood, Removal of chromium (VI) from aqueous medium using chemically modified banana peels as efficient low-cost adsorbent. *Alexandria Engineering Journal*, 2016. 55(3): p. 2933–2942.

[143] Rather, M.Y. and S. Sundarapandian, Facile green synthesis of copper oxide nanoparticles and their rhodamine-b dye adsorption property. *Journal of Cluster Science*, 2022. 33(3): p. 925–933.

[144] Odumbe, E., S. Murunga, and J. Ndiiri, Heavy metals in wastewater effluent: Causes, effects, and removal technologies. *Trace Metals in the Environment*, 2023.

[145] Akpor, O.B., G.O. Ohiobor, and D. Olaolu, Heavy metal pollutants in wastewater effluents: sources, effects and remediation. *Advances in Bioscience and Bioengineering*, 2014. 2(4): p. 37–43.

[146] Ince, M. and O.K. Ince, An overview of adsorption technique for heavy metal removal from water/wastewater: a critical review. *International Journal of Pure and Applied Sciences*, 2017. 3(2): p. 10–19.

[147] Abu-El-Halawa, R. and S.A. Zabin, Removal efficiency of Pb, Cd, Cu and Zn from polluted water using dithiocarbamate ligands. *Journal of Taibah University for Science*, 2017. 11(1): p. 57–65.

[148] Barakat, M., New trends in removing heavy metals from industrial wastewater. *Arabian Journal of Chemistry*, 2011. 4(4): p. 361–377.

[149] Hegazi, H.A., Removal of heavy metals from wastewater using agricultural and industrial wastes as adsorbents. *HBRC Journal*, 2013. 9(3): p. 276–282.

[150] Duan, C., et al., Removal of heavy metals from aqueous solution using carbon-based adsorbents: A review. *Journal of Water Process Engineering*, 2020. 37: p. 101339.

[151] Zou, Y., et al., Environmental remediation and application of nanoscale zero-valent iron and its composites for the removal of heavy metal ions: a review. *Environmental Science & Technology*, 2016. 50(14): p. 7290–7304.

[152] Borba, C., et al., Removal of nickel (II) ions from aqueous solution by biosorption in a fixed bed column: experimental and theoretical breakthrough curves. *Biochemical Engineering Journal*, 2006. 30(2): p. 184–191.

[153] Demiral, ., C. Samdan, and H. Demiral, Enrichment of the surface functional groups of activated carbon by modification method. *Surfaces and Interfaces*, 2021. 22: p. 100873.

[154] Qasem, N.A., R.H. Mohammed, and D.U. Lawal, Removal of heavy metal ions from wastewater: A comprehensive and critical review. *NPJ Clean Water*, 2021. 4(1): p. 1–15.

[155] Upadhyay, U., et al., Recent advances in heavy metal removal by chitosan based adsorbents. *Carbohydrate Polymers*, 2021. 251: p. 117000.

[156] Vardhan, K.H., P.S. Kumar, and R.C. Panda, A review on heavy metal pollution, toxicity and remedial measures: Current trends and future perspectives. *Journal of Molecular Liquids*, 2019. 290: p. 111197.

[157] Nishat, A., et al., Wastewater treatment: a short assessment on available techniques. *Alexandria Engineering Journal*, 2023. 76: p. 505–516.

[158] Tripathi, A. and M.R. Ranjan, Heavy metal removal from wastewater using low cost adsorbents. *J Bioremed Biodeg*, 2015. 6(6): p. 315.

[159] Da'na, E., Adsorption of heavy metals on functionalized-mesoporous silica: A review. *Microporous and Mesoporous Materials*, 2017. 247: p. 145–157.

[160] Yaashikaa, P., et al., Modelling on the removal of Cr (VI) ions from aquatic system using mixed biosorbent (*Pseudomonas stutzeri* and acid treated Banyan tree bark). *Journal of Molecular Liquids*, 2019. 276: p. 362–370.

[161] Sigworth, E. and S. Smith, Adsorption of inorganic compounds by activated carbon. *JournalAmerican Water Works Association*, 1972. 64(6): p. 386–391.

[162] Kaveeshwar, A.R., et al., Adsorption properties and mechanism of barium (II) and strontium (II) removal from fracking wastewater using pecan shell based activated carbon. *Journal of Cleaner Production*, 2018. 193: p. 1–13.

[163] Dbrowski, A., Adsorptionfrom theory to practice. *Advances in Colloid and Interface Science*, 2001. 93(1-3): p. 135–224.

[164] Yagub, M.T., et al., Dye and its removal from aqueous solution by adsorption: a review. *Advances in Colloid and Interface Science*, 2014. 209: p. 172–184.

[165] Fei, N., B. Sauter, and D. Gillingham, The p K a of Brønsted acids controls their reactivity with diazo compounds. *Chemical Communications*, 2016. 52(47): p. 7501–7504.

[166] Mehta, S.L., N. Manhas, and R. Raghubir, Molecular targets in cerebral ischemia for developing novel therapeutics. *Brain Research Reviews*, 2007. 54(1): p. 34–66.

[167] Pashin, J.C., Coal as a petroleum source rock and reservoir rock, in *Applied Coal Petrology*, 2008, Elsevier. p. 227–262.

[168] Alaqarbeh, M., Adsorption phenomena: definition, mechanisms, and adsorption types: short review. *RHAZES: Green and Applied Chemistry*, 2021. 13: p. 43–51.

[169] Daniel, S., The adsorption on metal surfaces of long chain polar compounds from hydrocarbon solutions. *Transactions of the Faraday Society*, 1951. 47: p. 1345–1359.

[170] Sotelo, J.L., et al., Study of natural clay adsorbent sepiolite for the removal of caffeine from aqueous solutions: batch and fixed-bed column operation. *Water, Air, & Soil Pollution*, 2013. 224: p. 1–15.

[171] Naoufal, B., et al., Adsorption of nutrients using low-cost adsorbents from agricultural waste and by-productsreview. *Progress in Agricultural Engineering Sciences*, 2018. 14(1): p. 1–30.

[172] Lim, A.P. and A.Z. Aris, A review on economically adsorbents on heavy metals removal in water and wastewater. *Reviews in Environmental Science and Bio/Technology*, 2014. 13: p. 163–181.

[173] Huang, W. and Z.-m. Liu, Biosorption of Cd (II)/Pb (II) from aqueous solution by biosurfactant-producing bacteria: isotherm kinetic characteristic and mechanism studies. *Colloids and Surfaces B: Biointerfaces*, 2013. 105: p. 113–119.

[174] Ugwu, E., et al., Adsorption mechanisms for heavy metal removal using low cost adsorbents: A review. in *IOP Conference Series: Earth and Environmental Science*, 2020. IOP Publishing.

[175] Wang, S., L. Li, and Z. Zhu, Solid-state conversion of fly ash to effective adsorbents for Cu removal from wastewater. *Journal of Hazardous Materials*, 2007. 139(2): p. 254–259.

[176] Kumar, A., et al., Intensive insight into the enhanced utilization of rice husk ash: abatement of rice mill wastewater and recovery of silica as a value added product. *Ecological Engineering*, 2016. 91: p. 270–281.

[177] Ariffin, N., et al., Review on adsorption of heavy metal in wastewater by using geopolymer. in *MATEC Web of Conferences*, 2017. EDP Sciences.

[178] Xu, J., et al., A review of functionalized carbon nanotubes and graphene for heavy metal adsorption from water: Preparation, application, and mechanism. *Chemosphere*, 2018. 195: p. 351–364.

[179] Alasadi, A., F. Khaili, and A. Awwad, Adsorption of Cu (II), Ni (II) and Zn (II) ions by nano kaolinite: Thermodynamics and kinetics studies. *Chemistry International*, 2019. 5(4): p. 258–26.

[180] Babarinde, A. and G.O. Onyiaocha, Equilibrium sorption of divalent metal ions onto groundnut (*Arachis hypogaea*) shell: kinetics, isotherm and thermodynamics. *Chem. Int*, 2016. 2(3): p. 37–46.

[181] Azizian, S., Kinetic models of sorption: a theoretical analysis. *Journal of Colloid and Interface Science*, 2004. 276(1): p. 47–52.

[182] Priyantha, N., A. Navaratne, and T. Kulasooriya, Investigation on adsorption kinetics of heavy metals by rice husk. *Journal of the National Science Foundation of Sri Lanka*, 2018. 46(2): p. 125–141.

[183] Ho, Y.-S. and G. McKay, Pseudo-second order model for sorption processes. *Process Biochemistry*, 1999. 34(5): p. 451–465.

[184] Fierro, V., et al., Adsorption of phenol onto activated carbons having different textural and surface properties. *Microporous and Mesoporous Materials*, 2008. 111(1-3): p. 276–284.

[185] Weber Jr, W.J. and J.C. Morris, Kinetics of adsorption on carbon from solution. *Journal of the Sanitary Engineering Division*, 1963. 89(2): p. 31–59.

[186] Luukkonen, T., et al., Metakaolin geopolymer characterization and application for ammonium removal from model solutions and landfill leachate. *Applied Clay Science*, 2016. 119: p. 266–276.

[187] Giles, C.H., D. Smith, and A. Huitson, A general treatment and classification of the solute adsorption isotherm. I. Theoretical. *Journal of Colloid and Interface Science*, 1974. 47(3): p. 755–765.

[188] Limousin, G., et al., Sorption isotherms: A review on physical bases, modeling and measurement. *Applied Geochemistry*, 2007. 22(2): p. 249–275.

[189] Errais, E., Réactivité de surface d'argiles naturelles: Etude de l'adsorption de colorants anioniques. *Theses.fr*, 2011, Strasbourg.

[190] Freundlich, H., Über die adsorption in lösungen. *Zeitschrift für Physikalische Chemie*, 1907. 57(1): p. 385–470.

[191] Tran, H.N., et al., Thermodynamic parameters of liquidphase adsorption process calculated from different equilibrium constants related to adsorption isotherms: A comparison study. *Journal of Environmental Chemical Engineering*, 2021. 9(6): p. 106674.

[192] Faust, S.D. and O.M. Aly, Adsorption processes for water treatment. 2013: Elsevier.

[193] Ayawei, N., et al., Synthesis, characterization and application of Mg/Al layered double hydroxide for the degradation of congo red in aqueous solution. *Open Journal of Physical Chemistry*, 2015. 5(3): p. 56–70.

[194] Özacar, M. and .A. engil, Equilibrium data and process design for adsorption of disperse dyes onto alunite. *Environmental Geology*, 2004. 45: p. 762–768.

[195] Shaker, M.A., Dynamics and thermodynamics of toxic metals adsorption onto soil-extracted humic acid. *Chemosphere*, 2014. 111: p. 587–595.

[196] Özer, A., F. Tümen, and M. Bildik, Cr (III) removal from aqueous solutions by depectinated sugar beet pulp. *Environmental Technology*, 1997. 18(9): p. 893–901.

[197] Gorzin, F. and M. Bahri Rasht Abadi, Adsorption of Cr (VI) from aqueous solution by adsorbent prepared from paper mill sludge: Kinetics and thermodynamics studies. *Adsorption Science & Technology*, 2018. 36(1-2): p. 149–169.

[198] An, F.-Q., et al., Adsorption of heavy metal ions by iminodiacetic acid functionalized D301 resin: Kinetics, isotherms and thermodynamics. *Reactive and Functional Polymers*, 2017. 118: p. 42–50.

[199] Saini, S., J.K. Katnoria, and I. Kaur, A comparative study for removal of cadmium (II) ions using unmodified and NTA-modified *Dendrocalamus strictus* charcoal powder. *Journal of Environmental Health Science and Engineering*, 2019. 17: p. 259–272.

[200] Ghidan, A.Y., T.M. Al-Antary, and A.M. Awwad, Green synthesis of copper oxide nanoparticles using *Punica granatum* peels extract: Effect on green peach Aphid. *Environmental Nanotechnology, Monitoring & Management*, 2016. 6: p. 95–98.

[201] ZENKHRI, L. and S. BOUDJEMAA, Synthetic and natural particles for the treatment of polluted water Synthesis, identification and application, Université Kasdi Merbah Ouargla.

[202] Tauc, J. and A. Menth, States in the gap. Journal of non-crystalline solids, 1972, 8, 569-585.

[203] Mittal, A.K., Y. Chisti, and U.C. Banerjee, Synthesis of metallic nanoparticles using plant extracts. Biotechnology advances, 2013, 31(2), 346-356.

[204] Raveendran, P., J. Fu, and S.L. Wallen, Completely green synthesis and stabilization of metal nanoparticles. Journal of the American Chemical Society, 2003, 125(46), 13940-13941.

[205] Abdeldaiem, M. and G. Hoda, Evaluation of antioxidant activity of ethanolic extract from irradiated sunflower (Helianthus Annuus L.) seeds hull. Evaluation, 2014, 4(1).

[206] Abuzeid, H.M., et al., Green Synthesis of Metal and Metal Oxide Nanoparticles for Recent Applications. Crystals, 2023, 13, 1576.

[207] Dhaouadi, H., et al., Mn3O4 nanoparticles: synthesis, characterization, and dielectric properties. International Scholarly Research Notices, 2012, 2012, 706398.

[208] Adeyemi, J.O., D.C. Onwudiwe, and A.O. Oyedeji, In vitro -glucosidase enzyme inhibition and anti-inflammatory studies of Mn3O4 nanoparticles mediated using extract of dalbergiella welwitschia. Results in Chemistry, 2022, 4, 100497.

[209] Walls, B., et al., Nanodomain structure of single crystalline nickel oxide. Scientific Reports, 2021, 11, 3496.

[210] Shah, A., et al., Histopathological and hematological investigations of mice model inoculated with nickel oxide nanoparticles and bacterial pathogens: In-vitro and in-vivo antibacterial studies. Journal of King Saud University - Science, 2023, 35(1), 102456.

[211] Prabhu, S., D. Thangadurai, and P. Bharathy, Green-based Biosynthesis of Zinc Oxide Nanoparticles Using Clitoria Ternatea Flower Extract and Its Antibacterial Activity. Nano Biomedicine and Engineering, 2021, 13.

[212] Haines, J., J. Léger, and S. Hoyau, Second-order rutile-type to CaCl2-type phase transition in -MnO2 at high pressure. Journal of Physics and Chemistry of Solids, 1995, 56(7), 965-973.

[213] Teli, A.M., et al., Effect of annealing temperature on charge storage kinetics of an electrospun deposited manganese oxide supercapacitor. Applied Surface Science, 2020, 511, 145466.

[214] Reddy, I.N., et al., A study of coral reef-like tetragonal Mn3O4 nanostructure photoelectrode for photoelectrochemical water splitting under visible irradiation. Journal of Electroanalytical Chemistry, 2020, 874, 114488.

[215] ahin, B., R. Aydin, and H. Cetin, Tuning the morphological, structural, optical and dielectric properties of hausmannite (Mn3O4) films by doping heavy metal lead. Superlattices and Microstructures, 2020, 143, 106546.

[216] Li, N., et al., Efficient removal of chromium from water by Mn3O4@ZnO/Mn3O4 composite under simulated sunlight irradiation: synergy of photocatalytic reduction and adsorption. Applied Catalysis B: Environmental, 2017, 214, 126-136.

[217] Raj, B.G.S., et al., Synthesis of Mn3O4 nanoparticles via chemical precipitation approach for supercapacitor application. Journal of Alloys and Compounds, 2015, 636, 234-240.

[218] Fadhel, M.H., A.H. Al Khazraji, and A.H. Fahmi, Eco-Friendly Method for Synthesis of Mn3O4 Nanoparticles and Their Characterization. Egyptian Journal of Chemistry, 2023, 66(7), 113-117.

[219] Baig, M.K., et al., Magnetic Behavior of Ni/NiO CoreShell Nanoparticles under Electromagnetic Waves for OilWater Interfacial Tension Reduction. J. Mater. Eng. Perform., 2019, 28(9), 5882-5889.

[220] Sabouri, Z., et al., Plant-based synthesis of NiO nanoparticles using salvia macrosiphon Boiss extract and examination of their water treatment. Rare Metals, 2020, 39(10), 1134-1144.

[221] Manjula, R., et al., Green synthesis and characterization of manganese oxide nanoparticles from Gardenia resinifera leaves. Materials Today: Proceedings, 2020, 26, 3559-3563.

[222] Gosens, I., et al., Impact of agglomeration state of nano-and submicron sized gold particles on pulmonary inflammation. Particle and Fibre Toxicology, 2010, 7, 1-11.

[223] Sayyed, S.G., et al., Investigation of electrochemical performance and stability of electrodeposited Mn3O4 thin films in different aqueous electrolytes for its application in flexible supercapacitors. Journal of Energy Storage, 2021, 33, 102076.

[224] Karpagavinayagam, P., A. Emi Princess Prasanna, and C. Vedhi, Eco-friendly synthesis of nickel oxide nanoparticles using Avicennia Marina leaf extract: Morphological characterization and electrochemical application. Materials Today: Proceedings, 2022, 48, 136-142.

[225] Prabhu, S., et al., Synthesis and characterization of nickel oxide nanoparticles using Clitoria ternatea flower extract: Photocatalytic dye degradation under sunlight and antibacterial activity applications. Results in Chemistry, 2022, 4, 100285.

[226] Angel Ezhilarasi, A., et al., Green synthesis of NiO nanoparticles using Aegle marmelos leaf extract for the evaluation of in-vitro cytotoxicity, antibacterial and photocatalytic properties. J. Photochem. Photobiol, 2018, 180, 39-50.

[227] Din, M., et al., Single step green synthesis of nickel and nickel oxide nanoparticles from Hordeum vulgare for photocatalytic degradation of methylene blue dye. INORG NANO-MET CHEM., 2020, 50, 1-6.

[228] Sharma, S., P. Chauhan, and S. Husain, Structural and optical properties of Mn2O3 nanoparticles its gas sensing applications. Adv. Mater. Proc., 2016.

[229] Pinaud, B.A., et al., Thin films of sodium birnessite-type MnO2: optical properties, electronic band structure, and solar photoelectrochemistry. The Journal of Physical Chemistry C, 2011, 115(23), 11830-11838.

[230] Chen, X., et al., Green synthesis of gold nanoparticles using carrageenan oligosaccharide and their in vitro antitumor activity. Marine Drugs, 2018, 16(8), 277.

[231] Fritzsche, H., The origin of reversible and irreversible photostructural changes in chalcogenide glasses. Philosophical Magazine B, 1993, 68(4), 561-572.

[232] Dubal, D., et al., A novel chemical synthesis and characterization of Mn3O4 thin films for supercapacitor application. Applied Surface Science, 2010, 256(14), 4411-4416.

[233] Hosny, N.M. and A. Dahshan, Facile synthesis and optical band gap calculation of Mn3O4 nanoparticles. Materials Chemistry and Physics, 2012, 137(2), 637-643.

[234] Hayoun, B., et al., Equilibrium Study, Modeling and Optimization of Model Drug Adsorption Process by Sunflower Seed Shells. Applied Sciences, 2020, 10, 3271.

[235] Olajire, A.A. and A.A. Mohammed, Green synthesis of nickel oxide nanoparticles and studies of their photocatalytic activity in degradation of polyethylene films. Advanced Powder Technology, 2020, 31(1), 211-218.

[236] Oliveira, R.N., et al., FTIR analysis and quantification of phenols and flavonoids of five commercially available plants extracts used in wound healing. Matéria (Rio de Janeiro), 2016, 21(03), 767-779.

[237] Hayoun, B., et al., Equilibrium study, modeling and optimization of model drug adsorption process by sunflower seed shells. Applied Sciences, 2020, 10(9), 3271.

[238] Parikh, S.J. and J. Chorover, FTIR spectroscopic study of biogenic Mn-oxide formation by Pseudomonas putida GB-1. Geomicrobiology Journal, 2005, 22(5), 207-218.

[239] Perachiselvi, M., et al., Synthesis and characterization of Mn3O4 nanoparticles for biological studies. Appl. Ecol. Environ. Sci, 2020, 8(5), 273-277.

[240] Mohamed, S.K., A.M. Elhgrasi, and O.I. Ali, Facile synthesis of mesoporous nano Ni/NiO and its synergistic role as super adsorbent and photocatalyst under sunlight irradiation. Environmental Science and Pollution Research, 2022, 29(43), 64792-64806.

[241] Hanifehpour, Y., et al., The electrochemical performance and catalytic properties of Ytterbium substitution on Manganese oxide nanoparticles: BET study; preparation and characterization. Journal of Materials Science: Materials in Electronics, 2019, 30, 18897-18909.

[242] Awual, M.R. and M.M. Hasan, Novel conjugate adsorbent for visual detection and removal of toxic lead(II) ions from water. MICROP M M, 2014, 196, 261-269.

[243] Krishna, Y.V.S., G. Sandhya, and R.R. Babu, Removal of heavy metals Pb(II), Cd(II) and Cu(II) from waste waters using synthesized chromium doped nickel oxide nanoparticles. Bulletin of the Chemical Society of Ethiopia, 2018, 32, 225.

[244] Tang, C.-Y., et al., Tannic acid functionalized graphene hydrogel for organic dye adsorption. Ecotoxicology and Environmental Safety, 2018, 165, 299-306.

[245] Khoso, W.A., et al., Synthesis, characterization and heavy metal removal efficiency of nickel ferrite nanoparticles (NFNs). Scientific Reports, 2021, 11, 3790.

[246] Semerjian, L., Removal of heavy metals (Cu, Pb) from aqueous solutions using pine (Pinus halepensis) sawdust: Equilibrium, kinetic, and thermodynamic studies. Environmental Technology Innovation, 2018, 12, 91-103.

[247] Khulbe, K. and T. Matsuura, Removal of heavy metals and pollutants by membrane adsorption techniques. Applied Water Science, 2018, 8, 1-30.

[248] Keochaiyom, B., et al., Synthesis and application of magnetic chlorapatite nanoparticles for zinc (II), cadmium (II) and lead (II) removal from water solutions. Journal of Colloid and Interface Science, 2017, 505, 824-835.

[249] Abdolali, A., et al., A breakthrough biosorbent in removing heavy metals: Equilibrium, kinetic, thermodynamic and mechanism analyses in a lab-scale study. Sci. Total Environ, 2016, 542, 603-611.

[250] Jayarambabu, N., Germination and Growth Characteristics of Mungbean Seeds (Vigna radiata L.) affected by Synthesized Zinc Oxide Nanoparticles. International Journal of Current Engineering and Technology, 2014, 4, 5.

[251] Dubey, R., J. Bajpai, and A. Bajpai, Chitosan-alginate nanoparticles (CANPs) as potential nanosorbent for removal of Hg (II) ions. Environmental Nanotechnology, Monitoring Management, 2016, 6, 32-44.

[252] Wadhawan, S., et al., Role of nanomaterials as adsorbents in heavy metal ion removal from waste water: A review. Journal of Water Process Engineering, 2020, 33, 101038.

[253] Al-Mur, B.A., Green zinc oxide (ZnO) nanoparticle synthesis using mangrove leaf extract from Avicenna marina: properties and application for the removal of toxic metal ions (Cd2+ and Pb2+). Water, 2023, 15(3), 455.

[254] Mahmoud, A.E.D., Graphene-based nanomaterials for the removal of organic pollutants: Insights into linear versus nonlinear mathematical models. Journal of Environmental Management, 2020, 270, 110911.

[255] Mustapha, S., et al., Adsorption isotherm, kinetic and thermodynamic studies for the removal of Pb (II), Cd (II), Zn (II) and Cu (II) ions from aqueous solutions using Albizia lebbeck pods. Applied Water Science, 2019, 9, 1-11.

[256] Sheela, T., et al., Kinetics and thermodynamics studies on the adsorption of Zn (II), Cd (II) and Hg (II) from aqueous solution using zinc oxide nanoparticles. Powder Technology, 2012, 217, 163-170.

[257] Naiya, T., A. Bhattacharya, and S. Das, Removal of Cd (II) from aqueous solutions using clarified sludge. Journal of Colloid and Interface Science, 2008, 325(1), 48-56.

[258] Khoshhesab, Z.M., Z. Hooshyar, and M. Sarfaraz, Removal of Pb (II) from aqueous solutions by NiO nanoparticles. Synthesis and Reactivity in Inorganic, Metal-Organic, and Nano-Metal Chemistry, 2011, 41(8), 1046-1051.

[259] Ferenji, A.E., et al., Biogenic mediated green synthesis of NiO nanoparticles for adsorptive removal of lead from aqueous solution. Heliyon, 2024, 10(11).

[260] Uogint, I., G. Lujanien, and K. Maeika, Study of Cu (II), Co (II), Ni (II) and Pb (II) removal from aqueous solutions using magnetic Prussian blue nano-sorbent. Journal of Hazardous Materials, 2019, 369, 226-235.

[261] Kabiri, S., et al., Graphene-diatom silica aerogels for efficient removal of mercury ions from water. ACS Applied Materials Interfaces, 2015, 7(22), 11815-11823.

[262] Abdollahi, B., et al., Simultaneous photodegradation of acid orange 7 and removal of Pb 2+ from polluted water using reusable clinoptiloliteTiO2 nanocomposite. Research on Chemical Intermediates, 2018, 44, 1505-1521.

[263] Lin, Z., et al., Simultaneous removal of Pb (II) and rifampicin from wastewater by iron nanoparticles synthesized by a tea extract. Journal of Cleaner Production, 2020, 242, 118476.

[264] Zhang, W., et al., A facile strategy for fabrication of nano-ZnO/yeast composites and their adsorption mechanism towards lead (II) ions. Applied Surface Science, 2016, 378, 196-206.

[265] El-Sayed, G.O., H.A. Dessouki, and S. Ibrahiem, Removal of Zn (II), Cd (II) and Mn (II) from aqueous solutions by adsorption on maize stalks. The Malaysian Journal of Analytical Sciences, 2011, 15(1), 8-21.

Scientific publications

Articles

- **Removal of heavy metals lead and copper ions from wastewater using green synthesized MnO_2/Mn_2O_3 nanoparticles**, April 3, 2025

Digest Journal of Nanomaterials and Biostructures Vol. 20, No. 2, April - June 2025, p. 395 - 408

Removal of heavy metals lead and copper ions from waste water using green synthesized MnO_2/Mn_2O_3 nanoparticles

I. Aouadj [a], H. Zerrouki [a], L. Zenkhri [a], M. S. Nedjimi [a,*], M. L. Belfar [a], S. Tlili [b], K. Mokadem [a]
[a] *VPRS Laboratory, Faculty of Mathematics & Matter Sciences University of Kasdi Merbah, B.P. 511, 30000, Ouargla, Algeria.*
[b] *LARENZA Laboratory, Kasdi Merbah Ouargla University, 30000, Ouargla, Algeria*

The current study examined the removal of lead and copper ions from aqueous solutions using a variety of experimental techniques by producing manganese oxide sorbent nanoparticles (MnO_2/Mn_2O_3-NPs) from a sunflower seed husk extract (Helianthus annuus). Key factors that affected the adsorption process were the pH level, contact time, starting metal ion concentration, and dose of the nanoadsorbent. Numerousanalytical methodswere employed to confirm the environmentally friendly manufacturing of MnO_2/Mn_2O_3-NPs.According to the data, the MnO_2/Mn_2O_3 -NP had an average size of roughly 26.93 nm.The adsorption reaction rate was analyzed by comparing pseudo-first- and pseudo-second-rate models.According to the recorded data, lead and copper ions adsorption response on the MnO_2/Mn_2O_3-NPs agreed on the paradigm of pseudo-second order. Langmuir and Freundlich's models assessed lead and copper sorption onto the absorbed substance.Considering the parameters that each model yields, the Langmuir isotherms emerge as the favoured choice for the adsorption of $Pb^{2+}$and Cu^{2+}ions on $MnO_2/Mn2O_3$ nanoparticles. MnO_2/Mn_2O_3-NPs show promise as an adsorbent material to remove heavy metals from water solutions.

(Received January 1, 2025; Accepted April 3, 2025)

Keywords: Manganese oxide nanoparticles, Green synthesis, Adsorption, Heavy metals, Kinetics model, Isotherm model

- **Green synthesis of nanoparticles and their characterization**, May 13, 2023

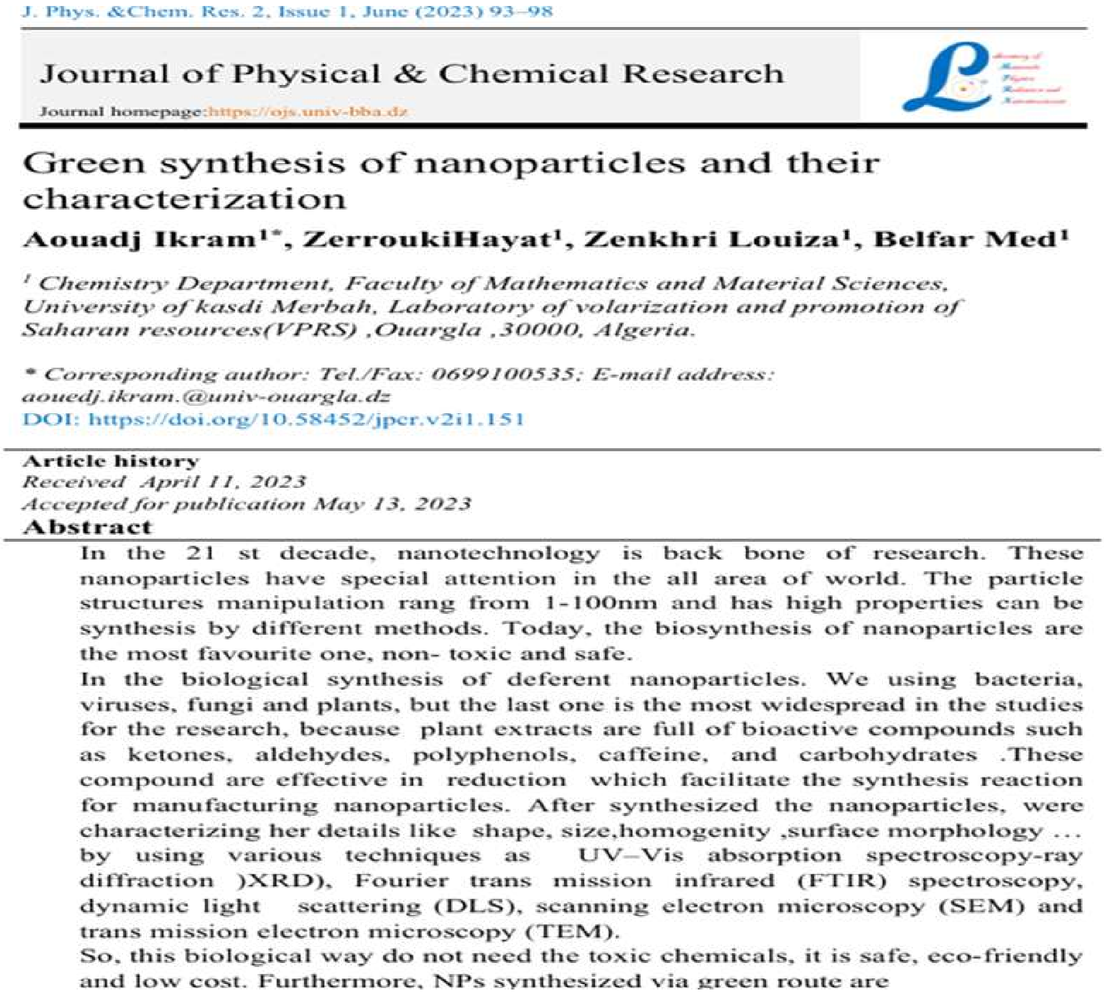

J. Phys. &Chem. Res. 2, Issue 1, June (2023) 93–98

Journal of Physical & Chemical Research

Journal homepage:https://ojs.univ-bba.dz

Green synthesis of nanoparticles and their characterization

Aouadj Ikram[1*], ZerroukiHayat[1], Zenkhri Louiza[1], Belfar Med[1]

[1] Chemistry Department, Faculty of Mathematics and Material Sciences, University of kasdi Merbah, Laboratory of volarization and promotion of Saharan resources(VPRS) ,Ouargla ,30000, Algeria.

** Corresponding author: Tel./Fax: 0699100535; E-mail address: aouedj.ikram.@univ-ouargla.dz*

DOI: https://doi.org/10.58452/jpcr.v2i1.151

Article history

Received April 11, 2023

Accepted for publication May 13, 2023

Abstract

In the 21 st decade, nanotechnology is back bone of research. These nanoparticles have special attention in the all area of world. The particle structures manipulation rang from 1-100nm and has high properties can be synthesis by different methods. Today, the biosynthesis of nanoparticles are the most favourite one, non- toxic and safe.

In the biological synthesis of deferent nanoparticles. We using bacteria, viruses, fungi and plants, but the last one is the most widespread in the studies for the research, because plant extracts are full of bioactive compounds such as ketones, aldehydes, polyphenols, caffeine, and carbohydrates .These compound are effective in reduction which facilitate the synthesis reaction for manufacturing nanoparticles. After synthesized the nanoparticles, were characterizing her details like shape, size,homogenity ,surface morphology ... by using various techniques as UV–Vis absorption spectroscopy-ray diffraction)XRD), Fourier trans mission infrared (FTIR) spectroscopy, dynamic light scattering (DLS), scanning electron microscopy (SEM) and trans mission electron microscopy (TEM).

So, this biological way do not need the toxic chemicals, it is safe, eco-friendly and low cost. Furthermore, NPs synthesized via green route are